In presenting this dissertation in partial fulfillment of the requirements for an advanced degree at Idaho State University, I agree that the Library shall make it freely available for inspection. I further state that permission to download and/or print my dissertation for scholarly purposes may be granted by the Dean of the Graduate School, Dean of my academic division, or by the University Librarian. It is understood that any copying or publication of this dissertation for financial gain shall not be allowed without my written permission.

Signature _____

Date _____

Isotopic Analysis of Fissile Materials Using Delayed γ-rays from Neutron Induced Fission

A Dissertation presented

by

Edward Thomas Elzea Reedy

to

The Department of Physics

in partial fulfillment of the requirements

for the degree of

Doctorate of Philosophy

in the subject of

Applied Physics

Idaho State University

December 2015

To the Graduate Faculty:

The members of the committee appointed to examine the dissertation of Edward Thomas Elzea Reedy find it satisfactory and recommend that it be accepted.

Alan W. Hunt,
Major Advisor

Dan Dale,
Committee Member

Dustin McNulty,
Committee Member

Eddie Tatar,
Committee Member

Andy W. Holland,
Graduate Faculty Representative

For that penguin.

Acknowledgments

I would like to thank my collaborators, especially Heather A. Seipel, Vladimir Mozin and Bernhard A. Ludewigt. Without them this research would not have been possible. I would also like to thank my advisor, Alan W. Hunt, for his patience. Lastly, my parents, because they never object to my path in life.

Contents

List of Figures

List of Tables

Thesis advisor
Alan W. Hunt

Author
Edward Thomas Elzea Reedy

Isotopic Analysis of Fissile Materials Using Delayed γ-rays from Neutron Induced Fission

Abstract

Delayed γ-rays from induced fission events have long proven useful in the detection, identification and quantification of fissionable material. These γ-rays provide an intense, highly penetrating and persistent signature unique to the fissioning isotope. Utilizing thermal neutrons as a probing radiation source highlights the fissile material while leaving the fertile untouched. This research looks at delayed γ-rays from neutron induced fission and their potential applications to the nuclear safeguards and forensics community. A 25 MeV linear electron accelerator was used to produce a bremsstrahlung photon beam. This photon beam was then incident on a ^{9}Be converter to produce an intense neutron source. The neutrons were then moderated to thermal energies before being incident on targets consisting of ^{239}Pu, ^{235}U and combinations thereof. Once the irradiation cycle was complete, each target was shuttled into a shielded experimental cell and energy spectra were collected via a high-purity germanium detector. The resulting spectra were then analyzed using discrete line comparisons and broad spectrum fitting algorithms such as principle component analysis for signatures capable of determining the isotopic composition of mixed targets.

Chapter 1

Introduction

1.1 Introduction

The nuclear forensics and safeguards community has placed significant interest in active inspection as a means to quickly detect, identify and quantify fissionable materials [1–9]. Active inspection utilizes a probing radiation source to induce nuclear reactions in a target and then monitors for the emissions from these reactions. Buried within these emissions are unique signatures specific to isotopes of interest. These signatures include nuclear resonance fluorescence, prompt and delayed neutrons as well as prompt and delayed γ-rays [1, 3, 9, 10]. Several active inspection techniques utilize these signatures and show promise for nuclear safeguards and forensics applications.

For the detection of fissionable materials, it is often advantageous to utilize the fission process since, by definition, this process is unique to these materials [8, 9, 11, 12]. In this scenario, a probing source of either neutrons or photons incites the fission process in a target whereby nuclei are split into two fission fragments. Almost immediately following fission (10^{-13} s) prompt neutrons and γ-rays are released from the fission fragments [12]. Following this release, the fission fragments halt the further release of neutrons or γ-rays until they undergo the β-decay process or an isomeric transition [12]. These fission fragments have half-lives ranging from milliseconds to tens of years, thus delaying the emission of neutrons and γ-rays to these longer timescales [13, 14]. Because nonfissionable materials do not undergo this process,

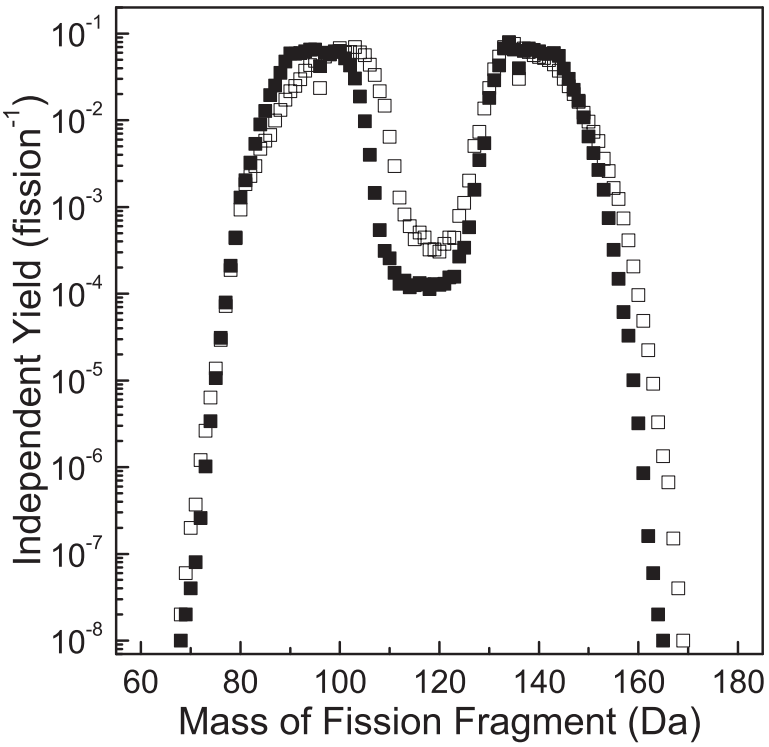

Figure 1.1: The independent fission fragment mass distribution of ^{235}U (■) and ^{239}Pu(□) for thermal neutron induced fission. The overall independent yield is normalized to 2 [14].

delayed neutrons and γ-rays thus provide signatures unique to fission that persist into these longer timescales.

Figure 1.1 shows the independent mass distributions of ^{235}U and ^{239}Pu for thermal neutron induced fission [14]. The low-mass centroid differs by $\sim$4 Da between these two isotopes while the high-mass centroid remains relatively unshifted. The shift in the low-mass centroid produces a significant difference in the yield of fission fragments between the two isotopes [14]. However, while the centroid for the high-mass fission fragment distribution changes little, the individual yields within this distribution can vary greatly [13, 14]. These shifts in the distribution lead to dramatically different fission fragment yields between fissioning nuclei. Since each fission fragment will emit characteristic neutrons and γ-rays as it decays towards stability, these differences can be used to determine the original isotope undergoing fission [15].

With fission fragments releasing on average ∼7 MeV into delayed γ-rays, many of these γ-rays lie above the limit of naturally occurring radioactive sources (∼2.6 MeV) as well as the limit of long lived sources found in spent nuclear fuel (∼3 MeV) [3, 8, 10, 12, 14–16]. Figure 1.2 shows the high-energy delayed γ-ray distribution emitted from ^{235}U and ^{239}Pu [14, 15]. Approximately 12% of the total γ-ray yield comes from the high-mass distribution. The remainder of the γ-rays, 88%, come from the low-mass distribution where the more drastic differences are seen in the fission fragment yield and, subsequently, in the yield of γ-rays in excess of 3 MeV [13–16]. Because these γ-rays tend to be emitted by relatively short-lived fission fragments (milliseconds-seconds) and at energies above ∼3 MeV, they can provide a unique signature of fissionable material in a low background region indicative of the current amount of material in a sample and are not influenced by long term build up of longer lived fission fragments [10, 14, 16].

Figure 1.3.a shows the photofission cross section for ^{239}Pu, ^{235}U and ^{238}U [14]. In many nuclear inspection scenarios, like cargo inspection, mere detection of any fissionable material is all that is necessary [3, 17]. In these instances, a photon beam as the interrogating source is a powerful tool capable of penetrating a significant amount of shielding [10]. However, of significant interest to the nuclear forensics and safeguards community is the desire to determine the isotopic composition of fissile material, specifically that of ^{239}Pu and ^{235}U [6, 8, 18]. These materials are utilized in the production of nuclear weapons and in the instance of safeguards, it is necessary to track the quantities of these materials to prevent diversion for such a purpose. In the case of nuclear forensics, it is necessary to identify the specific isotopic ratios in such material so it can be confirmed or attributed to a specific nation state. Since many heavy isotopes have large photofission cross sections, utilization of a photon beam for interrogation can cause materials such as ^{238}U to interfere with the detection of fissile material [14]. While neutrons can easily be shielded with hydrogenous material, in many of these instances material is available for direct inspection with minimal or no shielding [8, 18, 19]. This allows for the use of neutrons as an interrogating source. Figure 1.3.b shows the neutron fission cross section for ^{239}Pu, ^{235}U and ^{238}U [14]. The cross section for ^{238}U is significantly suppressed for thermal neutron energies.

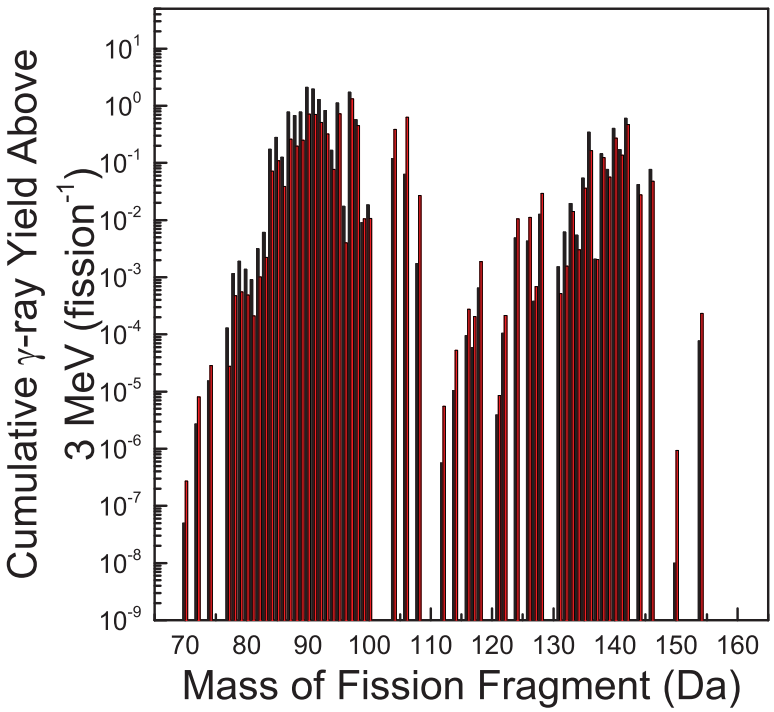

Figure 1.2: The cumulative high-energy γ-ray distribution of ^{235}U (black) and ^{239}Pu (red) as a function of fission fragment mass. Approximately 88% of the total γ-rays above 3 MeV come from the low-mass distribution [14, 15].

By utilizing neutrons as the interrogating source, the interference from such material can be significantly minimized, allowing for improved detection, identification and quantification of fissile material.

This dissertation seeks to provide a method for the quantification of fissile material for nuclear forensics and safeguards applications. A pulsed linear electron accelerator was used to produce a bremsstrahlung photon beam. This photon beam was then incident on a ^{9}Be converter that produced approximately 10^{10} neutrons$\cdot$s^{-1}. A polyethylene moderator was then used to reduce the energy of the neutrons to thermal energies where they were incident on targets containing varying amounts of ^{239}Pu and ^{235}U. After irradiation, the material was shuttled to a shielded experimental cell. A high-purity germanium detector (HPGe) was then used to collect delayed γ-ray spectra from the targets. The irradiation and count times were varied to deter-

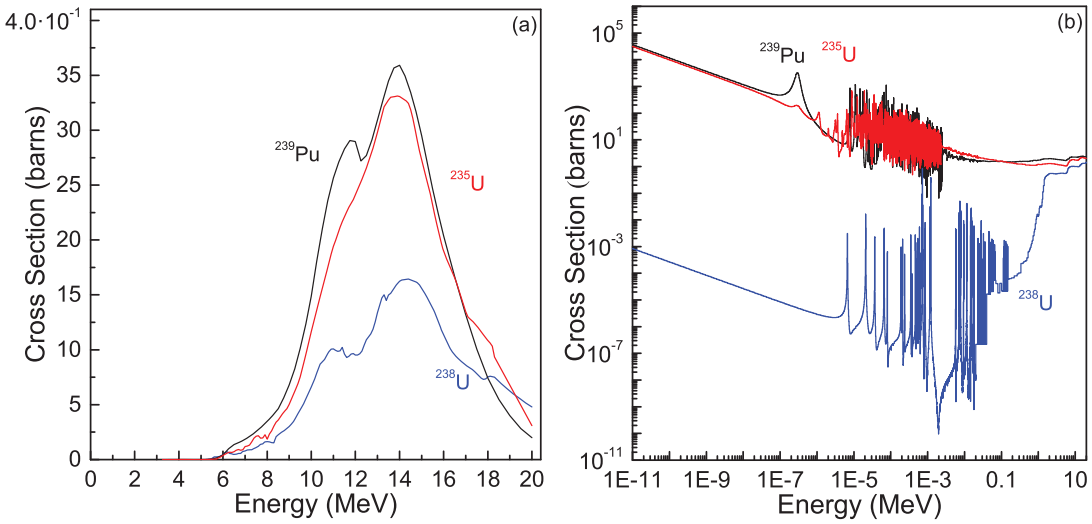

Figure 1.3: Photofission (a) and neutron induced fission (b) cross sections for ^{239}Pu (black), ^{235}U (red) and ^{238}U (blue) [14].

mine the optimum structure to emphasize discrete high-energy delayed γ-rays from short-lived fission fragments. Once this irradiation/count structure was optimized, multiple samples containing varied quantities of ^{239}Pu and ^{235}U were inspected and the resulting energy spectra were analyzed to determine a capable and unique fingerprint for distinguishing between fissile materials. Analysis methods for the determination of isotopic concentration included: peak ratio analysis, spectral contribution analysis, principal component analysis, multi-Gaussian fitting, etc. These analysis methods were compared and, where possible, combined to determine their relative success in this application. This dissertation will provide the physics background and formulation of such a process with emphasis on:

- **Induced Fission** An introduction to the induced fission process and how it pertains to the detection of fissile materials for nuclear forensics and safeguards.
- **Detection** The physics of how the γ-rays from fission are detected using a HPGe detector.
- **Analysis** An overview of the various analysis techniques and their applications to the identification and quantization of fissile materials.

Chapter 2

Physics Background and Fundamentals

2.1 Fission

Nuclear fission was discovered by Hahn and Strassmann in 1939 in an effort to create transuranic elements by bombarding natural uranium with neutrons [20]. In the process of measuring the products of the reaction to determine if the experiment was successful one of the products was found to be an isotope of barium. It was realized that barium was not a contaminant and that it could not be produced through the normal decay channels of an excited isotope of uranium. The only remaining process that could produce barium as a result was that of nuclear fission whereby the nucleus was split into two parts by the bombardment of neutrons. Following this result, Meitner and Frisch proposed the Liquid Drop Model of a nucleus to explain the fission process [21]. The Liquid Drop Model of the nucleus dictates that the nucleus resembles an incompressible fluid with the strong force playing the role of surface tension similar to that of a droplet of water [21]. Thus fission is the division of this droplet of water into two or, less commonly, more parts.

Carl Friedrich von Weizsäcker formulated the equation,

$$E_b(Z,N) = \alpha_1 A - \alpha_2 A^{2/3} - \alpha_3 \frac{Z(Z-1)}{A^{1/3}} - \alpha_4 \frac{(N-Z)^2}{A} + \Delta, \qquad (2.1)$$

to describe nuclear binding energy based on the notion of a liquid drop, where N, Z and A are the given nucleon numbers of an isotope [22]. In Weizsäcker's equation the first term increases linearly with the increase in nuclear mass and is referred to as the volume term. The linear increase in binding energy is attributed to the fact that the nuclear strong force treats neutrons and protons on an equal footing. The second term, $\alpha_2 A^{2/3}$, accounts for a reduction in binding energy at the surface of the nucleus. This reduction is due to a decrease in the "nearest neighbors" of surface nucleons and is attributed to the short range of the strong force in combination with the reduction of surrounding nucleons of those at the surface. Because of Coulomb repulsion, the binding energy will be reduced with the addition of protons. Term three, $\alpha_3 \frac{Z(Z-1)}{A^{1/3}}$ accounts for this repulsive force. Term four, $\alpha_4 \frac{(N-Z)^2}{A}$, takes isospin into consideration and maximizes the binding energy for isotopes where $N = Z$. The final term, Δ, is a correction to account for spin coupling. For odd atomic nuclei $\Delta = 0$. If the atomic mass is even, Δ is positive for Z and N both being even and negative when Z and N are both odd. The αs are determined empirically though a best fit of known binding energies of nuclei. Wong gives estimates for the αs as: $\alpha_1 = 16$ MeV, $\alpha_2 = 17$ MeV, $\alpha_3 = 0.6$ MeV and $\alpha_4 = 25$ MeV [22].

For the thermal neutron fission reaction of,

$$^{235}_{92}U_{143} +^{1}_{0} n_1 \rightarrow^{236}_{92} U^*_{143} \rightarrow^{137}_{55} Cs^*_{82} +^{98}_{37} Rb^*_{61}, \tag{2.2}$$

the Weizsäcker formula predicts the total energy release to be 168.5 MeV. This reaction is favored over the decay of $^{236}_{92}U^*_{143}$ by means other than fission [22]. As well as accurately describing the energetics of why fission proceeds with the introduction of a neutron to heavy elements, the Weizsäcker formula also showed that the process can proceed spontaneously for $Z^2/A \geq 48$, as is the case with many heavy isotopes [11]. Figure 2.1 shows a schematic of the induced fission process utilizing neutrons as the probing radiation source. At time zero, a neutron is absorbed by the nucleus. The nucleus absorbs the energy of the neutron and is further excited by the change in binding energy the neutron provides. In the example given in Equation 2.2 the absorbed energy of the $^{236}_{92}U^*_{143}$ nucleus is ~ 6 MeV. Within a short time period,

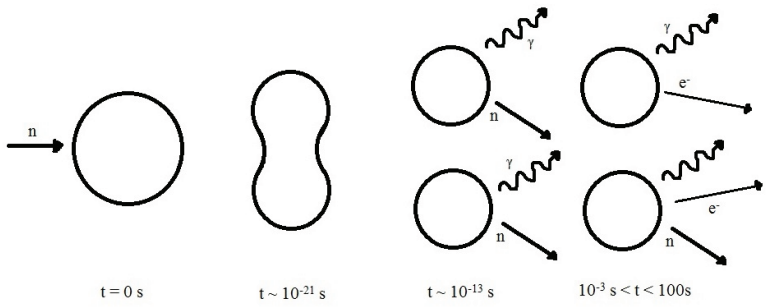

Figure 2.1: The neutron induced fission process. At time zero, a neutron is absorbed by the nucleus and the combination of the neutron's energy with the change in binding energy excites the nucleus by several MeV. Within 10^{-21} s the nucleus is deformed and Coulomb repulsion begins to tear the nucleus apart. By 10^{-13} s the fission fragments are fully separated by Coulomb repulsion and begin to emit prompt radiation in the form of neutrons and γ-rays. This process of decay is halted by the β-decay process delaying further emissions of neutrons and γ-rays by milliseconds to years. [12].

10^{-21} s, the nucleus deforms and Coulomb repulsion drives the nucleus apart [12]. Following the scission of the nucleus, the resulting fission fragments are highly excited and release prompt neutrons and γ-rays on the order of 10^{-13} s [12]. Following the release of prompt emissions, the fission fragments reach a ground state, effectively pausing further emissions until the β-decay process or an isomeric transition commences. These fission fragments subsequently have half-lives ranging from milliseconds to years [13, 14]. Following β-decay, subsequent emissions of neutrons and γ-rays can proceed. These emissions are referred to as delayed γ-rays and neutrons due to their, sometimes lengthy, delay caused by the decay processes.

2.1.1 Fission Fragments

Figure 2.2 shows the cumulative fission fragment mass distribution for ^{235}U and ^{239}Pu for thermal neutron induced fission [14]. Approximately 99.9% of fission events result in the production of two fission fragments with the remaining ∼0.1% results in ternary fission events whereby three fragments are produced [23]. As seen in Figure 2.2, the result of fission is not two equally sized fission fragments each with 1/2 the mass of the fissioning isotope. While the liquid drop model of fission does well

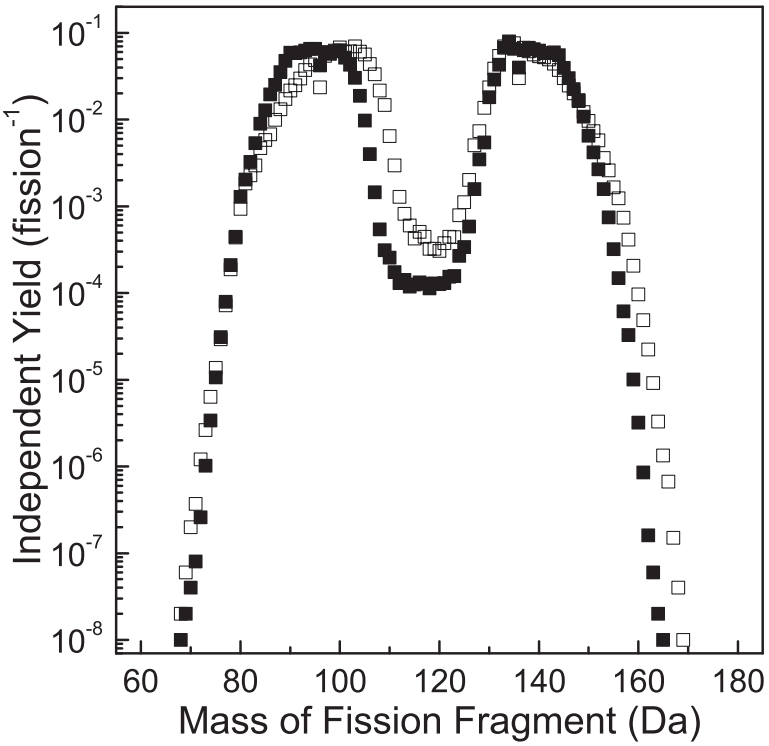

Figure 2.2: The independent fission fragment mass distribution of ^{235}U (■) and ^{239}Pu (□) for thermal neutron induced fission. The overall independent yield is normalized to 2 [14].

to explain the process, it fails to explain the asymmetry of the fission fragment distribution. This asymmetry is best explained by the nuclear shell model [23]. Similar to the atomic shell model, nucleons fill shells of increasing energy following the Pauli Exclusion Principle with neutrons and protons having independent shell structures. The binding energy of the nucleus closely follows that of the Weizsäcker mass formula. However, for certain numbers of neutrons or protons, the binding energy is significantly higher than what is predicted by the liquid drop model. These numbers correspond to completely filled nuclear shells at 2, 8, 20, 50, 82 and 126 nucleons and are called magic numbers [23]. Instances like $^{4}_{2}\mathrm{He}_{2}$ and $^{208}_{82}\mathrm{Pb}_{126}$, where both neutron and proton shells are filled, are called doubly magic and are remarkably stable isotopes.

Occurrences of these filled shells exist at the lower edge of the high-mass dis-

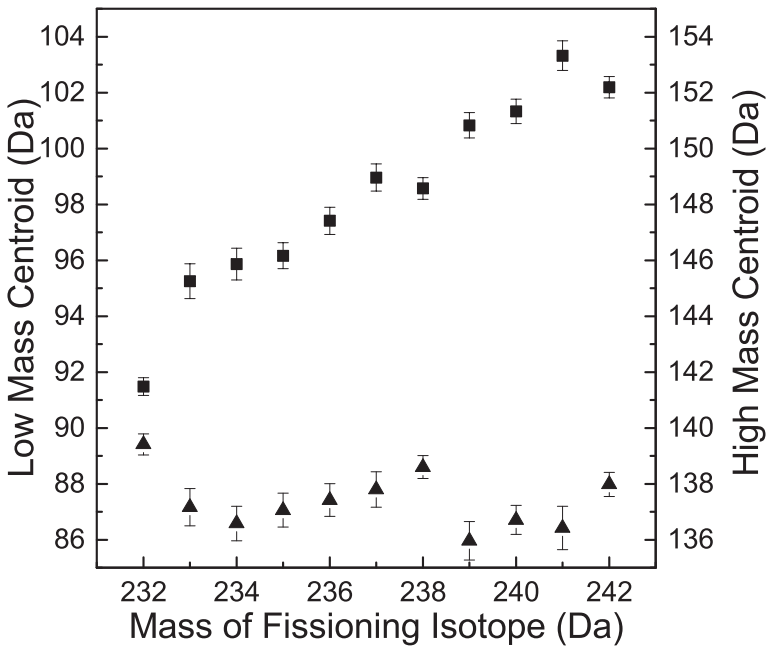

Figure 2.3: High-mass (▲) and low-mass (■) distribution centroids for fissionable material with nuclear masses between 232 and 242 [14].

tribution. This area of stability effectively pins the high-mass distribution centroid around 137 Da. Figure 2.3 shows the centroid locations of the high-mass and low-mass distributions for various isotopes [14]. As the mass of the initial fissioning isotope is increased, the low-mass distribution must shift upwards to accommodate this increase in nuclear mass. The isotopes ^{235}U and ^{239}Pu differ in nuclear mass by 4 Da and it is clear from Figure 2.3 that the low-mass centroid shifts by this amount to accommodate the difference. While the high-mass distribution centroid does not shift notably from fissioning isotope to isotope, the individual yields within this distribution can vary greatly [13, 14].

2.1.2 Prompt and Delayed Emissions

Following scission, the fission fragments are in a highly excited state. On a very short timescale following nuclear scission, $\sim 10^{-13}$ s, prompt emissions of neutrons and γ-rays occur [12]. On average, $2-3$ prompt neutrons and $6-8$ prompt γ-rays are

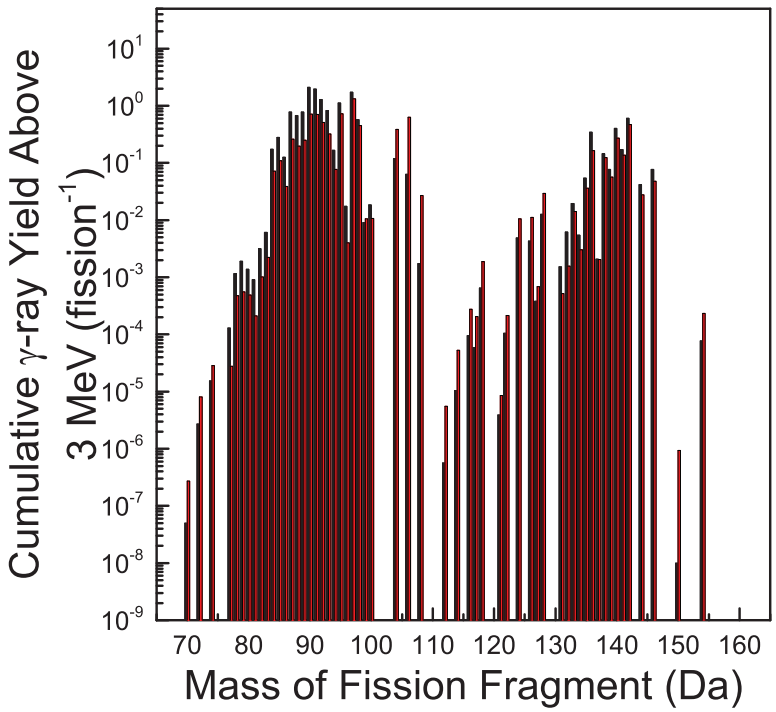

Figure 2.4: The cumulative high-energy γ-ray distribution of ^{235}U (black) and ^{239}Pu (red) as a function of fission fragment mass. Approximately 88% of the total γ-rays above 3 MeV come from the low-mass distribution where drastic differences in fission fragment yield are observed. The cumulative yield of β-delayed γ-rays from thermal neutron fission is 14.8 and 8.25 γ-rays·fission^{-1} for ^{235}U and ^{239}Pu, respectively [14,15].

emitted per fission event [12]. After prompt emission, while still excited, there are no further emission of neutrons and γ-rays until the fission fragments undergo β-decay or isomeric transition. Depending on the fission fragment, half-lives for these processes range from milliseconds to years [14]. Once the fission fragment undergoes β-decay or an isomeric transition, it can continue to emit photons and neutrons. This process results in delayed γ-rays and neutrons emitted on these longer timescales following fission. In contrast to prompt emissions, the delayed neutron yield is only $3-5\%$ per fission event while delayed γ-ray levels remain elevated at $\sim$7 delayed γ-rays per fission event [12]. With approximately 7 MeV of energy going into delayed γ-ray emissions, many of these γ-rays are produced with energies in excess of the limit of natural background, $\sim$2.6 MeV, and even that of spent nuclear fuel, $\sim$3 MeV [3,10,12,14–16].

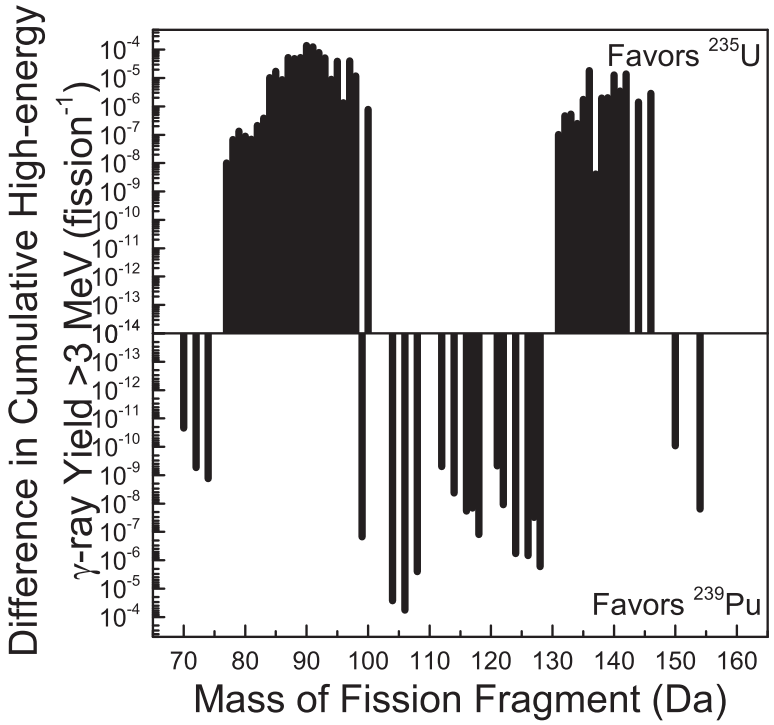

Figure 2.5: The difference in yield of high-energy γ-rays between ^{235}U and ^{239}Pu. The larger yield differences favor ^{235}U while very few γ-rays favor ^{239}Pu [14, 15].

In addition to being of higher-energy and long-lived, delayed γ-rays are unique to the fission fragment. Because the fission fragment distribution can be traced to the initial fissioning isotope, delayed γ-rays provide a unique and persistent fingerprint of fissionable material. Figure 2.4 shows the cumulative γ-ray distribution above 3 MeV for ^{235}U and ^{239}Pu. Approximately 14% of the total high-energy γ-ray yield comes from the high-mass distribution [14, 15]. The remainder of the γ-rays, $\sim$86%, come from the low-mass distribution where the more drastic differences are seen in the fission fragment yield [14, 15].

The differences between high-energy γ-ray yields for thermal neutron fission of ^{235}U and ^{239}Pu are shown in Figure 2.5 [14, 15]. Overall, the cumulative yield of β-delayed γ-rays from thermal neutron fission is approximately 79% higher for ^{235}U than for that of ^{239}Pu [14, 15]. Comparing the γ-ray yield as a function of mass of the fission fragment shows that a majority of the γ-ray emissions in the high and

low-mass distributions favor ^{235}U, while a small number in the valley appear to favor ^{239}Pu. Fission fragments in these regions are likely to emit γ-rays unique to ^{235}U and ^{239}Pu, respectively. Thus, analysis techniques that focus on these emissions will more accurately identify and quantify the fissionable material.

2.2 High Purity Germanium Detectors

High-purity germanium detectors (HPGe) are solid state semiconductor photon detectors that consist of a single crystal of lightly doped high-purity germanium, an n^+ contact and a p^+ contact [24]. High-purity germanium is currently the most pure crystal manufactured. Dopants in the crystal are not intentionally added but are a result of the manufacturing process [24]. If the resulting crystal has acceptor impurities, the crystal is utilized for a p-type detector. Conversely, if the crystal has donor impurities, this results in an n-type detector. Lithium diffusion is then used to form the n^+ contact and boron implantation is used to form the p^+ contact. The crystal is formed coaxially with one contact on the outside and the other internal to the detector. Since these methods create dead layers on the surface of the crystal of several hundred micrometers for the n^+ lithium layer and a few tenths of a micrometer for the p^+ boron layer, the resulting detectors vary in their sensitivity to low energy photons (below $\sim$300 keV) [24].

The detector is reverse biased to create an n-p junction with a large depletion region. To form the depletion region, regardless of detector type, positive bias is applied to the n^+ contact with negative bias being applied to the p^+ contact. The role of these contacts then depends on the germanium crystal's dopant material. If the crystal is ν-type the p^+ contact serves as the rectifying contact. Conversely, for π-type, the n^+ contact is the rectifying contact. The depletion region begins at these junctions and grows into the germanium crystal as more voltage is applied.

This depletion region serves as the active area of the detector. As a γ-ray traverses this region, it inelastically scatters with electrons in the crystal and ejects these electrons from their bound state creating electron-hole pairs. If these ejected electrons are of sufficient energy they will further scatter and continue to eject electrons as they

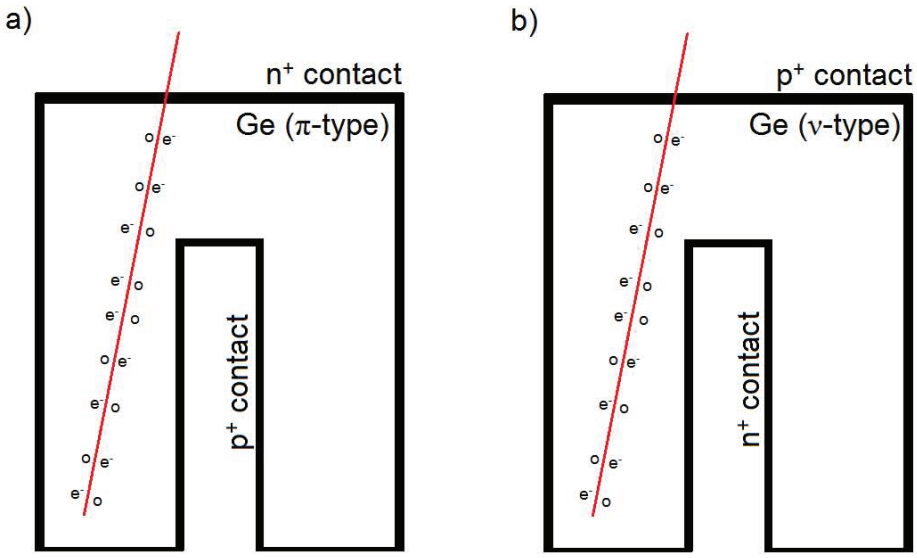

Figure 2.6: Cross-sectional view of p-type (a) and n-type (b) coaxial high-purity germanium detectors. Thick lines indicate the n^+ and p^+ contacts for each detector. A red line indicates the trajectory of an incident photon along with its initial electron (e^-) and hole (o) pairs [24].

lose energy. The γ-ray continues to scatter through the crystal creating a track of electron-hole pairs until its energy is completely absorbed or the γ-ray scatters out of the active region of the detector. These electron-hole pairs drift in the electric field within the depletion region creating a current and, subsequently, an electric pulse, until they are collected at the junctions. Because the number of electron-hole pairs is proportional to the incident energy of the absorbed photon, the amplitude of the electric pulse can be used to reconstruct the energy of the incident γ-ray. One issue faced by HPGe detectors is thermal energy. Thermal excitations can cause valence electrons to migrate to the conduction band, causing a high leakage current; therefore HPGe detectors require low operating temperatures and are typically cooled to liquid nitrogen temperatures, $\sim$77K [24].

While Compton Scattering is the dominant interaction in HPGe crystals, two other processes play significant roles: pair production and the photoelectric effect [24]. For germanium, the photoelectric effect dominates at low energies, less than $\sim$130 keV.

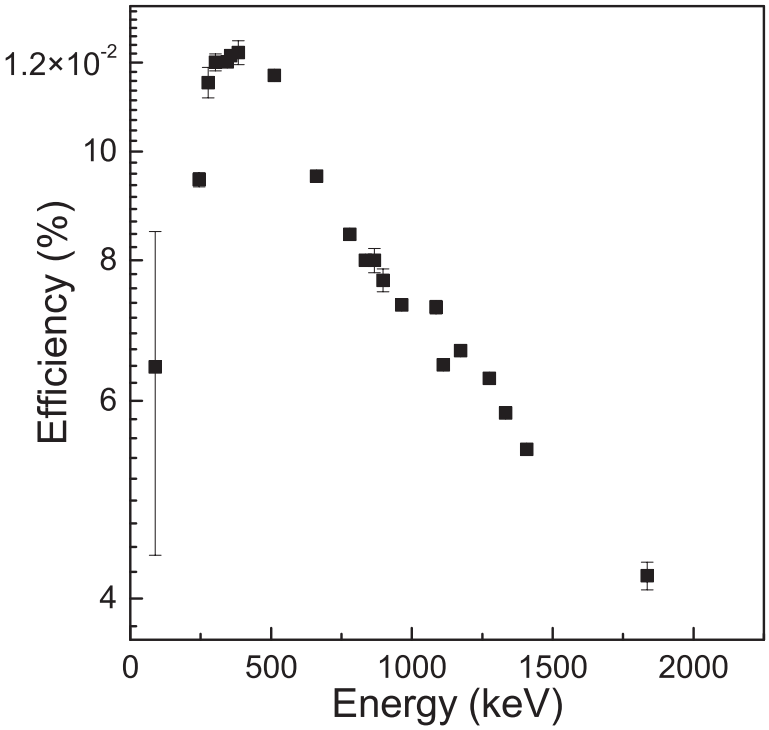

Figure 2.7: The absolute efficiency of a 48% relative efficient p-type HPGe detector. Sources were placed at a distance of 25 cm to the face of the detector.

In this process, as the photon enters the crystal it is entirely absorbed by an atom. This energy is then utilized to eject an atomic electron from its bound state with the energy of the γ-ray less the binding energy of that electron. Typical binding energy for these electrons is only a few electron volts. This electron scatters through the crystal and results in the eventual detection of the incident γ-ray. While these processes can take place at any energy, pair production can only take place if the incident γ-ray's energy is in excess of 1022 keV and dominates the interaction cross section above $\sim$5 MeV. In pair production, as the γ-ray enters the crystal its energy is used to produce an electron-positron pair. While the energy of the electron is easily captured, the positron annihilates with an electron to produce two 511 keV photons. If either of these photons escape the crystal the resulting energy captured is 511 keV less than the incident photon energy. If many of these are observed this creates an escape peak 511 keV below the photopeak. Likewise, if these processes are near the

edge of the active region of the detector, electrons or photons can fail to be collected. The remaining captured energy contributes to the Compton continuum and escape peaks below the energy of the photopeak.

Figure 2.7 shows the measured absolute efficiency of a 48% relative efficient high-purity germanium detector. Relative efficiency is determined by comparing the efficiency of the HPGe detector to that of a 7.62 by 7.62 cm NaI scintillation detector. Figure 2.7 shows a significant drop in detector efficiency for low-energies. This decrease is caused by a dead layer on the outside of the detector. This dead layer is formed by the lithium n^+ contact which is often several hundred microns in thickness [24]. Contrary to p-type detectors, n-type HPGes have a thin, a few tenths of microns, outer boron layer [24]. This allows for increased efficiencies at lower-energies while maintaining identical behavior at high-energies.

2.3 Analysis Techniques

2.3.1 Peak Ratio Analysis

Peak ratio analysis utilizes the ratio of two photopeaks present in and energy spectrum to determine isotopic information [9, 25–27]. This method is a common analysis technique used to determine composition in a variety of settings including applications to fuel reprocessing and photon activation analysis [9, 25–28]. The only requirement is a series of peaks, each with differing intensities in their respective material. The ratios of such peaks are only influenced by variances in the composition and remain consistent in identical samples. For this application, delayed γ-rays from fission fragments serve this purpose. Because each fissioning isotope has a unique fission fragment distribution, the resulting delayed γ-ray spectra differ in photopeak intensities. Unfortunately, because many fission fragments share photopeaks in the high-energy region too close for a high-purity germanium detector to resolve, this presents potential problems in determining isotopic composition of targets in this energy range [28].

The yield (Y) of a given peak in a mixed sample of ^{239}Pu and ^{235}U is given by,

$$Y = \frac{dY}{dm_{Pu}} \cdot m_{Pu} + \frac{dY}{dm_U} \cdot m_U, \tag{2.3}$$

where m_{Pu} and m_U are the masses of ^{239}Pu and ^{235}U and dY/dm is the yield per mass of that peak for each specific target. Equation 2.3 assumes the sample is small so as to minimize the effects of attenuation and moderation and that the number of neutrons entering the sample is significant with respect to the number consumed by the target in the fission process. In the case of a delayed γ-ray spectrum, the value dY/dm depends on the cross section of the material, incident radiation spectrum, the fission fragment yield and the branching ratio for the emission of that specific delayed γ-ray. The ratio of two discrete γ-ray peaks is given by,

$$Y_1 : Y_2 = \frac{\frac{dY_1}{dm_{Pu}} \cdot m_{Pu} + \frac{dY_1}{dm_U} \cdot m_U}{\frac{dY_2}{dm_{Pu}} \cdot m_{Pu} + \frac{dY_2}{dm_U} \cdot m_U}. \tag{2.4}$$

Substituting the relative concentration for ^{239}Pu,

$$R_{Pu} = \frac{m_{Pu}}{m_{Pu} + m_U}, \tag{2.5}$$

yields,

$$Y_1 : Y_2 = \frac{(\frac{dY_1}{dm_{Pu}} - \frac{dY_1}{dm_U}) \cdot R_{Pu} + \frac{dY_1}{dm_U}}{(\frac{dY_2}{dm_{Pu}} - \frac{dY_2}{dm_U}) \cdot R_{Pu} + \frac{dY_2}{dm_U}}. \tag{2.6}$$

Equation 2.6 is the ratio of two linear equations which produces a curve with two asymptotes at,

$$R_{Pu} = \frac{\frac{dY_2}{dm_U}}{\frac{dY_2}{dm_{Pu}} - \frac{dY_2}{dm_U}} \quad \text{and} \quad Y_1 : Y_2 = \frac{\frac{dY_1}{dm_{Pu}} - \frac{dY_1}{dm_U}}{\frac{dY_2}{dm_{Pu}} - \frac{dY_2}{dm_U}}. \tag{2.7}$$

By using a constant fiducial peak in the denominator, one that shares a common yield in both ^{239}Pu and ^{238}U,

$$\frac{dY_2}{dm_{Pu}} = \frac{dY_2}{dm_U}, \tag{2.8}$$

the asymptotes can be eliminated and Equation 2.6 reduces to a linear equation with

respect to relative concentration. Unfortunately, fiducial peaks can be limited in number and it is often necessary to characterize the peak ratios by the nonlinear form of Equation 2.6. Approximate values for the dY/dm's can be determined from measured pure spectra, simulation and simple calculations from the known fission fragment distribution.

2.3.2 Multi-Gaussian Fitting

Multi-Gaussian fitting deconvolves overlapping photopeaks into individual constituents. Because delayed γ-ray spectra are often complex and contain many close and overlapping photopeaks, it is often desirable to engage multi-Gaussian algorithms to discern the intensity of these overlapping photopeaks. The information garnered through these fits accurately conveys the peak area where singular methods fail. This information can then be used in PRA and various other analysis techniques to reduce the error associated with peak overlap. To accomplish this, multiple parameters about the photopeaks must be known including: energy, relative intensity, detector efficiency and resolution. The detector parameters can be determined either empirically or through simulations while the evaluated nuclear structure data files provide the energy and relative intensities of photopeaks for given isotopes [15, 28]. By knowing the relative intensities and detector efficiencies, multiple photopeaks from the same isotope can have linked intensities, further reducing the number of parameters in the fitting algorithm. Such a linked equation for two photopeaks, neglecting background, would be,

$$\begin{aligned} Y &= \frac{I_1}{\sigma_1\sqrt{2\pi}} e^{-\frac{(E-E_1)^2}{2\sigma_1}} + \frac{I_2}{\sigma_2\sqrt{2\pi}} e^{-\frac{(E-E_2)^2}{2\sigma_2}} \\ &= \frac{I_1}{\sigma_1\sqrt{2\pi}} e^{-\frac{(E-E_1)^2}{2\sigma_1}} + \frac{I_1 \cdot F(E_2)_{\frac{2}{1}}}{\sigma_2\sqrt{2\pi}} e^{-\frac{(E-E_2)^2}{2\sigma_2}}, \end{aligned} \tag{2.9}$$

where E_n is the energy of each peak, σ_n is the peak width, and I_n is the peak height. The factor, $F(E_2)_{\frac{2}{1}}$, is the ratio of intensities of peak 2 to peak 1. This factor is also influenced by the efficiency of the detector at the energy of the second peak. In this manner, all parameters with the exception of one, I_1, can be held fixed, reducing the

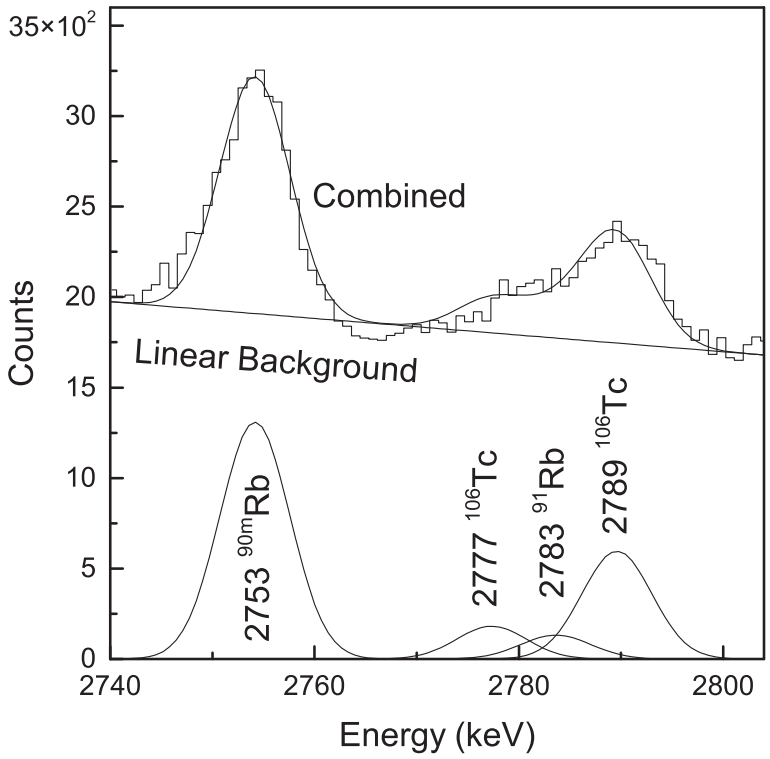

Figure 2.8: A portion of the delayed γ-ray energy spectrum collected from neutron induced fission in a combined target containing 2.9 g ^{239}Pu and 2.8 g ^{235}U alongside the results of a "fisrt-pass" multi-Gaussian fitting algorithm. The ^{106}Tc photopeaks have linked intensities making the resolution of the 2783 keV photopeak from ^{91}Rb resolvable. The individual Gaussian and linear components of the fit are also shown.

number of variable parameters from a potential six to one.

Figure 2.8 shows the results of a multi-Gaussian fit obtained across a section of a delayed γ-ray spectrum collected from the neutron fission of a combined ^{239}Pu and ^{235}U target. The individual 2753 keV photopeak can be quite easily resolved while the cluster containing three photopeaks cannot. To resolve the cluster, the intensities of the two photopeaks from ^{106}Tc were linked in the multi-Gaussian fit. Because the cluster of four peaks are in a narrow energy window, $\sim$60 keV, they are assumed to have the same resolution and detector efficiency. This approximation allows for the ratio of intensities between the ^{106}Tc peaks to be the branching ratio. While this fit is only a "first-pass" it shows that by linking intensities, photopeaks that are not

clearly visible, in this instance the 2783 keV peak from ^{91}Rb, can be resolved.

2.3.3 Spectral Contribution Analysis

Spectral contribution analysis has been a proven technique for determining isotopic composition [28, 29]. Rather than fitting individual peaks, a portion of the energy spectrum of a pure sample can be used as a component to produce a combined spectrum, the sum of the components being identical to the spectrum of the combined target. Utilizing the energy spectra of pure ^{235}U (ϕ_{235}) and ^{239}Pu (ϕ_{239}) as a basis set, the spectrum of a combined target ($\phi_{comb.}$) can be made by the equation:

$$\phi_{comb.} = \alpha_{239} \cdot \phi_{239} + \alpha_{235} \cdot \phi_{235}, \tag{2.10}$$

the coefficients, α_{239} and α_{235}, can be found quite easily through linear regression algorithms. This application of superposition can utilize measured or calculated spectra to determine the composition of an unknown energy spectrum provided there are sufficient differences between individual component spectra. It is also necessary that the basis spectra are representative of the conditions by which the unknown spectrum was taken. Furthermore, by normalizing the basis set to mass, the coefficients directly produce the masses of the material used to comprise the unknown spectrum.

Figure 2.9 shows delayed γ-ray energy spectra of ^{239}Pu and ^{235}U taken both individually and with the two sources combined. In very much the same fashion as Equation 2.3, a region of a spectrum can be described by,

$$\phi_{Reg.} = \frac{dY_{Reg.}}{dm_{Pu}} \cdot m_{Pu} + \frac{dY_{Reg.}}{dm_{U}} \cdot m_{U}. \tag{2.11}$$

This equation is just the sum of two linear equations with respect to the masses of ^{239}Pu and ^{235}U. In principal, the energy spectrum from the combined target is equal to the energy spectra of the two individual targets summed together. As shown in Figure 2.9 the two delayed γ-ray spectra from ^{239}Pu and ^{235}U summed together is very similar to that of the spectrum produced when the two targets are combined.

A concern does arise if the composition of the target material is not known com-

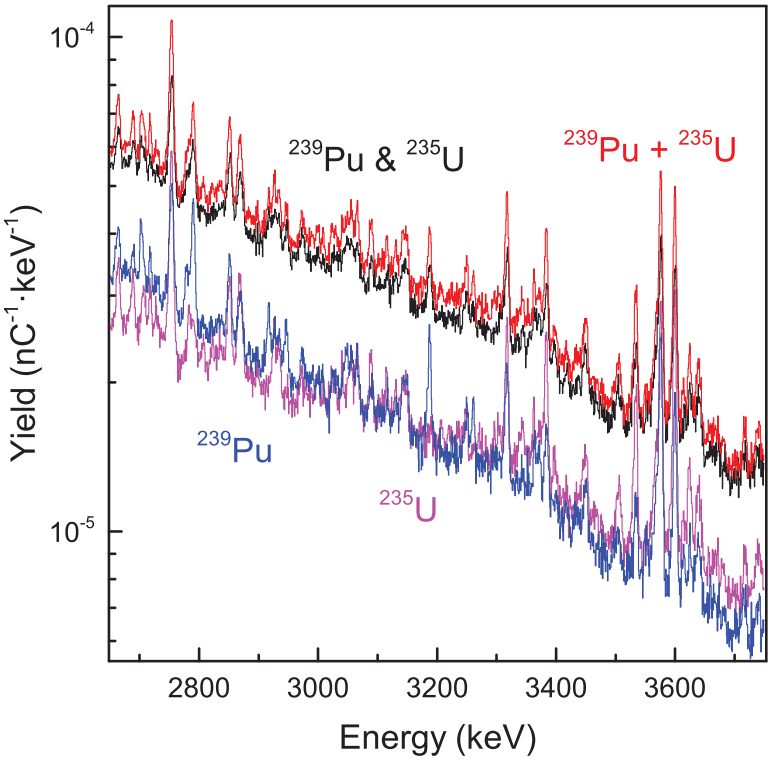

Figure 2.9: Delayed γ-ray energy spectra from neutron induced fission of 2.9 g ^{239}Pu (blue), 2.8 g ^{235}U (magenta) and a target of both 2.9 g ^{239}Pu and 2.8 g ^{235}U combined (black). The fourth spectrum was formed by adding the individual delayed γ-ray spectra of ^{239}Pu and ^{235}U together (red).

pletely or a background component is buried within the spectrum. Prior research has shown this algorithm to be relatively robust with respect to unknown and background components [28]. Provided that the unknown component spectra do not contain peaks that can be formed by the basis set, the algorithms can successfully deconvolve the known components utilizing their respective energy spectra [28].

2.3.4 Principal Component Analysis

Principal component analysis was first formulated by Karl Pearson in 1901 and was expanded into its present form by Harold Hotelling by 1933 [30, 31]. The main concept behind principal component analysis (PCA) is to find the direction of greatest

variance in a data set and orthogonally transform that data set along this direction [32]. Because orthogonal transformations preserve lengths of vectors and the angles between them, the overall shape of the data is preserved. PCA is often used to reduce a data set into the minimum number of parameters necessary for that data's description. It is also used to compare possibly correlated data sets to one another. The most common of these comparisons is facial recognition between two images. Since spectral data is represented in the same form as a digital image, as an array of numbers, PCA can be easily adapted to instances of spectral recognition.

An arbitrary set of data can be represented by an $m \times n$ matrix, A. Such a matrix would appear as,

$$A_{m,n} = \begin{pmatrix} \boldsymbol{a}_{1,1} & \boldsymbol{a}_{1,2} & \cdots & \boldsymbol{a}_{1,n} \\ \boldsymbol{a}_{2,1} & \boldsymbol{a}_{2,2} & \cdots & \boldsymbol{a}_{2,n} \\ \vdots & \vdots & \ddots & \vdots \\ \boldsymbol{a}_{m,1} & \boldsymbol{a}_{m,2} & \cdots & \boldsymbol{a}_{m,n} \end{pmatrix}, \tag{2.12}$$

with n columns representing different samples and m rows representing different variables or parameter vectors of the n^{th} sample. For the case of spectroscopy, the matrix A can be arranged to contain a single column of vectors. The vector $\boldsymbol{a}_m$ would thus represent the m^{th} sample's spectrum. An arbitrary transformation of the data matrix A to B would be,

$$PA = \begin{pmatrix} P \cdot \boldsymbol{a}_1 & P \cdot \boldsymbol{a}_2 & \cdots & P \cdot \boldsymbol{a}_n \end{pmatrix} = \begin{pmatrix} \boldsymbol{p}_1 \cdot \boldsymbol{a}_1 & \boldsymbol{p}_1 \cdot \boldsymbol{a}_2 & \cdots & \boldsymbol{p}_1 \cdot \boldsymbol{a}_n \\ \boldsymbol{p}_2 \cdot \boldsymbol{a}_1 & \boldsymbol{p}_2 \cdot \boldsymbol{a}_2 & \cdots & \boldsymbol{p}_2 \cdot \boldsymbol{a}_n \\ \vdots & \vdots & \ddots & \vdots \\ \boldsymbol{p}_m \cdot \boldsymbol{a}_1 & \boldsymbol{p}_m \cdot \boldsymbol{a}_2 & \cdots & \boldsymbol{p}_m \cdot \boldsymbol{a}_n \end{pmatrix} = B, \tag{2.13}$$

where $\boldsymbol{p}_m$ are the row vectors of P and $\boldsymbol{a}_n$ are the column vectors of A. The $\boldsymbol{p}_m$'s are the basis of the projection of the n^{th} sample's data set into B and must have size m. These projections will become the principal component directions and this limits the number of potential components to the number of available measurements, m [32].

PCA attempts to find the direction of greatest variance in this data set. To do this, the variance, or in this instance, covariance, must be calculated between the

data sets. The covariance of two variables x and y with means μ_x and μ_y is,

$$\sigma(x,y) = \langle (x-\mu_x)(y-\mu_y) \rangle. \tag{2.14}$$

This definition does little to calculate the covariance of data represented by a matrix. However, because the variables here are represented by a single matrix, A, this definition can be modified by subtracting the mean element of A, $\boldsymbol{\mu}_A$, from each element and taking the transpose of the matrix. Thus, the covariance of the matrix A becomes,

$$\begin{aligned} \sigma(x,y) = \sigma(A,A) &= \langle (A - \boldsymbol{\mu}_A \cdot J_{m,n})(A - \boldsymbol{\mu}_A \cdot J_{m,n})^T \rangle \\ &= \frac{1}{n-1}(A - \boldsymbol{\mu}_A \cdot J_{m,n})(A - \boldsymbol{\mu}_A \cdot J_{m,n})^T, \end{aligned} \tag{2.15}$$

with the factor $\frac{1}{n-1}$ providing an unbiased estimator for low values of n and the matrix $J_{m,n}$ containing only ones[1] [32]. For simplicity, the data set, A, can be mean-centered prior to construction of the covariance matrix, reducing Equation 2.15 to $\frac{1}{n-1}AA^T$. From here on it will be assumed that this restriction has been enforced and that the data matrix, A, has been mean centered.

Because the transformation being sought is one that minimizes the correlation between data, the variables of the transformed data, B, are assumed to be uncorrelated, thus the covariance of B should be as close to I as possible. This is achieved through the diagonalization of the covariance matrix, C_A. Because AA^T, and thus C_A, is a square, real and symmetric matrix, by definition it is diagonalizable by a matrix of its eigenvectors. The matrix comprised by these eigenvectors is orthonormal. Furthermore, such eigenvectors must be orthogonal. The covariance of the transformed data, B, can thus be represented as,

$$\begin{aligned} C_B &= \frac{1}{n-1}BB^T = \frac{1}{n-1}(PA)(PA)^T \\ &= \frac{1}{n-1}PAA^TP^T = PC_AP^T. \end{aligned} \tag{2.16}$$

[1]Equivalently, this operation can be performed by multiplying the mean-centering matrix/operator.

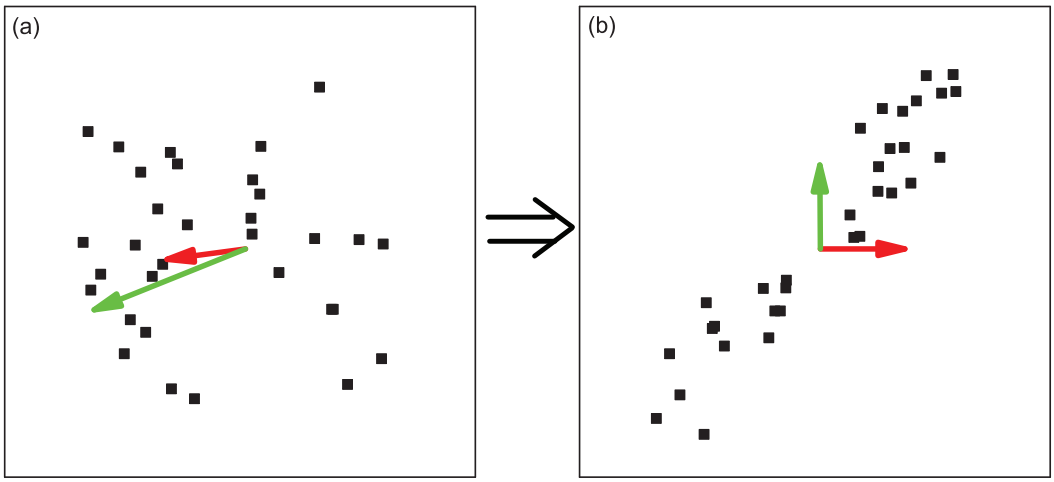

Figure 2.10: The results of a nonorthogonal transformation on a set of uncorrelated data. The original data set is (a) and the transformed is (b). Two potential principal component vectors are shown in red and green. These components are neither orthogonal nor normalized. Transforming the data set to this coordinate space creates a compression/extension of the data in these directions. Such a transformation results in the appearance of a false correlation between variables.

If the matrix P is restricted to be orthonormal, then,

$$P^T P C_A P^T P = C_A = P^T C_B P, \tag{2.17}$$

is just the solution to the diagonalization of C_A and is a special instance of singular value decomposition. Here, the matrix P is chosen such that C_B is diagonal with the i^{th} eigenvalue of C_A placed at $C_{B,ii}$. This transformation results in the orthonormal principal component vectors, p_m. This condition of orthonormality is required to keep the "shape" of our original data set and makes P an orthogonal transformation. Figure 2.10 shows the results of a nonorthogonal transformation on an arbitrary, uncorrelated data set. The transformation results in a false correlation between the data, where an orthogonal transformation would preserve the original shape of the data.

The diagonalization of the covariance matrix, C_A, results in the transformation matrix, P. The matrix P rotates the previously correlated data A into minimally

correlated data set B via Equation 2.13. The matrix, P, is subsequently comprised of the orthonormal eigenvectors of the covariant matrix, C_A. These eigenvectors become the principle components and, because they were formed from the covariance matrix, point in the directions of greatest variance. The principal component vector with the largest associated eigenvalue indicates the principal component with the greatest variance, the second largest indicates the direction of second greatest variance and so on. The individual vector components of P indicate the magnitude by which each vector in A is rotated by. These vector components are called loadings and data with similar characteristics will share similar transformations and thus similar loadings. To interpret the output of PCA, the loadings are often compared to each other and to observables to determine if there is a "useful" correlation between the two. The vectors of the transformed data, B, are called scores and each score inherits the maximum possible variance from the original data. Large values in a scores plot indicate that a great deal of that variable's variance is explained by the corresponding component. Comparisons of these scores indicate relationships between the variable, its corresponding loading and the potential observable that they are associated with.

2.3.5 Combination Applications

Many of these analysis techniques are not mutually exclusive. The peak areas found through multi-Gaussian fitting can, of course, be utilized in peak ratio analysis. These areas can also be used to form an array for use in principal component analysis. Likewise, the information from principal component analysis may show correlations between particular scores, relating energy information and observables such as relative concentration. Such information would be useful in determining which photopeaks best describe the sample in terms of concentration. Arrays of peak areas can even be substituted for the energy spectrum in spectral contribution analysis.

Chapter 3

Experiment

3.1 Setup

Figure 3.1 shows a diagram of the experimental setup used to irradiate the targets with moderated neutrons. A 25 MeV linear accelerator was utilized to generate a pulsed electron beam with an energy of 15 MeV at frequencies of 33 Hz and 132 Hz. Each pulse had a width of 4 μs and contained an average charge of $\sim$140 nC. The electron beam was then incident on a 4.2 g·cm^{-2} tungsten radiator to produce a pulsed bremsstrahlung photon beam with the corresponding endpoint energy. Directly following the radiator, at a distance of 4.75 cm, a 13.7 g·cm^{-2} aluminium scrubber was placed to absorb any electrons that passed through the tungsten radiator. The photon beam was then collimated through a 15.24 cm thick lead wall at a distance of 9.83 cm from the radiator. This prevented bremsstrahlung photons from the radiator from entering the target. Collimation consisted of a penetration through the Pb wall with a diameter of 6.03 cm centered on the beam line. The photon flux was then converted to a neutron source via the ^{9}Be(γ,n) reaction. To achieve this, a ^{9}Be cylinder was placed axial to the beam line with its center at a distance of 54.93 cm from the radiator. The ^{9}Be cylinder was 8.89 cm in diameter with a length of 46.99 g·cm^{-2}. In this configuration, the ^{9}Be converter is capable of generating $\sim 10^{10}$ neutrons·s^{-1}.

Blocks of virgin polyethylene (5.08 cm x 20.32 cm x 10.08 cm) were placed around the ^{9}Be converter to moderate the neutrons to near thermal energies. This moder-

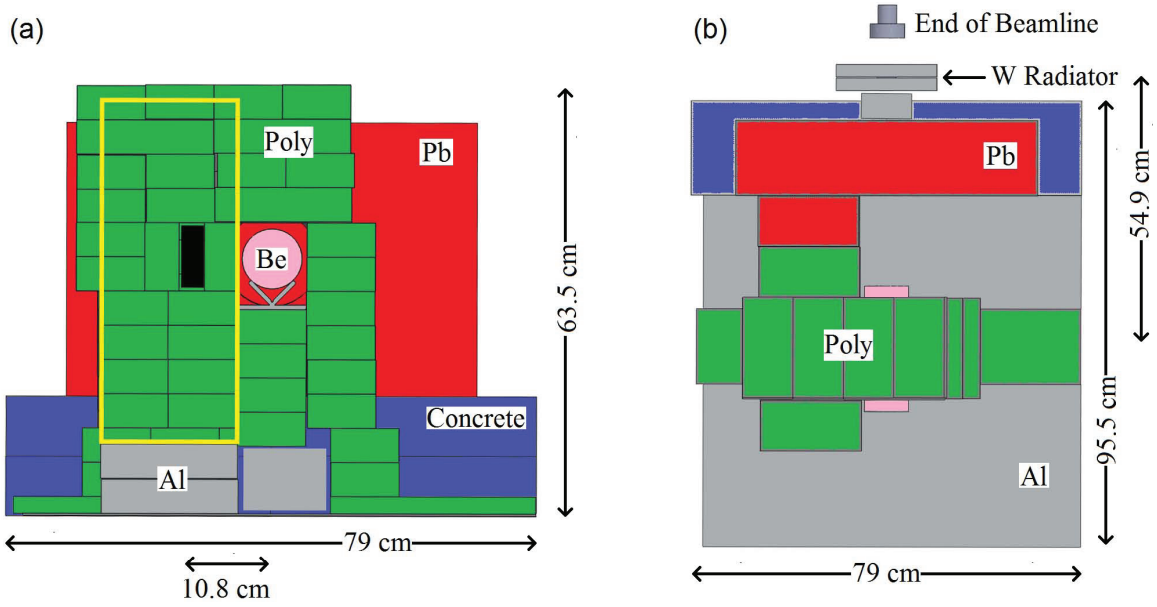

Figure 3.1: Schematic of the experimental setup used to irradiate the targets with moderated neutrons as seen from the face (a) and from above (b). The front view shows an outline of a polyethylene "door" in yellow that is removed from the drawing to allow for view of the irradiation cavity shown in black. The top view shows the end of the accelerator at the top of the drawing as well as the tungsten radiator housed between two 2.54 cm thick aluminum plates.

ation consisted of 20.32 cm above and below the Be cylinder and 10.16 cm on the downstream left side. An additional 20.32 cm of virgin polyethylene was placed to the downstream right side of the Be converter. This left the planar surfaces of the Be cylinder exposed. A pocket (3.81 cm x 20.32 cm x 10.08 cm) was created in the downstream right portion of the polyethylene stack perpendicular to the beamline to accommodate the targets. The center of the target pocket was 10.8 cm from the axis of the beamline and, subsequently, the axis of the ^{9}Be converter. In addition to this moderation, the ends of the cavity were sealed with two stacks of virgin polyethylene moderator measuring 50.8 cm x 20.32 cm x 10.08 cm. The target cavity can be seen in Figure 3.1.a to the left of the Be cylinder. The upstream and downstream polyethylene stacks can be seen in Figure 3.1.b. The downstream stack has been removed from Figure 3.1.a to allow visibility of the target cavity. Between the upstream

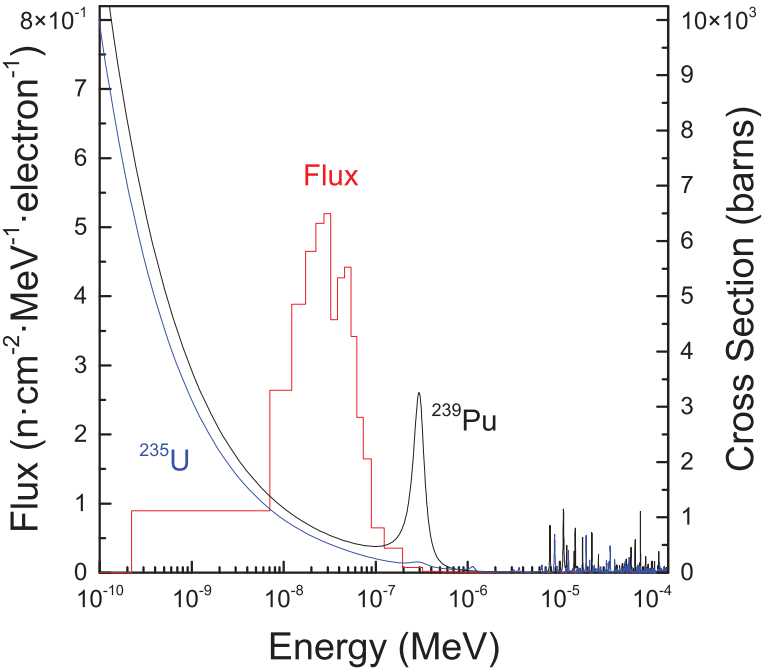

Figure 3.2: The neutron flux produced within the target cavity alongside the neutron induced fission cross sections for ^{235}U and ^{239}Pu [14,33]. Flux is normalized to target area, energy bin-width and source electron. Flux calculations were provided by Dr. Vladimir Mozin from Lawrence Livermore National Laboratory.

polyethylene stack and the large lead wall, additional lead was added to help shield the target from the photon flux. This shielding consisted of a lead stack with the dimensions of 50.8 cm x 20.32 cm x 10.08 cm, and prevented the occurrence of undesirable photofission in the targets caused by leakage of the bremsstrahlung photon beam through the lead wall.

Once the neutrons pass through the moderator into the cavity containing the target, their energy is significantly lowered. Figure 3.2 shows the calculated energy spectrum of the neutron flux along with the cross sections for ^{235}U and ^{239}Pu. The bulk of the neutron energies, 97.4%, lie in the continuum portion of the cross sections below 100 meV and out of the resonant structures. In this energy regime the cross sections of ^{239}Pu and ^{235}U are nearly identical in form with the ^{239}Pu cross section being ∼30% greater than that of the ^{235}U fission cross section at the peak neutron flux energy. Without the influence of resonant structures, the fission rate is not

overwhelmingly disproportionate to the masses of ^{239}Pu and ^{235}U. This relationship, while not necessary, is desirable so a small quantity of one does not obscure the signature of the other.

Once the target was irradiated, a sophisticated shuttling mechanism transported the target to a shielded experimental cell. Figure 3.3 shows a schematic of the overall setup. The experimental cell is shielded from the accelerator hall by a 1.85 m thick concrete and earthen wall. This prevents neutrons and γ-rays produced by the flash of the accelerator and the irradiation setup from influencing the detector. The shuttling system was 9.43 m in total length and transits through a 17.0 cm diameter penetration connecting the accelerator hall and the experimental cell. This, unfortunately, is a limiting factor in the size of target this system can accommodate. Transit times ranged from 21 s to 40 s and were kept constant for complementary experimental sets.

In the experimental cell, a 44% relative efficient, n-type high-purity germanium (HPGe) detector was placed. The detector was mechanically cooled which enabled convenient placement without the need to accommodate a large liquid nitrogen dewar. This detector collected energy spectra from the targets once their transit was complete. Figure 3.4 shows a schematic of the detector and the target at the counting location. The planar face of the HPGe detector was placed at a distance of 15.88 cm from the target's counting location. A 6.35 mm thick Pb sheet was placed over the face of the detector to reduce low-energy contributions from the target and minimize detector dead time. While the detector was located in a shielded experimental cell, additional shielding was placed around the detector to minimize any effects from the irradiation scheme. This shielding consisted of surrounding the detector axially with 5.08 cm of lead and 3.81 cm of borated polyethylene. An additional 10.16 cm of Pb was placed to the rear of the cavity housing the detector. This left only those γ-rays coming from the direction of the target visible to the HPGe detector.

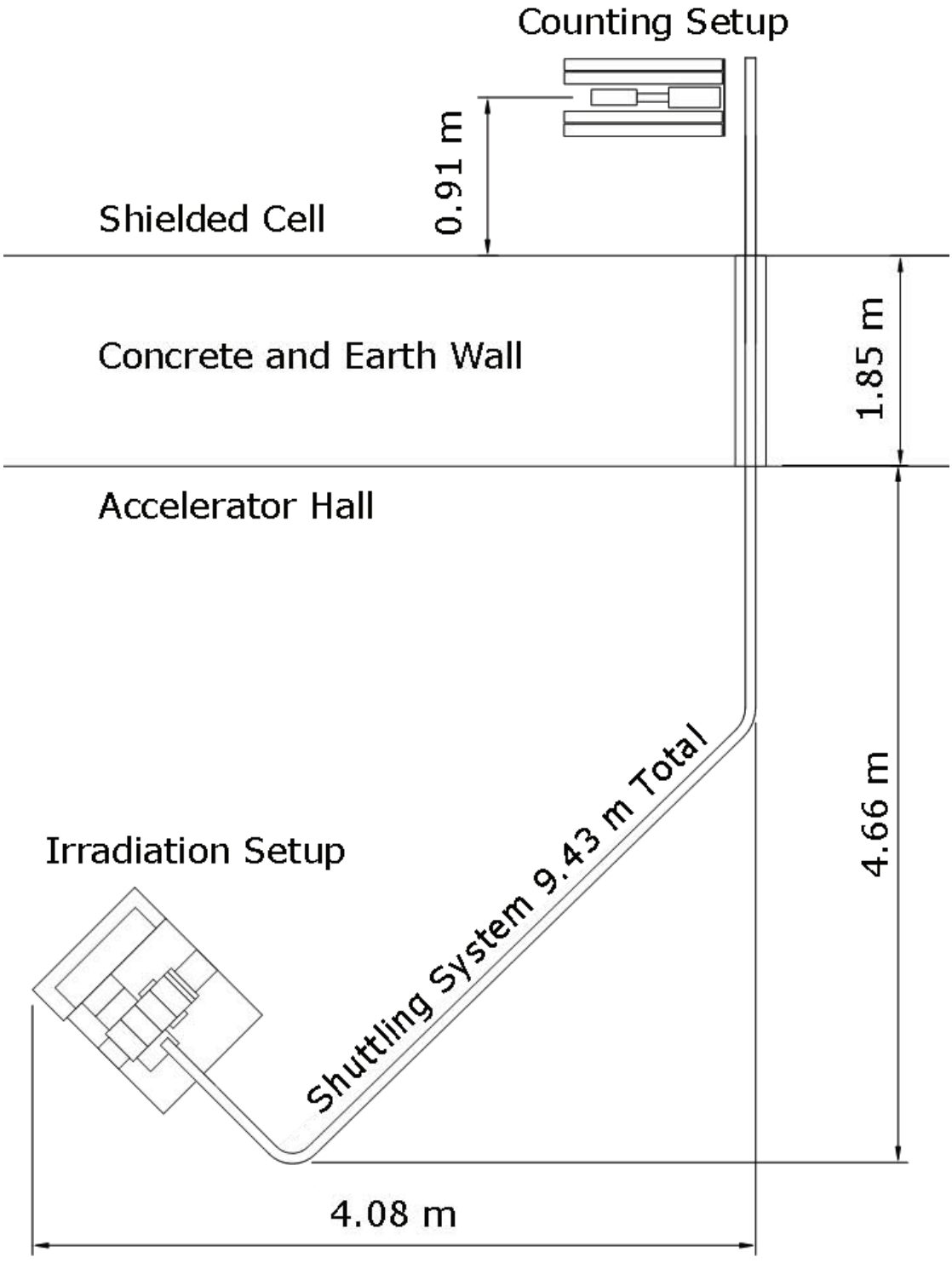

Figure 3.3: Schematic of the overall experimental setup. The irradiation setup is placed in the accelerator hall and the counting setup is placed in a shielded experimental cell. Connecting the two setups is a track style shuttling system that transits a total of 9.43 m from the irradiation position, through a penetration in a concrete and earthen wall into the experimental cell where the HPGe detector is housed.

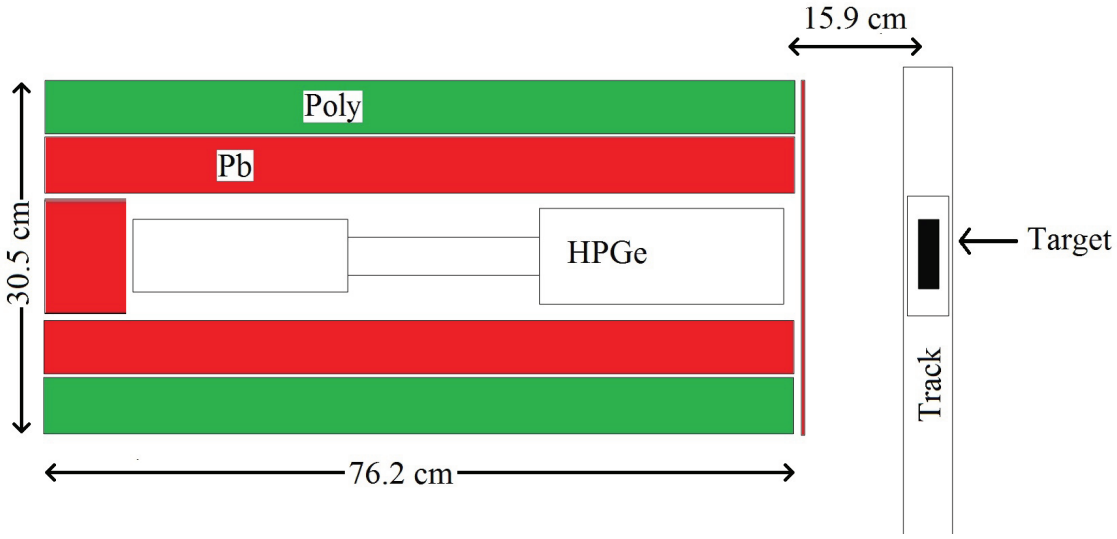

Figure 3.4: Cross-sectional schematic of the experimental setup used to detect β-delayed γ-rays from fission fragments as viewed from the top. The detector is encased in a 5 cm thick Pb hollow cylinder that is subsequently housed in a borated polyethylene block. A 6.35 mm Pb filter is placed over the face of the detector. The target (in black) is located on the shuttling system directly in front of the detector.

3.2 Fissile targets

The targets consisted of solid forms of ^{239}Pu and highly enriched ^{235}U oxide. The ^{239}Pu consisted of individual disk-shaped nuclear accident dosimeters (NADs). Each NAD contains an average of 0.974 g of ^{239}Pu with less than 1% variation in mass. The targets also contain small amounts of ^{238}Pu, ^{240}Pu, ^{241}Pu and ^{241}Am [34]. Table 3.1 details the average mass of each of these isotopes in the NADs. Each NAD is 2.45 cm in diameter and 1.0 mm in thickness with the contents encased in a uniform thin copper cladding. The individual NADs are then placed inside clear Air-Tite^{TM}quarter-sized coin containers. The ^{235}U sample consisted of 42.7% enriched uranium oxide in cylindrical pellet form. The mass is divided amongst six roughly equal sized pellets measuring ~4.88 mm by ~6.54 mm with the shorter dimension referring to the diameter of the planar surface. Table 3.2 shows the uranium pellet mass composition for a single pellet. These pellets were divided into sets of three each and stacked vertically into two polyethylene 2 mL microcentrifuge tubes.

Table 3.1: Average mass composition of a single ^{239}Pu NAD as of 11/18/2014 [34].

Isotope	Mass (g)
^{238}Pu	$5.22 \cdot 10^{-5}$
^{239}Pu	$9.74 \cdot 10^{-1}$
^{240}Pu	$5.49 \cdot 10^{-2}$
^{241}Pu	$2.70 \cdot 10^{-4}$
^{241}Am	$3.65 \cdot 10^{-3}$

Table 3.2: Average mass composition of a single ^{235}U cylinder.

Isotope	Mass (g)
^{235}U	$4.64 \cdot 10^{-1}$
^{238}U	$6.23 \cdot 10^{-1}$

Table 3.3: Composite target composition and total masses.

Target	Target Composition	Total Mass g	Relative ^{239}Pu %	Relative ^{235}U %
A	2.9 g ^{239}Pu	2.9 g	100	0
B	2.8 g ^{235}U + 1.0 g ^{239}Pu	3.8 g	26.3	73.7
C	2.8 g ^{235}U + 2.9 g ^{239}Pu	5.7 g	50.9	49.1
D	2.8 g ^{235}U	2.8 g	0	100

Composite targets were formed by placing these samples on and in a 2.54 cm × 5.08 cm × 7.62 cm low-density, $\sim 3.0 \cdot 10^{-2}$ g·cm^3, polyethylene foam holder. Table 3.3 details the four target's composition including total fissile mass and relative ^{239}Pu and ^{235}U concentrations. The relative ^{239}Pu concentrations of each of the four targets were: 0%, 26.3%, 50.9% and 100%. This allowed for two pure targets and two mixed targets to test various analysis methods. With the collection of spectra of each component individually, energy spectra and photopeaks of a mixed target were compared to spectra of one or both of its individual constituents and structure unique to that constituent were identified.

A typical target orientation is shown in Figure 3.5. This is Target C from Table 3.3 and contains 2.8 g of ^{235}U and 3 NADs totalling 2.9 g of ^{239}Pu. The ^{235}U and ^{239}Pu are arranged in the same manner for Targets A and D with ^{235}U and ^{239}Pu being absent, respectively. Target B differs in that only one ^{239}Pu NAD is present and is centered directly between the ^{235}U on the face of the holder. The capsules containing the

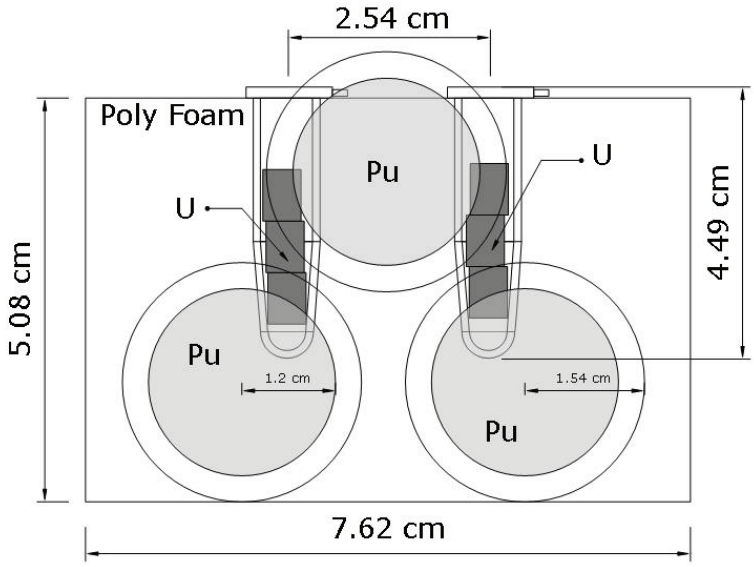

Figure 3.5: Schematic of a typical target containing 2.8 g ^{235}U and 2.9 g of ^{239}Pu (Target C). The outline of the polyethylene foam sample holder ($5.08 \times 7.62 \times 2.54$ cm) is shown along with the capsules containing ^{235}U which rest interior to the sample holder. The three ^{239}Pu NADs rest on the exterior of the polyethylene sample holder. The ^{235}U and ^{239}Pu are arranged in the same manner for Targets A and D with ^{235}U and ^{239}Pu being absent, respectively. Target B differs in that only one NAD is present and is centered directly between the ^{235}U.

^{235}U are imbedded in the holder with their centers a distance of 2.54 cm apart. The ^{239}Pu NADs are placed on the "front" of the sample holder closest to the detector. This geometry also places the ^{239}Pu NADs on the face of the holder closest to the Be neutron converter when in the irradiation position. Four targets containing varied amounts of ^{239}Pu and ^{235}U were made for inspection.

3.3 Data collection

Figure 3.6 shows a schematic of the data collection system. The high-purity germanium detector's preamplifier divides the signal into two outputs. This allowed for two amplifier and analog to digital converter (ADC) pairings and, subsequently, fast/slow acquisition comparisons with an identical detector signal. For one channel,

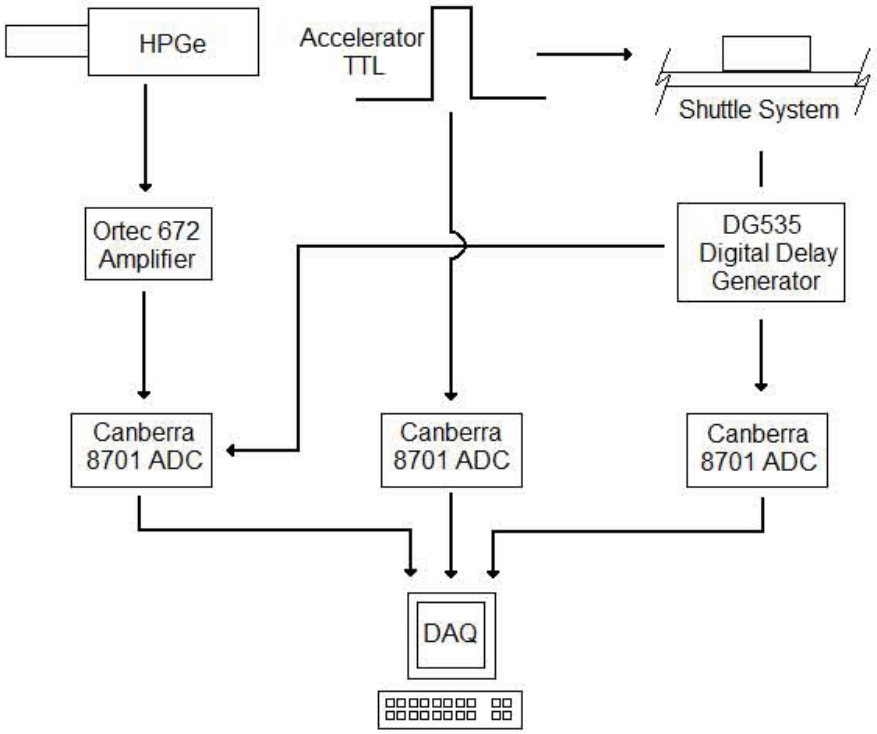

Figure 3.6: Schematic of the data acquisition system. Only the "slow" output is shown from the HPGe detector.

an Ortec 973U ultra high-rate spectroscopy amplifier was used in conjunction with a Canberra 8715. This amplifier and ADC pairing formed the fast channel. The other detector signal was put through an Ortec 672 amplifier and Canberra 8701 ADC pair which comprised the slow channel.

Pulse shaping by both the fast and slow channel's amplifiers is done by passing the detector pulse through a successive series of high-pass and low-pass filters. In the case of the slow channel's Ortec 672 amplifier, a single low-pass filter is followed by a series of high-pass filters [24, 35]. This converges the pulse shape to a Gaussian [24]. Shaping time on this amplifier was set to 6 μs. Once the pulse is shaped and amplified it, passes to the Canberra 8701 ADC. The Canberra 8701 ADC is a Wilkinson type ADC which compares the input voltage with the voltage produced by charging a

capacitor with a constant current source [24, 36, 37]. A comparator then determines when the voltage of the capacitor is equal to the height of the incoming pulse. Once the comparator determines that the voltages are equal, the capacitor is discharged linearly with time. While the capacitor is discharging, a gate is opened which allows for a constant rate clock to be counted. In the case of the Canberra 8701 ADC, the clock rate is 100 MHz. Because the discharging of the capacitor is linear with respect to time, the total number of clock ticks is linearly related to the height of the original detector pulse.

For the fast channel, the Ortec 973U ultra high-rate amplifier acts in a gated integrator mode with a short, 3 μs, integration time [38]. This amplifier contains a series of low-pass filters followed by a second series of high-pass filters [24]. This configuration results in a trapezoidal pulse shape with a flat top [24, 38]. This pulse shape decreases effects caused by variations in charge collection times in HPGe detectors which create a ballistic deficit between the actual pulse height and the shaped pulse height for Gaussian shaped pulses [24]. The pulse is then integrated by a capacitor linked to an active circuit [24]. The integration is terminated at the end of the set, 3 μs, integration time by discharging the capacitor. The amplified and shaped signal is then passed to the Canberra 8715 ADC. The Canberra 8715 ADC has fixed dead time which enables fast recording of high count rate spectra [39]. To achieve this fast conversion time, the ADC utilizes the successive approximation method to determine pulse height [40]. This method uses a series of comparators with ever narrowing voltage ranges [24]. For example, the first comparator may determine if the voltage of a given pulse was above or below 5 V, half the maximum amplitude of a NIM amplifier signal [24]. If it was, voltage equal to half the range of the ADC, 5 V, would be subtracted from the pulse height and the pulse would be sent to the next stage. If it lies below this threshold, the pulse would move to the second stage unadulterated. The second comparator would then determine if the pulse was above or below 2.5 V and so on. As the pulse travels through the series of comparators, a tally is kept of whether the pulse was above or below each time. At the end of the comparators the tally is summed to determine the pulse's channel. For 8192 channels there would be a set of thirteen stacked comparators to determine the channel a given pulse would

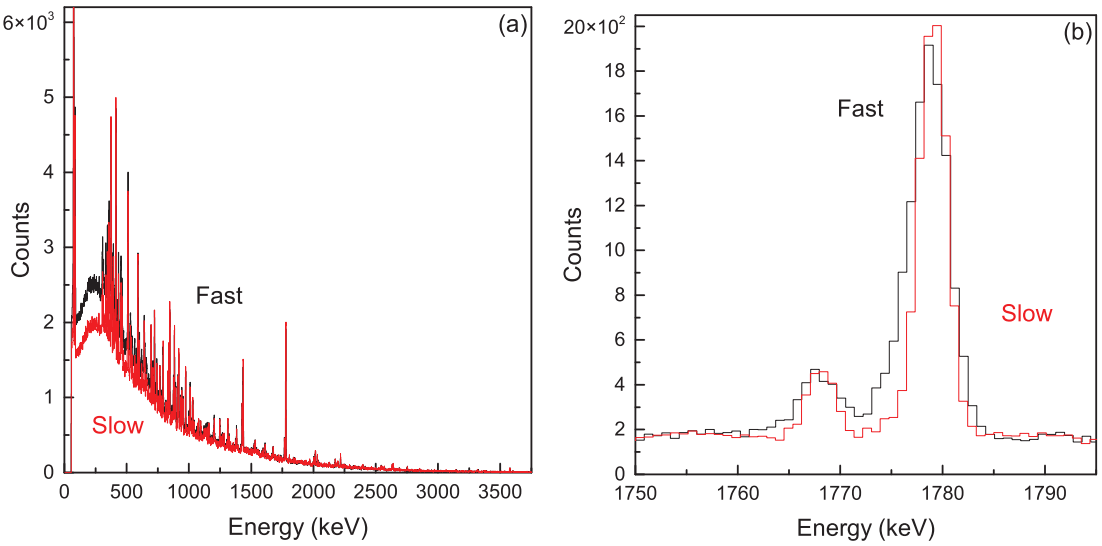

Figure 3.7: Delayed γ-ray energy spectra from neutron induced fission of ^{239}Pu. The irradiation and detection cycles were each 300 s with 22 s transit time between the irradiation station and detector. Energy spectra were collected using both the fast and slow channels from the data acquisition system.

be counted in.

Information from both ADCs was then processed through a multi-parameter data acquisition system which enabled data storage and real-time visualization of the energy spectra. This acquisition system allows for the recording of this data in event-by-event mode, with events assigned timestamps in 50 ns increments. Figure 3.7 shows portions of a ^{239}Pu delayed γ-ray energy spectrum collected with both the fast and slow channels. The fast data acquisition channel has $\sim$19% more total counts in the spectrum. However, Figure 3.7.b shows that utilizing the fast channel results in a decrease in resolution. In this instance, the full width at half maximum of the 1778 keV peak is greater in the fast channel, 4.52 keV compared to 3.20 keV. Because high throughput is desired and the detector resolution is still significant compared to many other types of detectors, the fast channel is primarily used for data analysis.

In conjunction with data from the high-purity detector, information about the accelerator and positioning of the targets was also collected. Figure 3.8 shows a schematic of the information collected and relative timing thereof. During irradiation,

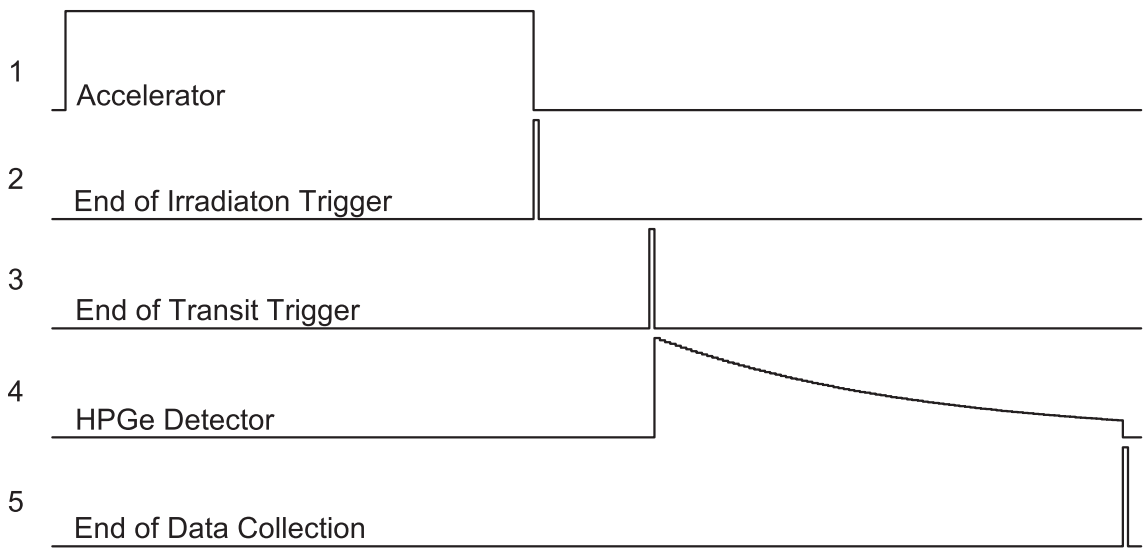

Figure 3.8: Schematic representation of the acquisition systems triggers and data collection. (1) The accelerator is on during the irradiation cycle. (2) At the end of the irradiation cycle a trigger initiates the shuttling system. (3) Once the target is in the counting position a trigger enables the HPGe detector ADC and begins the collection of the delayed γ-ray spectrum (4). (5) At the end of data collection the ADC gate is switched off and a trigger is sent to the shuttling system to reset and begin the process again. All five signals are recorded by the data acquisition system.

the accelerator gun trigger is collected by the acquisition system. Once the irradiation is complete, the accelerator sends a pulse to the shuttling system. This pulse tells the system to begin transiting the target to the detector location. Once the target arrives at the detector, an end-of-travel (EOT) pulse is sent to the digital delay generator. From the delay generator, the EOT pulse is recorded by the data acquisition system and a gate on the ADC is opened allowing the collection of spectra by the acquisition system. Once data collection has ceased, the gate on the detector ADCs is closed and a trigger is sent to the shuttling system to begin the cycle again. Because the detector acquisition is gated to acquire only when the target is in the count position, the amount of undesirable room background and influences from the irradiation scheme are reduced. All the pulses and triggers shown in Figure 3.8 are recorded by the data acquisition system. Because all this information is collected by the same system and

stored in the same file, the accelerator irradiation structure, sample transit time and energy spectra are all available for data analysis, time cuts and spectrum playback in a readily retrievable source.

Chapter 4

Results

4.1 Irradiation Structure Optimization

Multiple irradiation and counting time structures were investigated for optimization. Table 4.1 lists the irradiation, detection and shuttle times for these structures. These structures were repeated several times per sample to increase statistics over that of a single irradiation. Both short (tens of seconds) and long (minutes) timescales were examined at two accelerator frequencies. A low-frequency of 33 Hz and a high-frequency of 132 Hz were used. Increasing the frequency of the irradiation increases the irradiation intensity, thus, increases the measurable number of delayed γ-rays. However, lower-frequencies are often necessary to reduce the detector dead time and enable better spectra collection. Unfortunately, not all time structures could have a short, 21 s, shuttle time. Optimally, the shuttling time would be as small as possible to reduce the time fission fragments have to decay prior to reaching the detector. However, this was not possible due to time constraints and the availability of equipment used to shuttle the target following irradiation.

The yield of high-energy delayed γ-rays has been used to discern the presence of fissionable material in the past [3, 10]. In an effort to determine which of the irradiation and count time structures in Table 4.1 is optimum for the detection of fissile material, the yield of delayed γ-rays above 3 MeV was initially used as a marker for effectiveness of the irradiation structure. Figure 4.1 shows the yield of β-delayed

Table 4.1: Investigated target time structures.

Irradiation Time s	Transit Time s	Count Time s	Irradiation Frequency Hz
90	21	90	132
300	40	300	132
900	30	1800	33

γ-rays above 3 MeV as a function of each irradiation structure for 2.9 g of ^{239}Pu. The first structure to be investigated was 900 s/1800 s. This structure matches that of previous experiments conducted without the aid of a shuttling system and acts primarily as a benchmark to prior experiments. Due to its low yield and long time structure, which limits the detection of short-lived fission fragments, it was rejected in favor of shorter irradiation and counting structures. The irradiation structure of 90 s/90 s appears to be optimum for capturing delayed γ-rays in this setup. This structure results in a 16.3% higher yield of high-energy delayed γ-rays over that of the next closest structure.

The other available irradiation structure was 300 s/300 s. This structure, however, has a significant disadvantage compared to the 90 s/90 s structure. The 90 s/90 s structure has a greatly decreased shuttling time, 19 s shorter. The low shuttling time in the 90 s/90 s structure was done by increasing the power available to the motor. Because the motor was not rated for this power level, it was only done for the 90 s/90 s structure. In the 90 s/90 s structure, the target transits the distance from irradiation to the HPGe detector before many short-lived fission fragments can decay. This enables the detection of even shorter-lived fission fragments. For the isotope ^{106}Tc with a half-life of 36 s, 30% of the intensity is lost in the 19 s of transit time remaining for the 300 s/300 s structure. For isotopes with half-lives around one minute or less this effect is significant. If the shuttling time were decreased to 21 s for the 300 s/300 s irradiation structure, many of the short-lived fission fragments would not decay prior to detection. However, because the acquisition time is longer, many of these γ-rays may be buried within the background negating the effects of the shorter shuttling time.

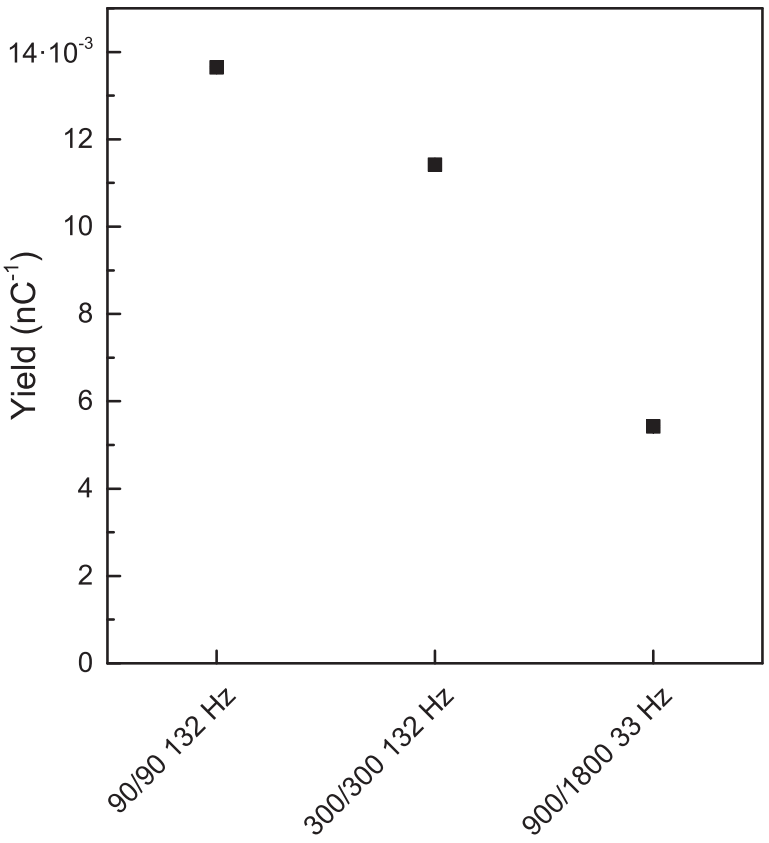

Figure 4.1: The delayed γ-ray yield above 3 MeV for ^{239}Pu in each of the irradiation structures listed in Table 4.1. Error bars are indicative of 1σ standard deviation.

Figure 4.2 shows the intensity weighted cumulative percentage of delayed γ-rays as a function of half-life for thermal neutron induced fission of ^{239}Pu and ^{235}U. While many fission fragments in the low-energy region have long half-lives, on the order of years, the spectra above 3 MeV are dominated by short-lived fission fragments with half-lives on the order of tens of seconds [14, 15]. Fully $\sim$30% of the γ-ray yield above 3 MeV is due to fission fragments with half-lives of less than 5 s and $\sim$72% of the yield is due to fission fragments with half-lives less than 90 s. Because many of the high-energy γ-rays are emitted by significantly short-lived fission fragments, to capture these γ-rays the sample should transit the distance from the irradiation position to detection position as quickly as possible. Because a large majority of the γ-ray yield, 50%, is due to fission fragments with half-lives less than $\sim$35 s,

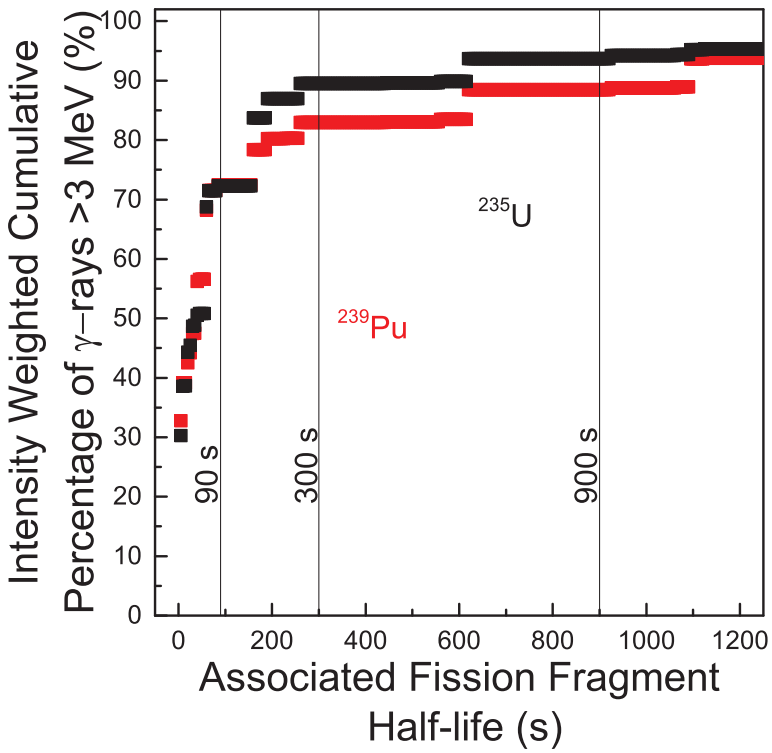

Figure 4.2: The intensity weighted cumulative percentage of the cumulative fission fragment γ-ray emissions as a function of half-life for thermal neutron induced fission [14, 15].

equilibrium for these fragments is reached after ∼100 s. Increasing the irradiation period to 300 s does increase the γ-ray yield equilibrium by ∼20%. However, with a longer shuttling period, many of the γ-rays from short-lived fission fragments do not reach the detector.

Figure 4.3 shows the yield of three delayed γ-ray lines as a function of irradiation period for fission fragments with half-lives of 36 s (^{106}Tc), 4.3 minutes (^{90m}Rb) and 10.3 minutes (^{95}Y). The yield of long-lived fission fragments such as ^{95}Y increases steadily as the irradiation period is increased. For ^{106}Tc, with a half-life of 36 s, the yield drops by ∼62% from the 90 s irradiation period to the 300 s irradiation period. This variation in the irradiation and detection scheme can highlight specifically desired fission fragments. Since a large portion of the γ-ray yield is due to short-lived fission fragments with half-lives on the order of 10's of seconds, it is likely

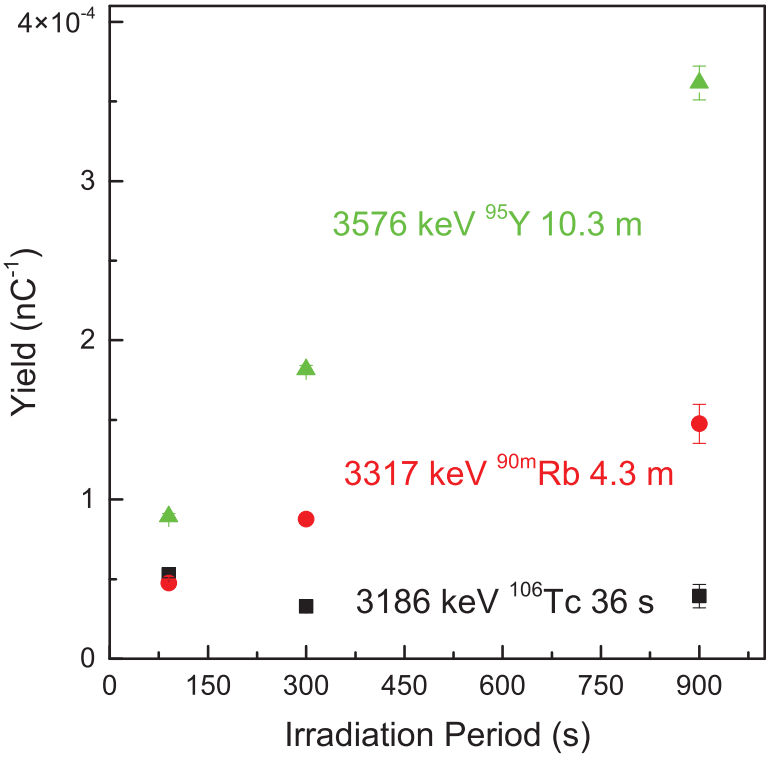

Figure 4.3: The yield of the 3186 keV line from ^{106}Tc, the 3317 keV line from ^{90m}Rb and the 3576 keV line from ^{95}Y as a function of irradiation period.

advantageous to use short irradiation, transit and detection times.

4.1.1 Energy Spectra and Fragment Identification

Prior research and modeling has gone into identifying photopeaks and their respective fission fragments[1] [28,33]. With modeling, the timing structure of the irradiation and counting cycles must be included to account for fission fragment buildup and decay to accurately portray the delayed γ-ray spectrum. From these models, photopeaks can be identified by accessing the database of discrete γ-rays and their yields, since these yields were utilized in the making of the model spectrum. This reduces the time involved in identifying photopeaks and also reduces the chances of misidentifi-

[1]The modeling of this specific research is outside the scope of this dissertation and is done by a third party. For further reading see the dissertation *Delayed Gamma-Ray Assay for Nuclear Safeguards* by V. Mozin

cation. Because many isotopes share similar or even identical photopeaks, those with significantly overlapping intensities can be identified and eliminated from analysis if necessary. This information can also be utilized in analysis to reduce the number of free parameters in a Gaussian fit by importing the known energy of the photopeaks into the algorithm.

Figure 4.4 shows a portion of the ^{239}Pu energy spectra collected from the HPGe detector for each of the three irradiation structures listed in Table 4.1. From the figure, it is clear that all the spectra share relatively similar photopeak structure but with some differences. While the photopeaks of the longer-lived fission fragments like ^{95}Y are present in all the spectra, those of the shorter-lived are not significantly present in the 900 s/1800 s irradiation. While photopeaks from fission fragments like ^{106}Tc (36 s) and ^{91}Rb (58 s) are present in both the 90 s/90 s and the 300 s/300 s, they have a significantly larger intensity in the spectrum from the 90 s/90 s irradiation structure. Neither of these short-lived fission fragments appear to be present in the 900 s/1800 s spectrum with any significant intensity. In the ^{239}Pu spectrum from the 900 s/1800 s the only photopeak not present in the spectra from the short irradiation structure is the 2971 keV photopeak from ^{142}La.

Figure 4.5 shows a portion of the ^{235}U energy spectra collected from the HPGe detector for each of the three irradiation structures listed in Table 4.1. In a similar fashion to that of the ^{239}Pu spectra presented in Figure 4.4, short-lived fission fragments such as ^{91}Rb appear to only be present with a significant intensity in the energy spectra collected from the short irradiation structures. Similarly, the photopeak at 2971 keV photopeak from ^{142}La is only present in the spectrum from the 900 s/1800 s structure. Absent from the spectra from ^{235}U is the presence of photopeaks from the short-lived fission fragment ^{106}Tc.

Figures 4.6 through 4.14 show comparisons of delayed γ-ray spectra from 2.9 g of ^{239}Pu and 2.8 g of ^{235}U from moderated neutron induced fission in the three irradiation structures. These figures show the energy range from 2650 keV to 6650 keV in 1 MeV increments. Spectra from the 90 s/90 s structure is shown in Figure 4.6, Figure 4.7 and Figure 4.8; the 300 s/300 s structure is shown in Figure 4.9, Figure 4.10 and Figure 4.11; and the 900 s/1800 s structure is shown in Figure 4.12, Figure 4.13

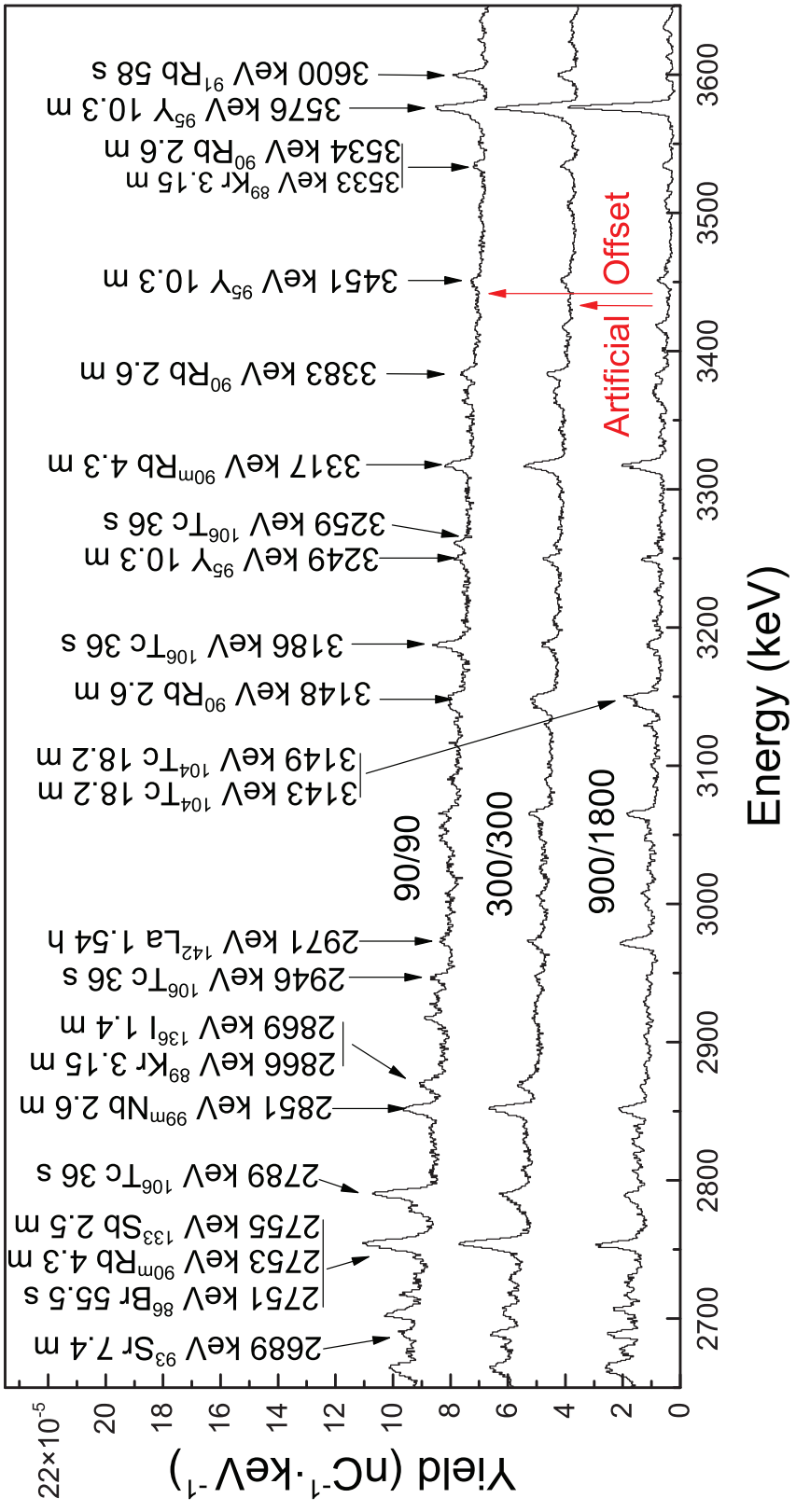

Figure 4.4: Energy spectrum from 2650 keV to 3650 keV of delayed γ-rays from 2.9 g of ^{239}Pu irradiated with moderated neutrons in the 90 s/90 s, 300 s/300 s and 900 s/1800 s irradiation time structures. Spectra are summed over multiple iterations of the irradiation, transit and counting times for a total of $\sim$4 hours each. Notable energy peaks are labeled with their energy and originating fission fragment and its half-life. Artificial offsets of $3 \cdot 10^{-5}$ nC^{-1}·keV^{-1} and $6 \cdot 10^{-5}$ nC^{-1}·keV^{-1} have been added to the 300 s/300 s and 90 s/90 s spectra to enable better visualization of the data, respectively.

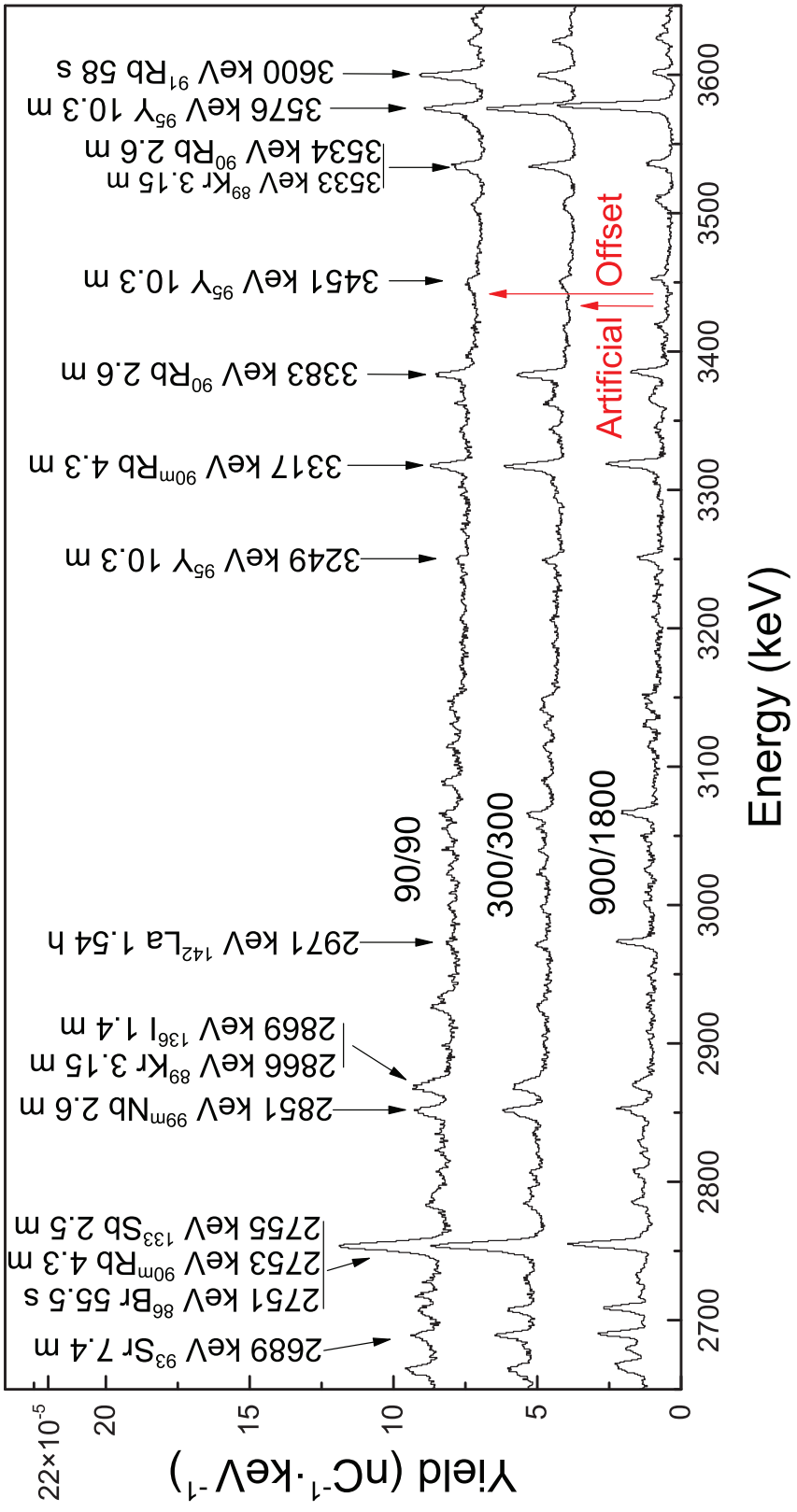

Figure 4.5: Energy spectrum from 2650 keV to 3650 keV of delayed γ-rays from 2.8 g of ^{235}U irradiated with moderated neutrons in the 90 s/90 s, 300 s/300 s and 900 s/1800 s irradiation time structures. Spectra are summed over multiple iterations of the irradiation, transit and counting times for a total of $\sim$4 hours each. Notable energy peaks are labeled with their energy and originating fission fragment and its half-life. Artificial offsets of $3 \cdot 10^{-5}$ nC^{-1}·keV^{-1} and $6 \cdot 10^{-5}$ nC^{-1}·keV^{-1} have been added to the 300 s/300 s and 90 s/90 s spectra to enable better visualization of the data, respectively

and Figure 4.14. These energy spectra have been normalized to total charge on the tungsten radiator and an artificial offset has been added to the ^{239}Pu spectra to enable differentiation of features.

There are a significant number of photopeaks throughout the energy range from 2650 to 5650 keV in all three data sets. At lower-energies, many of the photopeaks overlap. Across each of the data sets, the photopeaks at ∼2753 keV, ∼2867 keV and ∼3533 keV are shared by two or more fission fragments. As energy increases the number of overlapping photopeaks decreases. While not listed, there are many photopeaks that do, indeed, overlap, however, the intensities of the other contributing fission fragments are often not significant, less than a few percent. It is also evident that as energy increases, the total number of photopeaks decreases. This trend is also common across the three data sets. Beyond ∼3600 keV the number of photopeaks available for analysis and subsequent isotope identification decreases significantly. Two factors influence this: decreased detector efficiency at high-energy and reduced emissions of these γ-rays in this higher regime [14, 15, 24].

Photopeaks from fission fragments with half-lives on the order of several minutes, like ^{95}Y (10.3 minutes) or ^{90}Rb (2.6 minutes), are common across all the irradiation and detection structures. While photopeaks from these fission fragments are present with a diminished intensity in spectra from short irradiation structures, their intensity is still quite significant. However, photopeaks from the short-lived fission fragments, like ^{106}Tc (36 s) and ^{91}Rb (58 s), are only intense in the short, 90 s/90 s and 300 s/300 s, irradiation/detection structures and not in the 900 s/1800 s irradiation/detection structure. Similarly, photopeaks from the long-lived fission fragments, like ^{104}Tc (18.2 minutes) and ^{142}La (1.54 h), are only present in the long, 900 s/1800 s, irradiation/detection structure. This shows that by modifying the irradiation and detection structure, emissions from different fission fragments can be highlighted. Potentially, γ-rays from either short-lived or long-lived fission fragments may provide a unique and discernable fission signature of a desired isotope.

Figure 4.12 to 4.14 shows the energy range from 2650 to 5650 keV in 1 MeV increments of delayed γ-ray spectra collected from 2.9 g of ^{239}Pu and 2.8 g of ^{235}U using the 900 s/1800 s irradiation structure. While longer-lived fission fragments

are present in these spectra as compared to the shorter irradiation structures, these spectra are not very unique when compared to each other. In fact, photopeaks across the energy range are duplicated in both spectra with often similar intensities. The 90 s/90 s and 300 s/300 s irradiation/detection structures, however, have several distinct fission fragments present in either the ^{239}Pu or the ^{235}U spectra. Photopeaks from ^{106}Tc are only found with significant intensity in the ^{239}Pu spectra from the short irradiation/detection structures. This fission fragment appears to be an indicator for the presence of ^{239}Pu and, thus, the capability to measure it is desirable.

While several factors influence optimization of the irradiation scheme, of the available data set, the 90 s/90 s structure appears to be optimum. This irradiation structure has a high delayed γ-ray yield of short-lived fission fragments. This increased yield is due to the short irradiation, detection and transfer times. With $\sim$72% of the γ-rays emitted by ^{239}Pu and ^{235}U above 3 MeV having associated half-lives less than 90 s, it is with these that unique signatures of the original fissioning isotope are likely to be found [10,14,15]. Ideally, the target would not be transported over any distance to reduce the opportunity for any fission fragment to decay before its γ-rays could be detected. This would place the detector next to the target and within a short distance of the ^{9}Be radiator. While not impossible, exposure to neutron radiation causes significant damage to the HPGe detector reducing its effectiveness significantly [24].

4.2 Peak Ratio Analysis

Peak ratio analysis (PRA) has been a proven technique for isotopic identification for many applications including photon activation analysis, delayed γ-rays and nuclear resonance fluorescence [9,25–28]. Provided that a material emits multiple photopeaks with unique and differing intensities when under inspection, that material can be identified by the unique ratio of those peaks. Each of the targets listed in Table 3.3 was subjected to multiple iterations of the 90 s/90 s irradiation scheme. Several unique and common photopeaks were identified across the target spectra for analysis. These peaks were selected over a wide energy range from 2753 keV to 3600 keV and are the result of several fission fragments. Table 4.2 lists the energy of the photopeaks

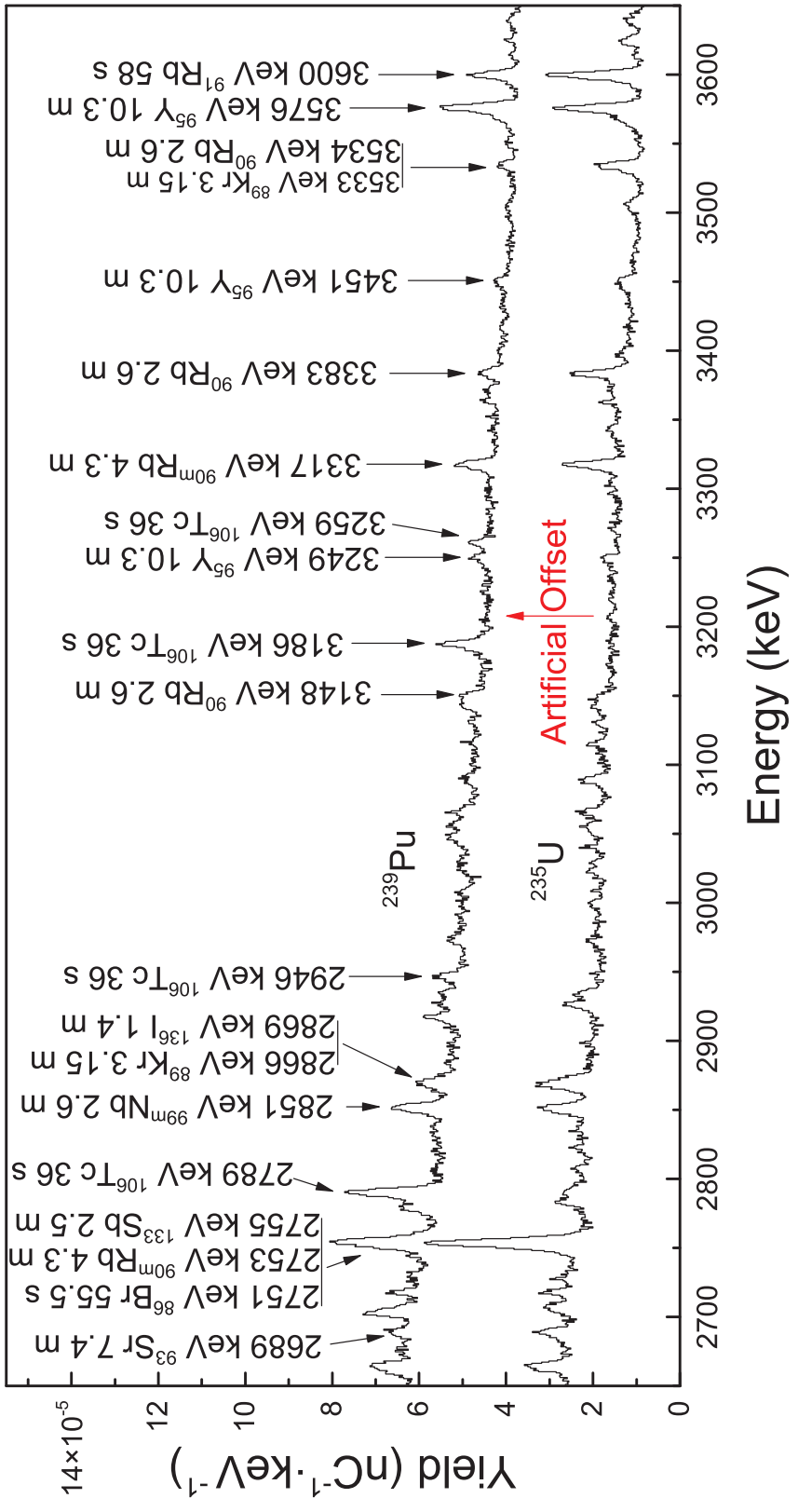

Figure 4.6: Energy spectrum from 2650 keV to 3650 keV of delayed γ-rays from 2.8 g of ^{235}U and 2.9 g of ^{239}Pu irradiated with moderated neutrons in the 90 s/90 s irradiation time structure. Spectra are summed over multiple iterations of 90 s irradiation, 21 s transit and 90 s counting times for a total of $\sim$4 hours each. Notable energy peaks are labeled with their energy and originating fission fragment and its half-life. An artificial offset of $3 \cdot 10^{-5}$ nC^{-1}·keV^{-1} has been added to the ^{239}Pu spectrum to enable better visualization of the data.

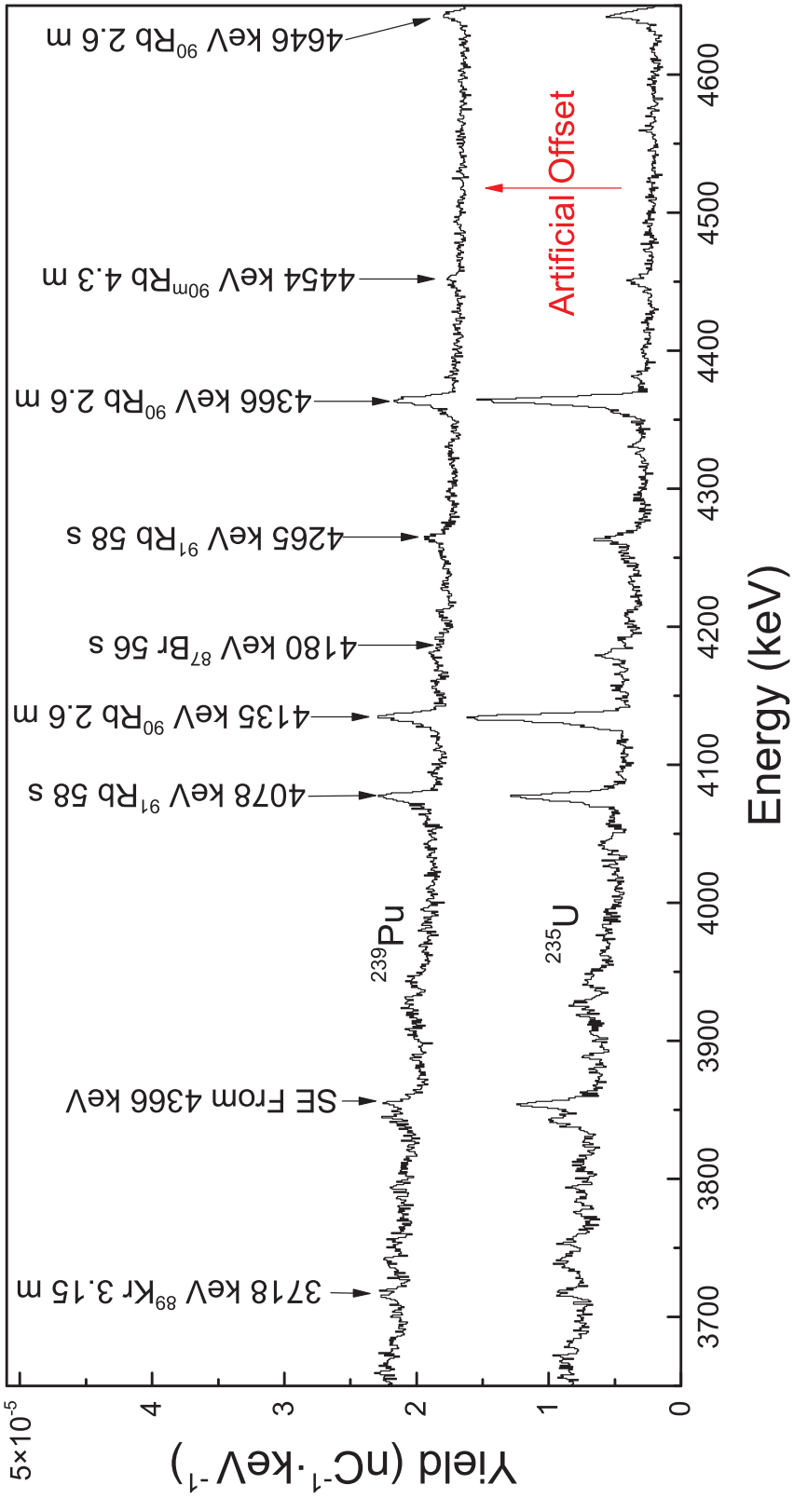

Figure 4.7: Energy spectrum from 3650 keV to 4650 keV of delayed γ-rays from 2.8 g of ^{235}U and 2.9 g of ^{239}Pu irradiated with moderated neutrons in the 90 s/90 s irradiation time structure. Spectra are summed over multiple iterations of 90 s irradiation, 21 s transit and 90 s counting times for a total of $\sim$4 hours each. Notable energy peaks are labeled with their energy and originating fission fragment and its half-life. Notable single escape peaks are marked "SE" with their corresponding incident photopeak. An artificial offset of $1.5 \cdot 10^{-5}$ nC^{-1}·keV^{-1} has been added to the ^{239}Pu spectrum to enable better visualization of the data.

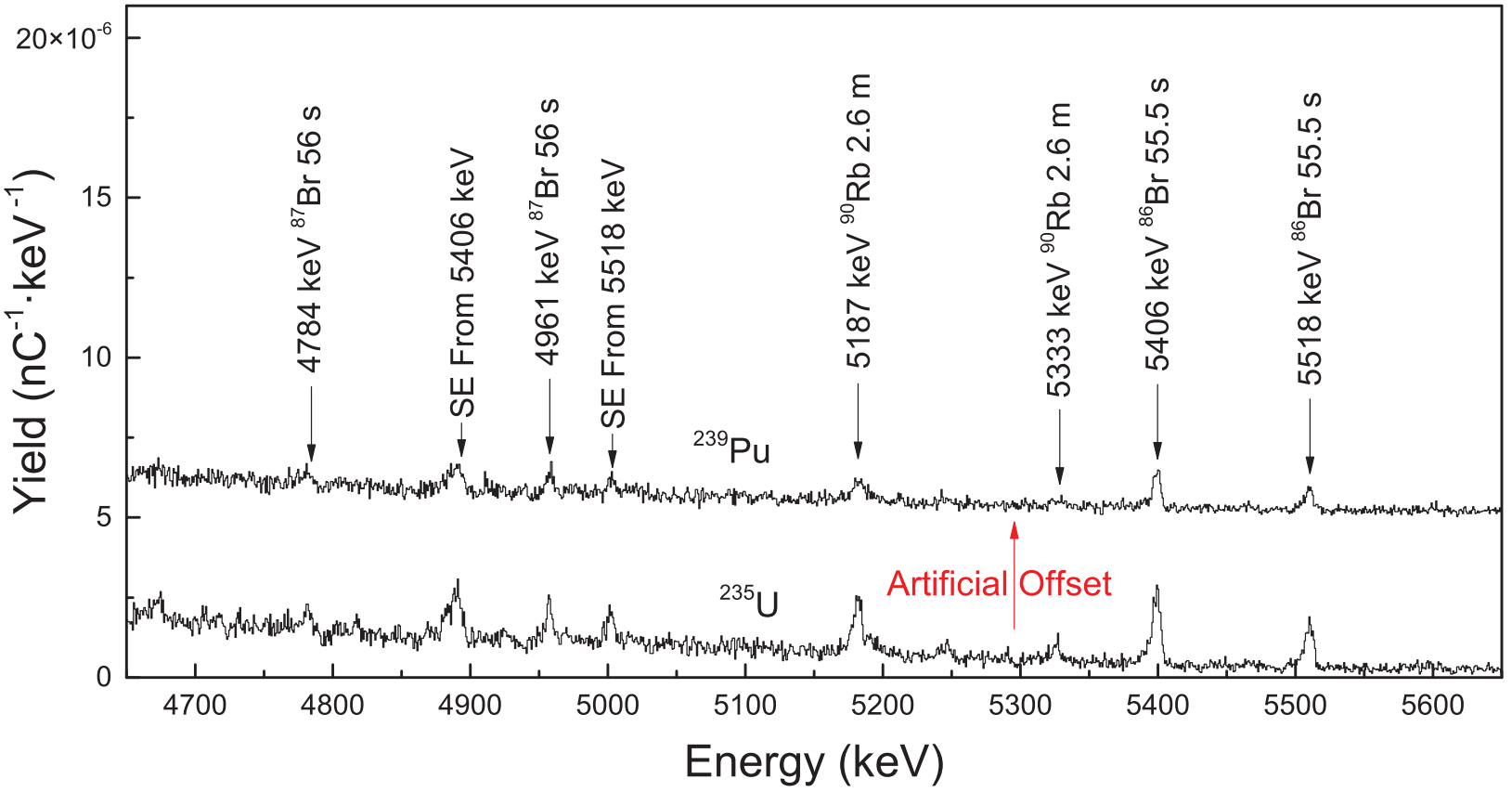

Figure 4.8: Energy spectrum from 4650 keV to 5650 keV of delayed γ-rays from 2.8 g of ^{235}U and 2.9 g of ^{239}Pu irradiated with moderated neutrons in the 90 s/90 s irradiation time structure. Spectra are summed over multiple iterations of 90 s irradiation, 21 s transit and 90 s counting times for a total of $\sim$4 hours each. Notable energy peaks are labeled with their energy and originating fission fragment and its half-life. Notable single escape peaks are marked "SE" with their corresponding incident photopeak. An artificial offset of $5 \cdot 10^{-6}$ nC^{-1}·keV^{-1} has been added to the ^{239}Pu spectrum to enable better visualization of the data.

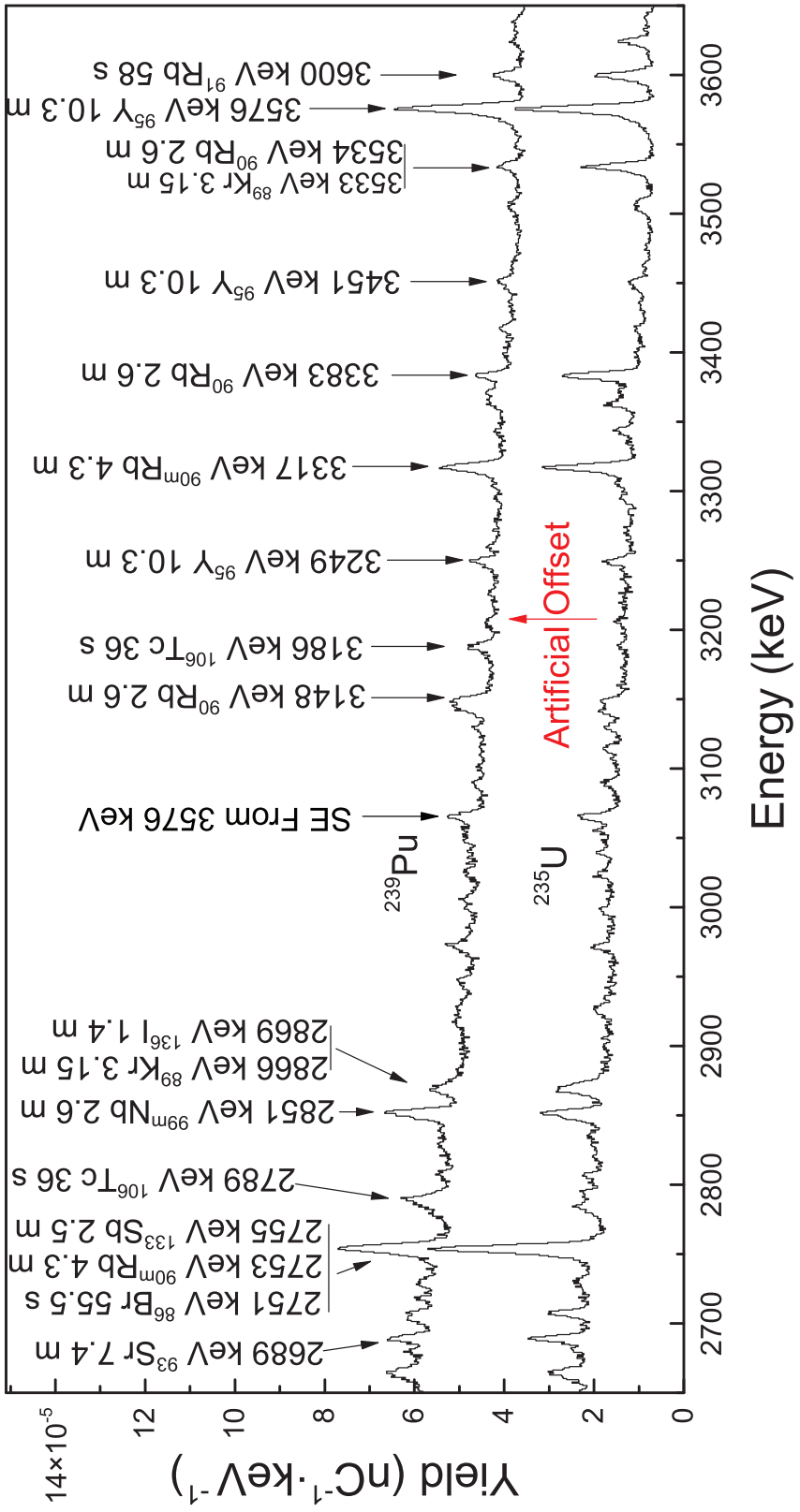

Figure 4.9: Energy spectrum from 2650 keV to 3650 keV of delayed γ-rays from 2.8 g of ^{235}U and 2.9 g of ^{239}Pu irradiated with moderated neutrons in the 300 s/300 s irradiation time structure. Spectra are summed over multiple iterations of 300 s irradiation, 40 s transit and 300 s counting times for a total of ∼2.5 hours each. Notable energy peaks are labeled with their energy and originating fission fragment and its half-life. Notable single escape peaks are marked "SE" with their corresponding incident photopeak. An artificial offset of $3 \cdot 10^{-5}$ nC^{-1}·keV^{-1} has been added to the ^{239}Pu spectrum to enable better visualization of the data.

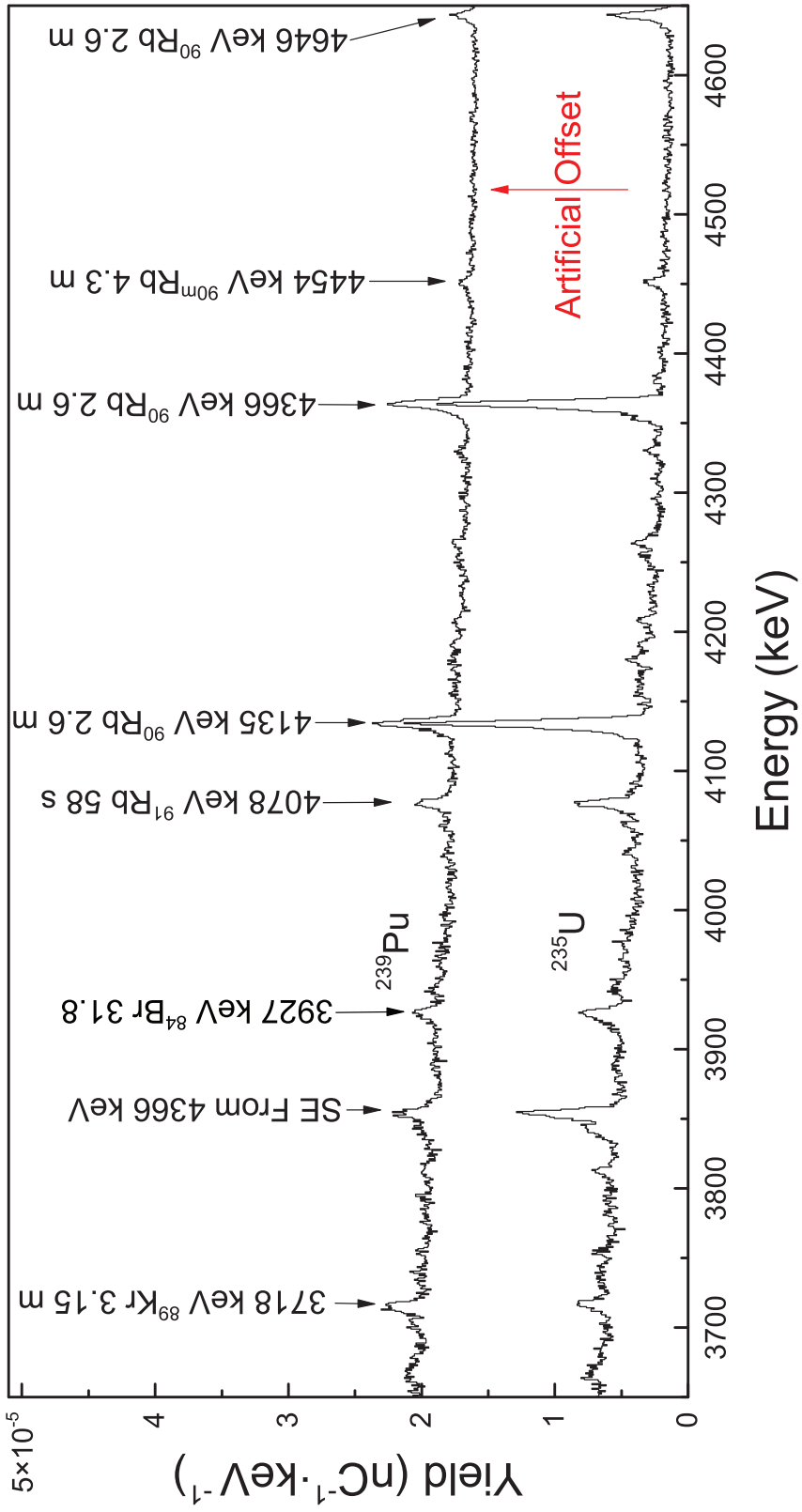

Figure 4.10: Energy spectrum from 3650 keV to 4650 keV of delayed γ-rays from 2.8 g of ^{235}U and 2.9 g of ^{239}Pu irradiated with moderated neutrons in the 300 s/300 s irradiation time structure. Spectra are summed over multiple iterations of 300 s irradiation, 40 s transit and 300 s counting times for a total of $\sim$2.5 hours each. Notable energy peaks are labeled with their energy and originating fission fragment and its half-life. Notable single escape peaks are marked "SE" with their corresponding incident photopeak. An artificial offset of $1.5 \cdot 10^{-5}$ nC^{-1}·keV^{-1} has been added to the ^{239}Pu spectrum to enable better visualization of the data.

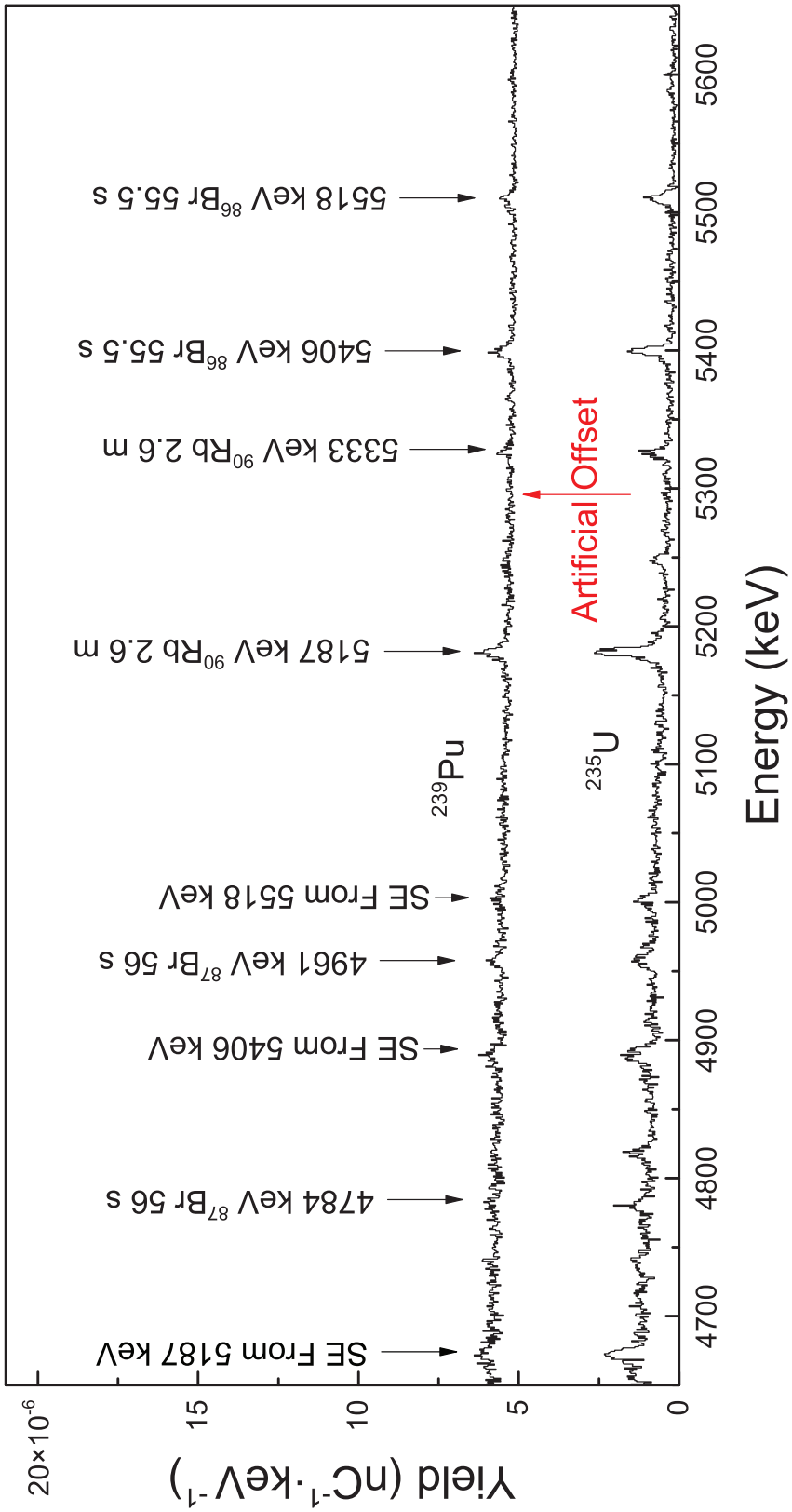

Figure 4.11: Energy spectrum from 4650 keV to 5650 keV of delayed γ-rays from 2.8 g of ^{235}U and 2.9 g of ^{239}Pu irradiated with moderated neutrons in the 300 s/300 s irradiation time structure. Spectra are summed over multiple iterations of 300 s irradiation, 40 s transit and 300 s counting times for a total of ∼2.5 hours each. Notable energy peaks are labeled with their energy and originating fission fragment and its half-life. Notable single escape peaks are marked "SE" with their corresponding incident photopeak. An artificial offset of $5 \cdot 10^{-6}$ nC^{-1}·keV^{-1} has been added to the ^{239}Pu spectrum to enable better visualization of the data.

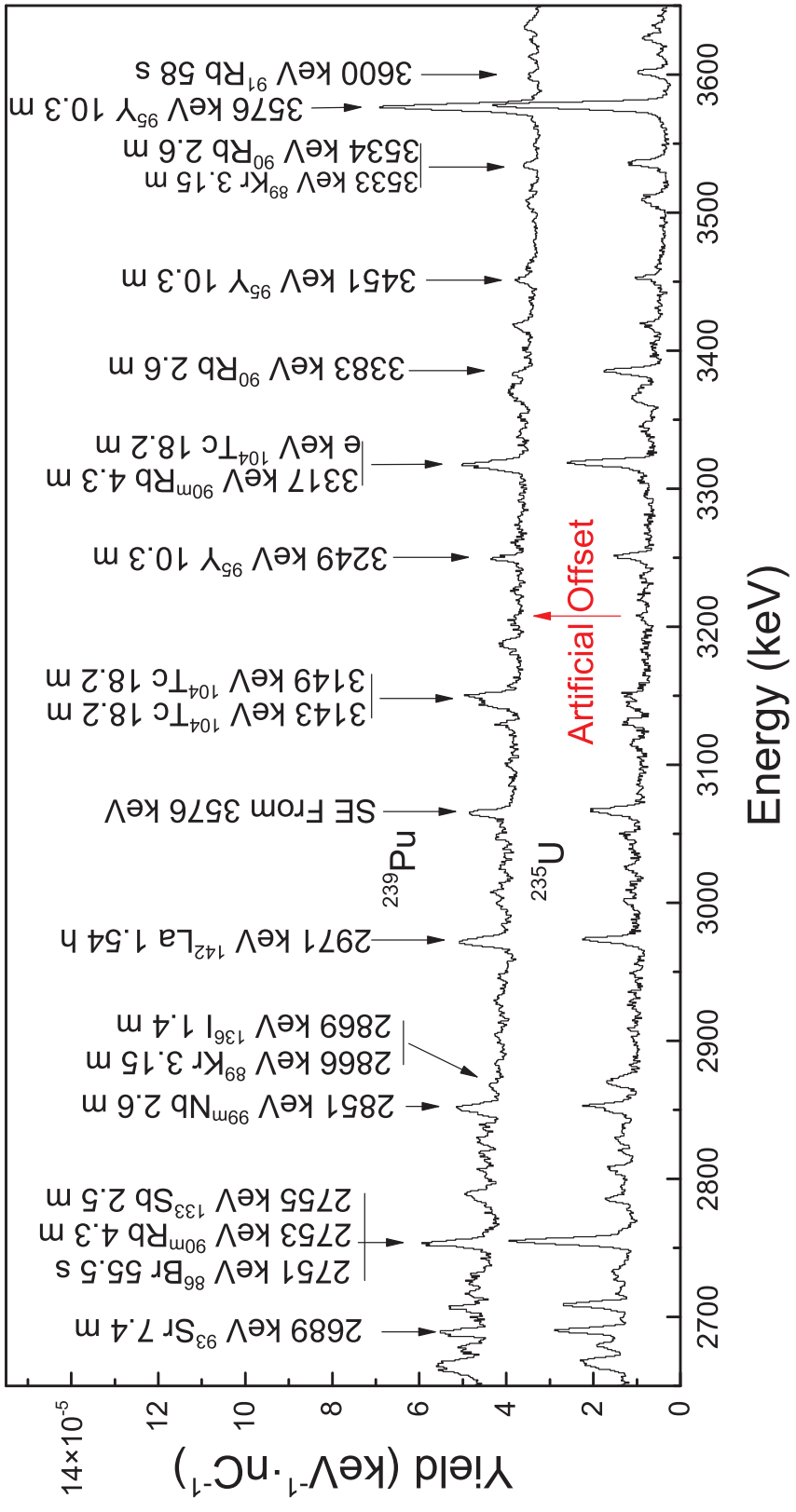

Figure 4.12: Energy spectrum from 2650 keV to 3650 keV of delayed γ-rays from 2.8 g of ^{235}U and 2.9 g of ^{239}Pu irradiated with moderated neutrons in the 900 s/1800 s irradiation time structure. Spectra are summed over multiple iterations of 900 s irradiation, 30 s transit and 1800 s counting times for a total of ∼4 hours each. Notable energy peaks are labeled with their energy and originating fission fragment and its half-life. Notable single escape peaks are marked "SE" with their corresponding incident photopeak. An artificial offset of $3 \cdot 10^{-5}$ nC^{-1}·keV^{-1} has been added to the ^{239}Pu spectrum to enable better visualization of the data.

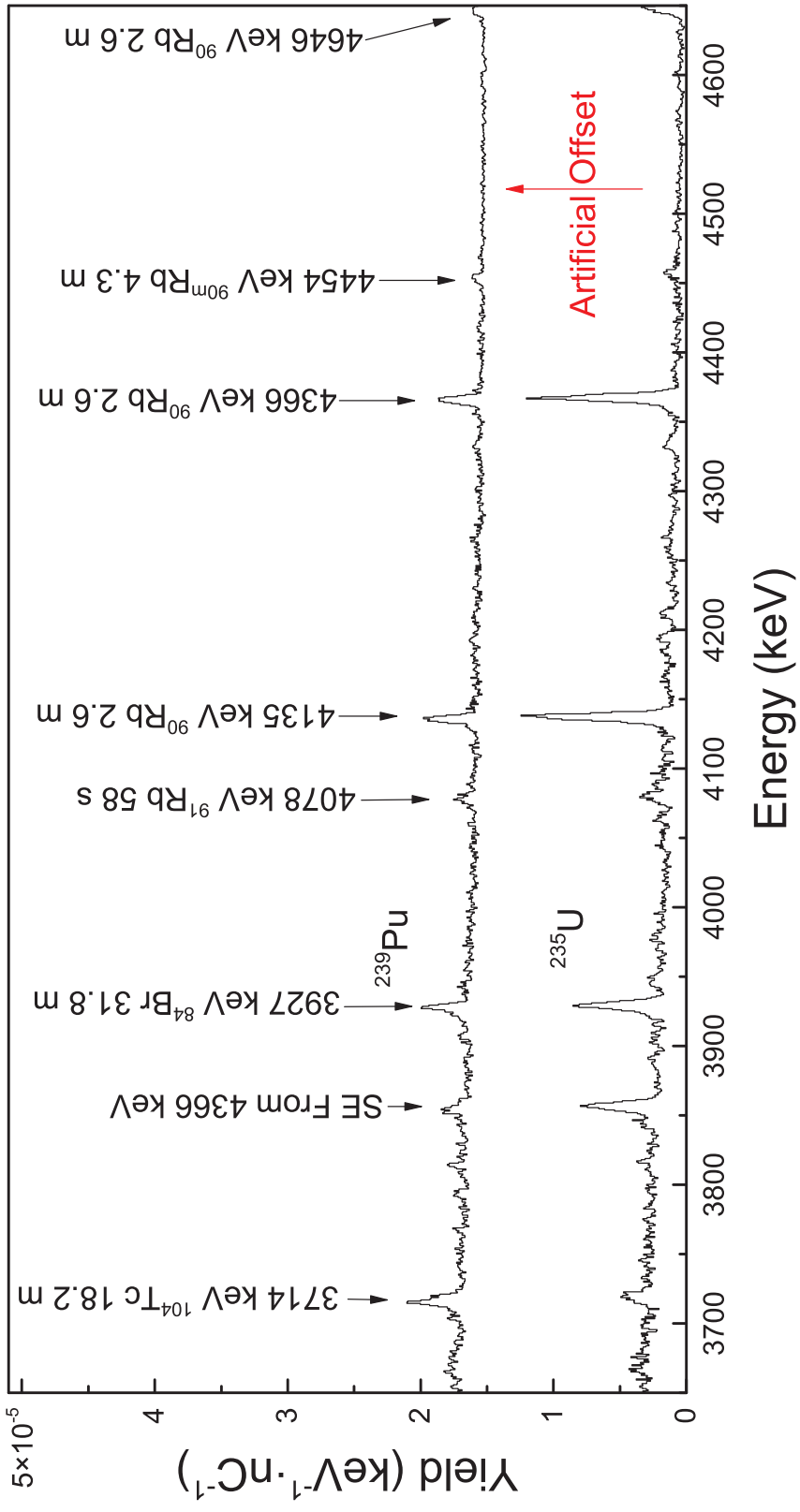

Figure 4.13: Energy spectrum from 3650 keV to 4650 keV of delayed γ-rays from 2.8 g of ^{235}U and 2.9 g of ^{239}Pu irradiated with moderated neutrons in the 900 s/1800 s irradiation time structure. Spectra are summed over multiple iterations of 900 s irradiation, 30 s transit and 1800 s counting times for a total of ∼4 hours each. Notable energy peaks are labeled with their energy and originating fission fragment and its half-life. Notable single escape peaks are marked "SE" with their corresponding incident photopeak. An artificial offset of $1.5 \cdot 10^{-5}$ nC^{-1}·keV^{-1} has been added to the ^{239}Pu spectrum to enable better visualization of the data.

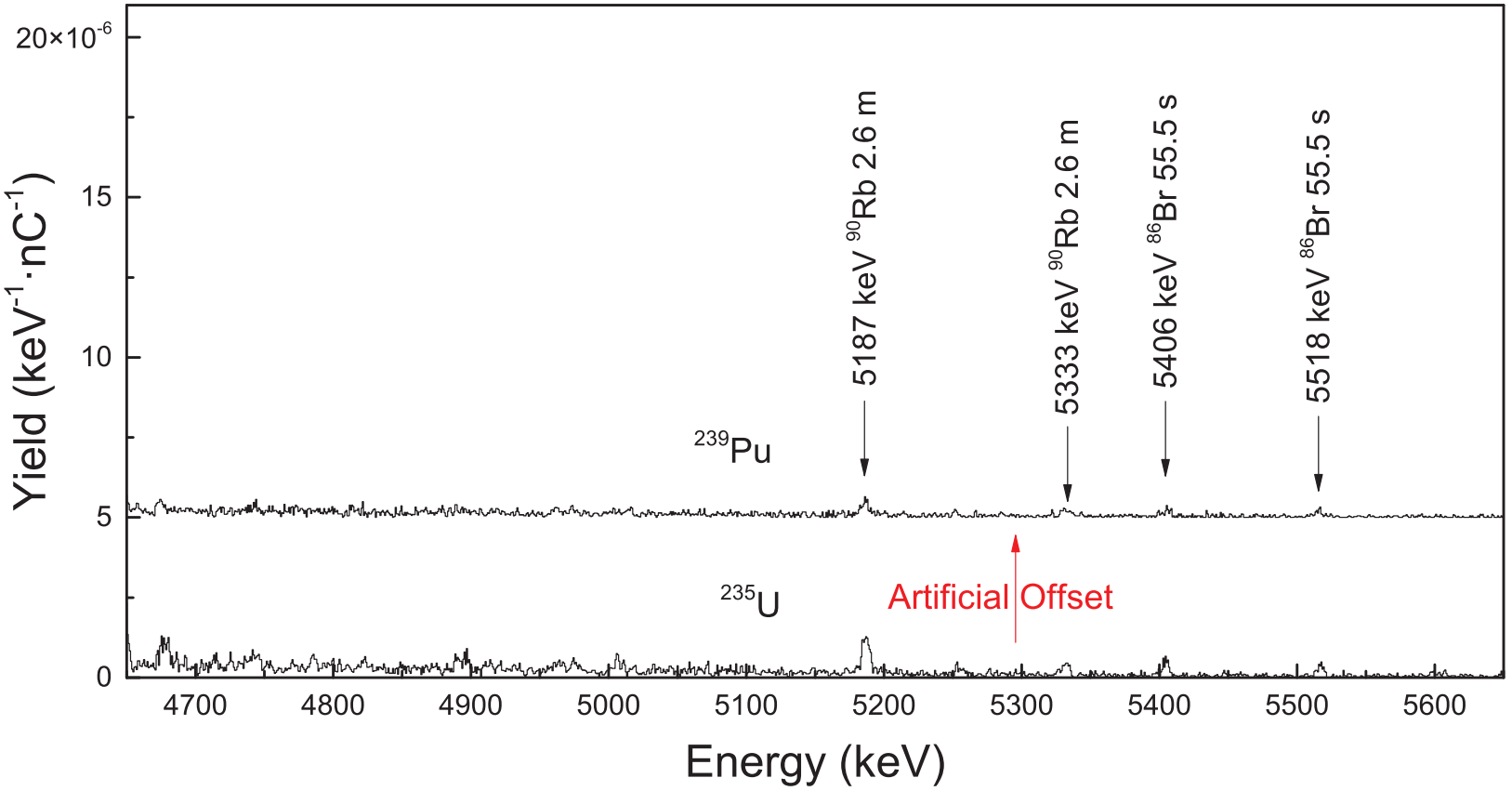

Figure 4.14: Energy spectrum from 4650 keV to 5650 keV of delayed γ-rays from 2.8 g of ^{235}U and 2.9 g of ^{239}Pu irradiated with moderated neutrons in the 900 s/1800 s irradiation time structure. Spectra are summed over multiple iterations of 900 s irradiation, 30 s transit and 1800 s counting times for a total of $\sim$4 hours each. Notable energy peaks are labeled with their energy and originating fission fragment and its half-life. An artificial offset of $5 \cdot 10^{-6}$ nC^{-1}·keV^{-1} has been added to the ^{239}Pu spectrum to enable better visualization of the data.

Table 4.2: Energy, dominant isotope and half-life of the photopeaks selected for the peak ratio analysis.

Energy keV	Isotope	Half-life s
2752.68	^{90m}Rb	258
2851.5	^{99m}Nb	156
2868.9	^{136}I	83.4
3186.40	^{106}Tc	35.6
3317.00	^{90m}Rb	258
3383.24	^{90}Rb	158
3532.88	^{89}Kr	189
3576.0	^{95}Y	618
3599.67	^{91}Rb	58.4

chosen for this analysis along with their respective dominant fission fragment. While many higher-energy photopeaks are present, most are emitted by fission fragments already represented in Table 4.2. As can be seen in this table the photopeaks selected are emitted by relatively short-lived fission fragments, many with half-lives on the order of minutes or less. These photopeaks also have energies above the limit of natural background, ∼2.6 MeV, and many are above the limit of background from spent nuclear fuel, ∼3 MeV.

Figure 4.15 shows the yield of each of the photopeaks listed in Table 4.2 determined from the spectra of pure samples of ^{239}Pu and ^{235}U for the 90 s/90 s irradiation structure. As shown in the figure, most of the photopeaks have a significantly higher yield for ^{235}U than for ^{239}Pu. This is the case for six of the nine selected photopeaks. However, two of the photopeaks selected appear with approximately the same yield for both isotopes, the 3576 keV photopeak from ^{95}Y and the 2851 keV photopeak from ^{99m}Nb and can be utilized as fiducial peaks to linearize the peak ratio function. One significant note is the 3186 keV line from ^{106}Tc which is the only photopeak selected that appears with a significantly larger intensity in the spectra from ^{239}Pu as compared to ^{235}U.

Once these peaks were selected, several ratios of their areas were taken. Figure 4.16

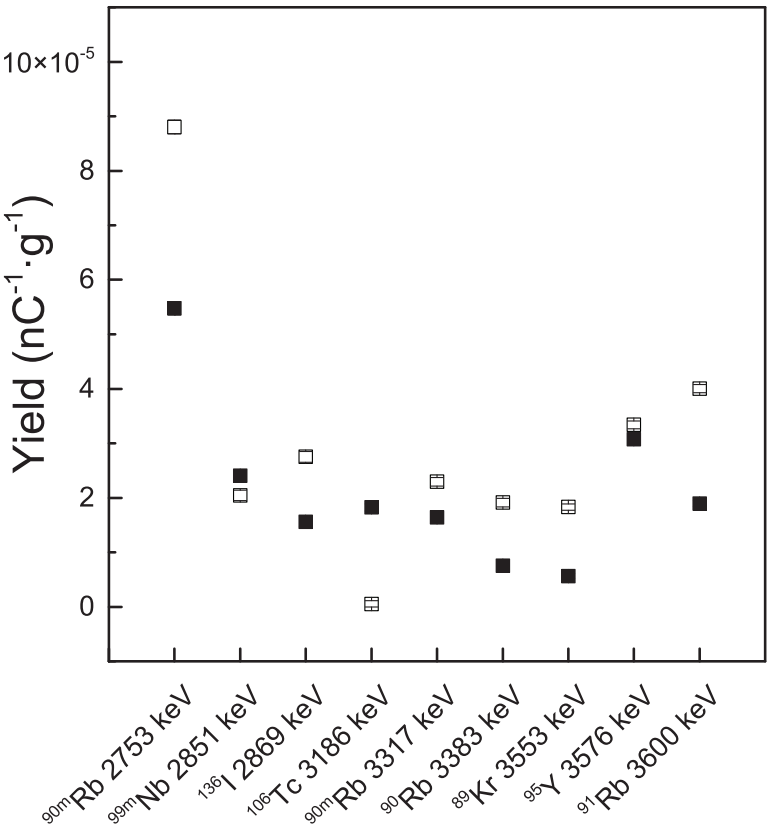

Figure 4.15: Yield of each of the photopeaks listed in Table 4.2 determined from spectra of 2.9 g of ^{239}Pu (■) and 2.8 g of ^{235}U (□) measured using the 90 s irradiation, 21 s transit and 90 s detection setup. Energy and dominant fission fragment for each photopeak is given. Error bars are representative of 1σ standard deviation.

shows the ratios of some of the peak combinations as a function of relative ^{239}Pu concentration. Each ratio shows a strong monotonic relationship with relative ^{239}Pu concentration and relatively low error. Many peak ratio errors are within 10% of the value with the exception being instances of photopeaks with very low statistics in one or two samples. This is due to the lack of that particular fission fragment in the target material. Instances of this include the 3186 keV photopeak from ^{106}Tc that is not present in a significant intensity in the delayed γ-ray spectrum of ^{235}U. In Figure 4.16.a the ratio was taken between the 2753 keV peak from ^{90m}Rb and the 3576 keV line from ^{95}Y. Figure 4.15 shows that the 3576 keV line from ^{95}Y has the

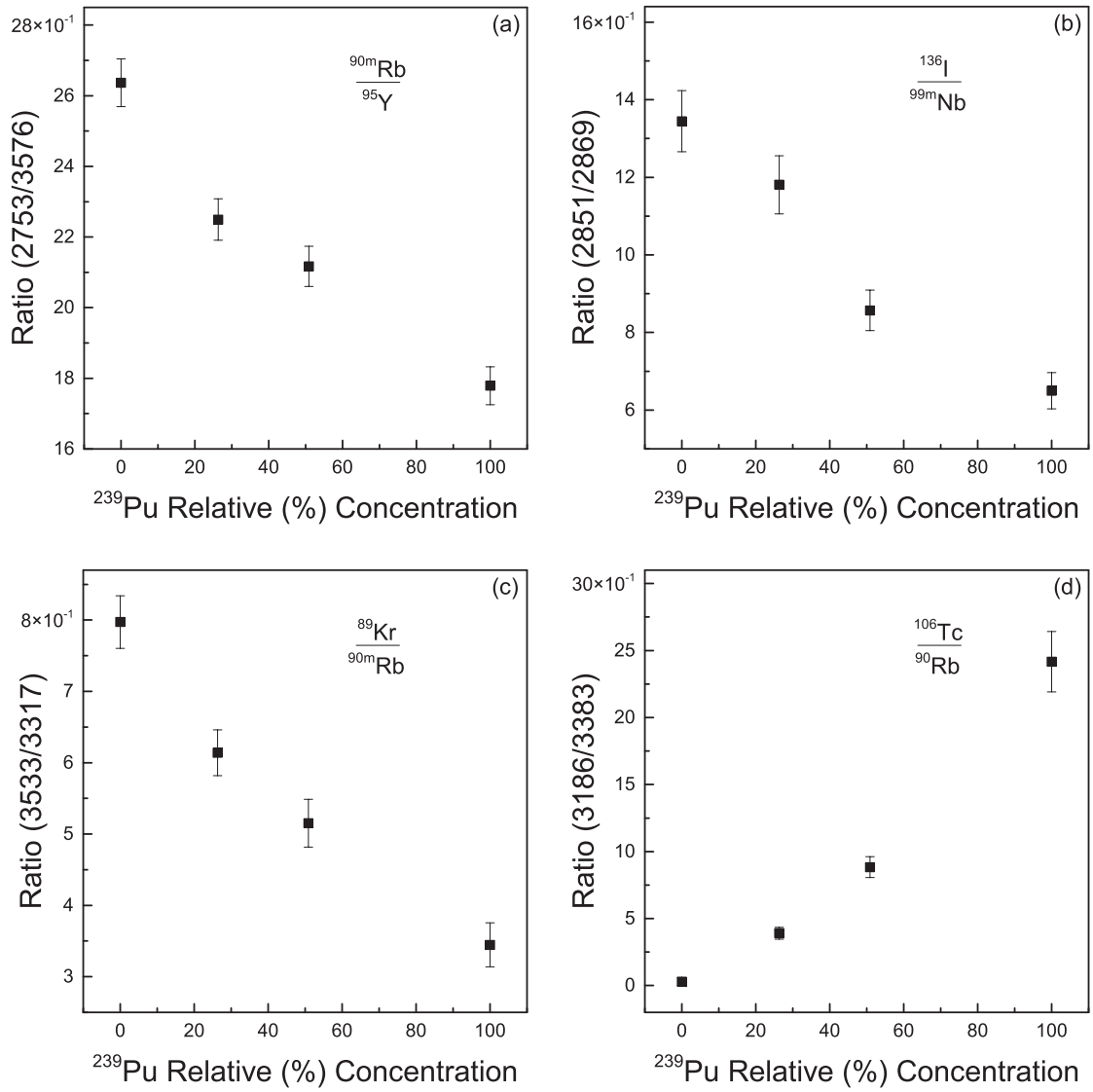

Figure 4.16: Ratios of several photopeaks ranging in energy from 2753 keV to 3600 keV as a function of relative ^{239}Pu concentration. Error bars are representative of 1σ standard deviation.

same yield for ^{239}Pu and ^{235}U and thus it can be utilized as a fiducial to produce a linear relationship when constructing a ratio. The 2753 keV peak from ^{90m}Rb shows a large yield when compared to the other peaks selected and a ∼60% higher intensity in the ^{235}U spectra than in ^{239}Pu. The ratio between these two peaks produces a strongly linear relationship with respect to relative ^{239}Pu concentration. The 2689 keV photopeak from ^{99m}Nb also holds the possibility of producing a linear relationship if used as a fiducial. Figure 4.16.b shows the ratio of the 2851 keV photopeak from ^{136}I with the ^{99m}Nb line in the denominator. The 2851 keV photopeak from ^{136}I is ∼80% larger in yield in the ^{235}U spectrum than in ^{239}Pu. This ratio, like that of Figure 4.15.a, also shows a strong monotonic and quite linear relationship with respect to relative concentration.

While construction of peak ratios is ideal and linear with the presence of a fiducial in the denominator, very few fiducials are present in the data. While 20% of the photopeaks selected have similar yields for both ^{239}Pu and ^{235}U, it may not always be possible to select a fiducial peak common to both isotopes. This is likely to become increasingly difficult in instances where more than two fissile materials are present. Figure 4.16.c and Figure 4.16.d show the results of ratios taken between photopeaks without the use of fiducial peaks. Figure 4.16.c shows the ratio of 3533 keV photopeak from ^{89}Kr with that of the 3317 keV photopeak from ^{90m}Rb. Both of these are present in both spectra of ^{235}U and ^{239}Pu with relatively large intensities. However, because these yields differ between that of ^{239}Pu and ^{235}U the ratio of these two photopeaks still produces a monotonic relationship capable of discerning the relative concentration of a mixed ^{239}Pu/^{235}U sample. It is also clear from Figure 4.16.c that this ratio is still quite linear with respect to relative concentration.

The ^{106}Tc fission fragment appears to be a good indicator as to the presence of ^{239}Pu, as it does not appear to be present in the pure ^{235}U spectrum. The ratio between the 3186 keV line from ^{106}Tc with the 3383 keV line from ^{90}Rb is shown in Figure 4.16.d. The 3383 keV line from ^{90}Rb is present in both the spectrum from ^{239}Pu and ^{235}U and is a relatively strong indicator of ^{235}U. The ratio between these peaks is representative of a strong indicator of the presence of ^{239}Pu taken with an indicator of ^{235}U. This ratio has a strong monotonic relationship with relative

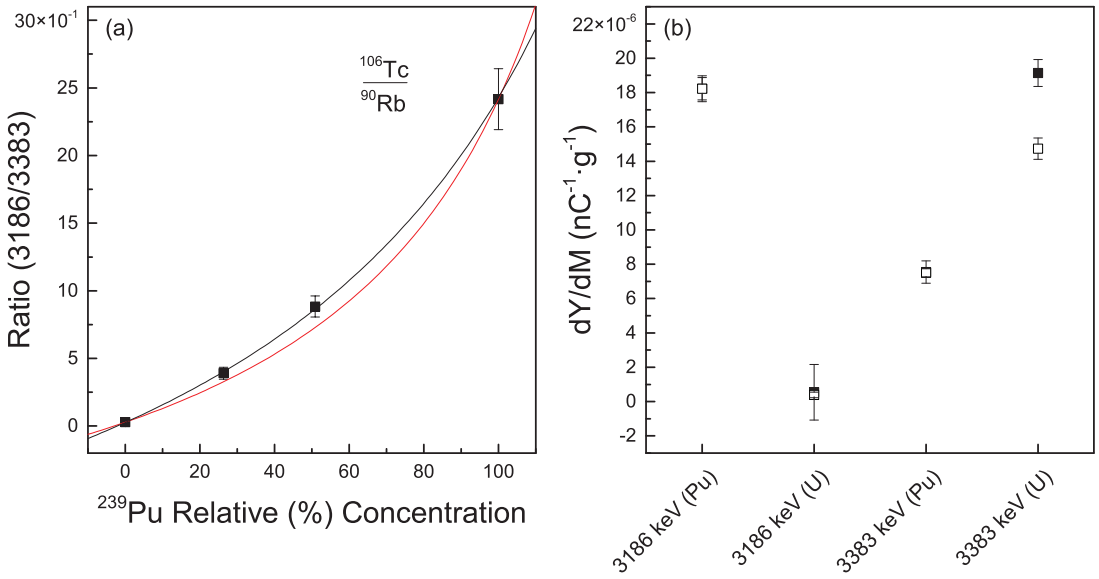

Figure 4.17: (a) Comparison of the predicted curvature (red) of the ratio of the 3186 keV line from ^{106}Tc and 3383 keV line from ^{90}Rb and the fit to the data (black). (b) The predicted dY/dm (■) values alongside the values derived from the fit (□) for the two peaks from both samples. Error bars are indicative of 1σ standard deviation.

^{239}Pu concentration with a slight curvature to the data as predicted. While it has been predicted in Chapter 2.3.1 that utilization of non-fiducial peaks would result in curvature with respect to relative concentration, both Figure 4.16.c and Figure 4.16.d still show quite linear relationships.

Applying a fit to the data shown in Figure 4.16.d yields a curve that translates the ratio of these two peaks into relative concentration. To do this, Equation 2.6 was used to produce the curve describing the data. Because there are so few data points and the equation has four free parameters the fit had to be "bootstrapped" using measured values from the pure samples for each parameter as initial conditions. Figure 4.17 shows the results of the fit to the data. Figure 4.17.a shows the predicted curvature alongside the fit of the function. As can be seen in Figure 4.17.a, the curve resulting from the fit follows the data points quite well. However, with so many free parameters and few data points, it is possible to apply any such equation to this data.

Figure 4.17.b shows the measured dY/dm values (■) compared with the results of the fitting algorithm (□) for the ratio of the 3186 keV line from ^{106}Tc and the

3383 keV line from ^{90}Rb. Three of the four dY/dm values are within error bars of their predicted yield. The only value significantly differing from predicted is that of the yield of the 3383 keV line produced from the fission of ^{235}U. This dY/dm value is $\sim$75% of its prediction and only results in a small modification to the curvature of the equation that defines this peak ratio. It is important to note, however, that with more data points the accuracy of this fit could be significantly improved and possibly eliminate the need for bootstraping.

Figure 4.18 shows the data transformed into relative concentration using the fit curve from Figure 4.17. The statistical errors near 100% relative concentration reduce in relative size while those near 0% increase in relative size. This is due to increasing sensitivity of the peak ratio as a function of relative concentration. This transformation thus results in the statistical error being relatively constant with concentration and results in an average statistical error of $\sim$3.75% relative concentration. This transformation also results in all the points laying within 1σ standard deviation from the true relative concentration. Similar transformations can be applied to other peak ratios and their combined information could be used to decrease the error associated with calculating the relative concentration.

4.2.1 Multi-Gaussian Fitting

Multi-Gaussian fitting is a requirement when multiple photopeaks are close enough in energy as to overlap. Figure 4.19 show a portion of energy spectra collected from the targets listed in Table 3.3 for the 90 s/90 s irradiation scheme. As can be seen in the figure, the photopeaks from ^{106}Tc overlap that of ^{91}Rb. Because the characteristics of the detector such as resolution and efficiency are known, as well as the intensity ratio between the two ^{106}Tc, the fitting algorithm only requires four free parameters to fit the cluster of three photopeaks. Of these parameters, two are required for a linear background underneath the photopeaks and only two are required for the three photopeaks themselves, in this instance one for the intensity of the ^{91}Rb peak and one for the linked intensities of the ^{106}Tc peaks.

Overlaid on Figure 4.19 are the results of multi-Gaussian fits performed on the

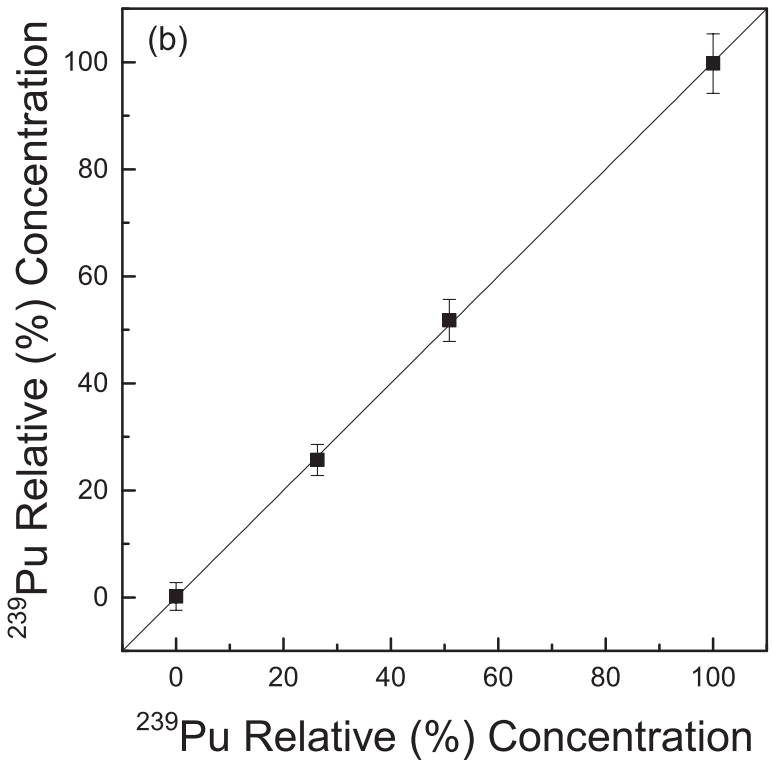

Figure 4.18: The results of transforming the ratio of the 3186 keV line from ^{106}Tc and the 3383 keV line from ^{90}Rb into relative concentration using the fit obtained in Figure 4.17.a. Error bars are indicative of 1σ standard deviation.

spectra. Because the two photopeaks from ^{106}Tc are close in energy they are assumed to share the same detector efficiency and resolution. Their intensities are thus linked through the branching ratio. The 2777 keV is 0.304 times the intensity of the 2789 keV photopeak. By fixing this intensity and using the known parameters of the detector, the free parameters utilized by the fit are reduced significantly. As can be seen in Figure 4.19, the results are a fit that follows closely that of the measured spectra. The main deviation exists between the cluster of photopeaks and the 2753 keV line. This produces an over-estimation of the background of as much as 7% of the yield in a given channel in this region and is likely due to photopeaks buried within the 2753 keV line. This photopeak is dominated by the 2753 keV from ^{90m}Rb, however, there exists two other significant lines near this energy, 2751 keV and 2755 keV from ^{86}Br and ^{133}Sb, respectively. Because the width and energy of the 2753 keV peak is

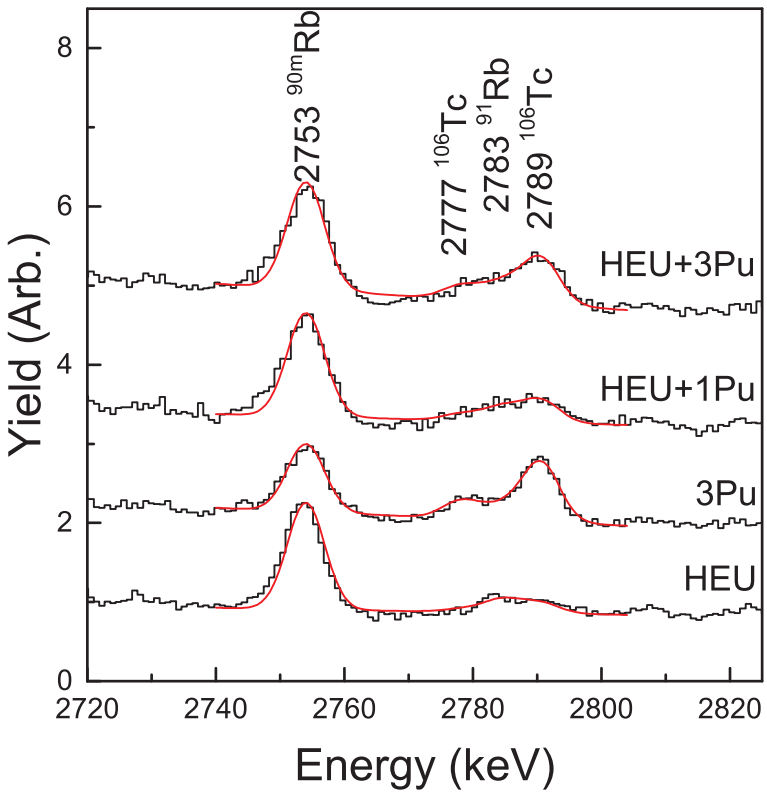

Figure 4.19: Portion of the energy spectra for the four targets listed in Table 3.3 taken utilizing the 90 s/90 s irradiation scheme. Four photopeaks are labeled with their respective energies. Three of these peaks, two from ^{106}Tc and one from ^{91}Rb overlap significantly and are difficult to resolve. The multi-Gaussian fits are overlaid on their respective energy spectra in red. Artificial offsets have been added to enable differentiation between spectra and their structures.

fixed within the algorithm, the algorithm does not move or expand the Gaussian to accommodate the inclusion of either of these two peaks. Thus, the linear background is likely increased to account for the extra counts in this region. Despite this the fitting algorithm is capable of discerning the cluster of three photopeaks successfully and the parameters used to define the 2783 keV peak from ^{91}Rb can then be extracted and used in PRA.

Figure 4.20.a shows the results of PRA performed using the 2789 keV photopeak from ^{106}Tc and the solitary 2753 keV photopeak from ^{90m}Rb. The results are encouraging and show a monotonic relationship as a function of relative ^{239}Pu concentration

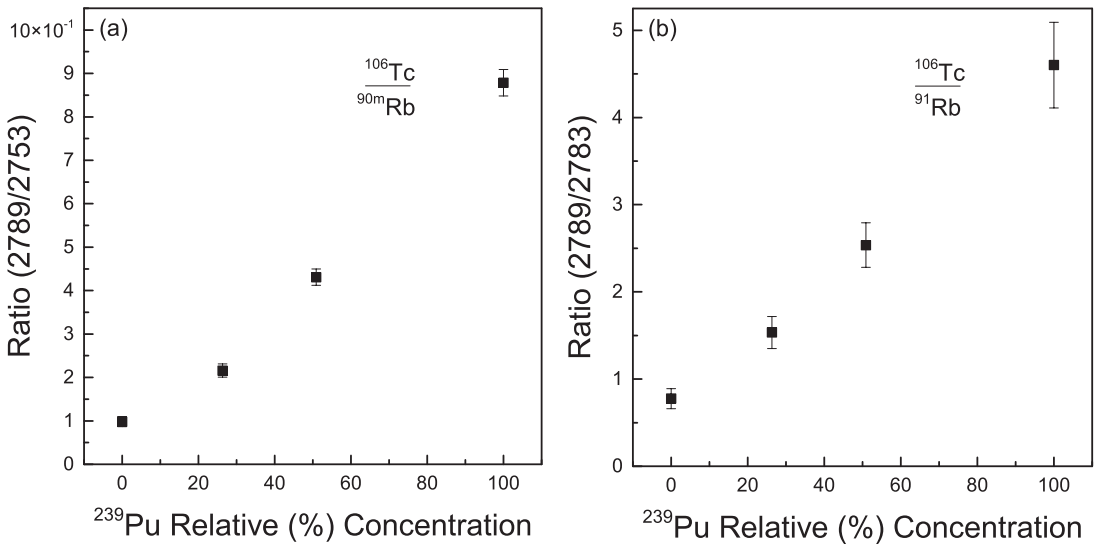

Figure 4.20: Results of peak ratio analysis performed on the cluster of photopeaks from Figure 4.19 utilizing linked multi-Gaussian fitting to deconvolve the cluster of three overlapping photopeaks. The ratio of the 2789 keV photopeak from ^{106}Tc was taken with the solitary 2753 keV photopeak from ^{90m}Rb (a) and the obscured 2783 keV photopeak from ^{91}Rb (b).

with a relatively small error, ∼7% of the value on average. Because the fitting algorithm is capable of discerning the ^{91}Rb photopeak, the area of such can also be utilized for analysis. Figure 4.20.b shows the ratio between the 2789 keV from ^{106}Tc and the 2783 keVfrom ^{91}Rb. Because the photopeak is buried within a cluster and the area of the 2783 keV peak is small, this contributes to an increased error of roughly 10-15%. Despite their close proximity and this increase in error, the ratio between the 2789 keV and the 2783 keV shows a strong monotonic relationship that can be utilized to discern relative ^{239}Pu concentration in a mixed ^{239}Pu/^{235}Usample.

4.3 Spectral Contribution Analysis

Spectral contribution analysis has shown significant promise for use in isotopic identification [28, 29]. Rather than focusing on a few photopeaks, SCA utilizes a wide energy range containing many photopeaks to reduce the statistical error. SCA eliminates the need to fit individual photopeaks as well as the need for deconvolution

of overlapping peaks. An energy spectrum of a mixed sample is assumed to be a linear combination of the spectra of its individual components. Using the equation,

$$\phi_{comb.} = \alpha_{239} \cdot \phi_{239} + \alpha_{235} \cdot \phi_{235}, \tag{4.1}$$

a portion of the ^{235}U (ϕ_{235}) and ^{239}Pu (ϕ_{239}) energy spectra can be used to recreate the spectrum of a combined target, $\phi_{comb.}$. The coefficients, α's, can be determined with a simple least squares regression fitting routine. These coefficients can then be used to determine the relative concentration of a given mixed sample. Without the need to deconvolve multiple photopeaks, the number of free parameters in the fitting algorithm decreases to the mere number of contributing fissile materials, a significant advantage over PRA. SCA does, however, require the delayed γ-ray spectra of each component acquired under identical experimental parameters. To acomplish this, both modeled spectra and collected spectra can be used to form the basis set. However, for this research, the collected energy spectra of samples containing only ^{239}Pu and ^{235}U were used to form the basis set.

In selection of the energy range for analysis, it was decided to balance the maximization of spectrum structure while minimizing the possibility of background. To do this, the region starts from 2650 keV, well above natural background, and terminates at 3750 keV, just above where spectral characteristics diminish significantly. Figure 4.21 shows the results of SCA on the four targets in the 90 s/90 s irradiation scheme along with the resulting fitted energy spectrum of the two combined targets. Because the basis set fully fits itself, this leaves only the two data points from the combined targets for analysis. The figure shows that, while there is some over projection of a few photopeaks in the 26.3% ^{239}Pu target, the basis set is very capable of recreating the mixed targets with very little variation from the measured spectra.

Figure 4.22 shows the relative ^{239}Pu spectral contribution of the targets determined using spectral contribution analysis. There is significantly small associated statistical error, $\sim$1% relative concentration versus $\sim$3% for PRA. This reduction in statistical error is due to the large number of counts contributing to the analysis. The two pure targets fall exactly on the line of equality because they are the basis of the

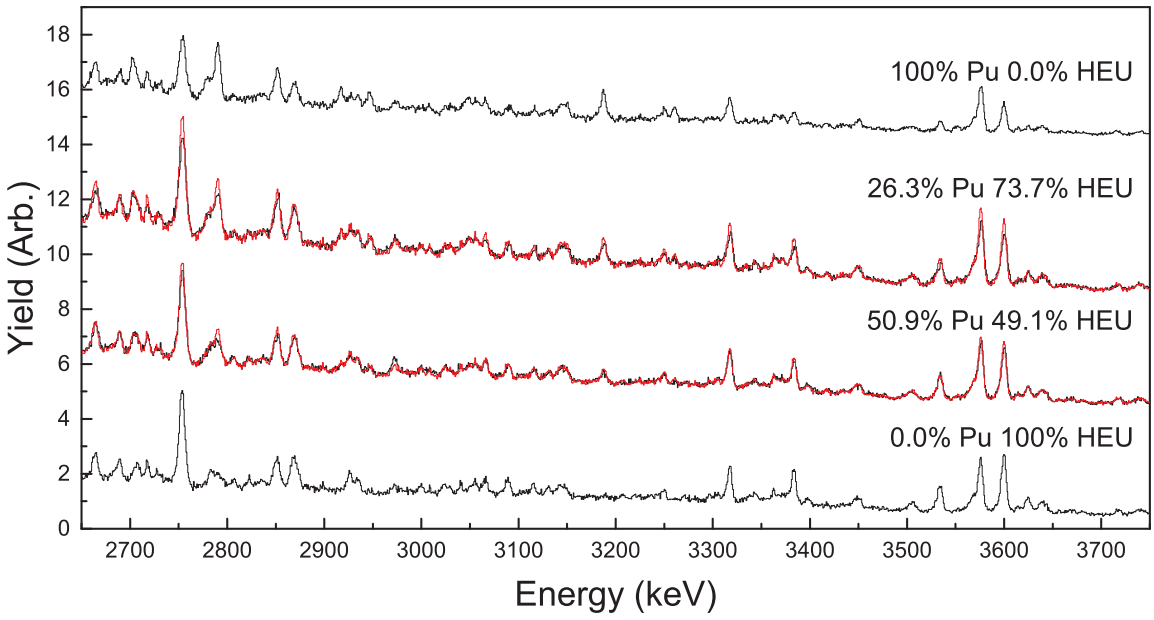

Figure 4.21: The portion of the energy spectra used for spectral contribution analysis. The 100% ^{239}Pu and 0% ^{239}Pu spectra were used as a basis set for recreation of the two mixed targets. Original data is shown in black while the fit to bicomponent spectra are shown in red. Artificial offsets have been introduced to allow differentiation of the spectra and their characteristics.

fitting algorithm. The mixed targets, however, deviate by as much as 10% from their expected value. Compared to PRA, which was within 1σ standard deviation of the actual value, this is a significant disadvantage. Equating the terms in Equation 4.1 with those of Equation 2.11 and introducing the masses of each isotope used in the construction of the basis set, 2.9 g of ^{239}Pu and 2.8 g of ^{235}U, yields,

$$\begin{aligned} \phi_{comb.} &= \alpha_{239} \cdot \phi_{239} + \alpha_{235} \cdot \phi_{235} \\ &= \frac{dY_{Reg.}}{dm_{Pu}} \cdot m_{Pu} + \frac{dY_{Reg.}}{dm_U} \cdot m_U \\ &= \frac{dY_{Reg.}}{dm_{Pu}} \cdot 2.9\ g \times \alpha_{239} + \frac{dY_{Reg.}}{dm_U} \cdot 2.8\ g \times \alpha_{235}, \end{aligned} \tag{4.2}$$

where the coefficients, α's vary from zero to one. The masses of the relative concen-

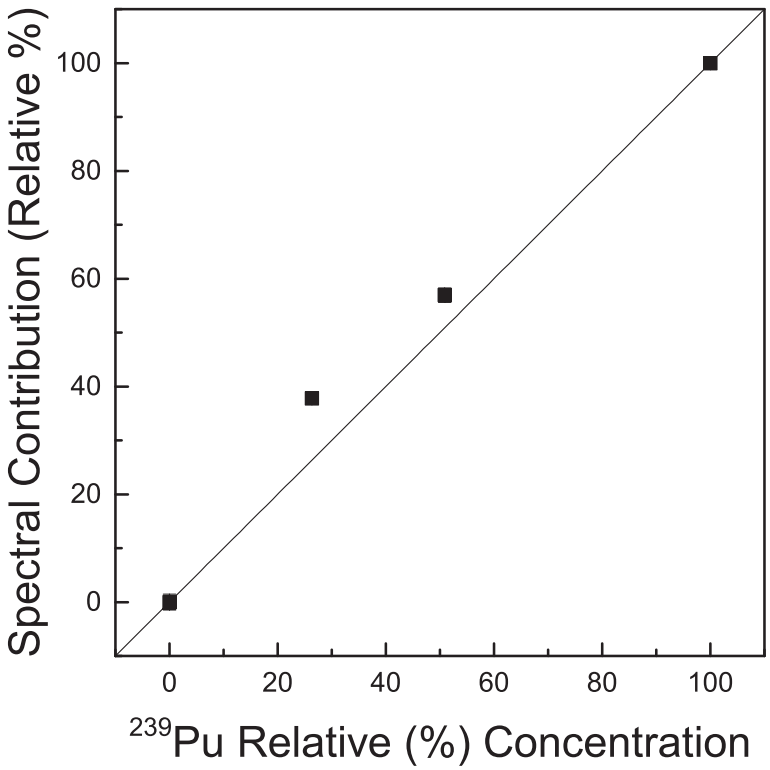

Figure 4.22: Spectral contribution analysis performed with a region of energy from 2650 keV to 3750 keV from the 90 s/90 s data set. This method utilizes the pure ^{239}Pu and ^{235}U spectra as the basis set and fits the spectra of two mixed targets. Error bars are representative of 1σ standard deviation. The line represents equality between relative ^{239}Pu concentration and relative ^{239}Pu spectral contribution.

tration can thus be represented by,

$$\frac{m_{Pu}}{m_{Pu} + m_U} = \frac{2.9\ g \cdot \alpha_{239}}{2.9\ g \cdot \alpha_{239} + 2.8\ g \cdot \alpha_{235}}. \tag{4.3}$$

Since relative spectral contribution is expected to track with relative concentration, both the mixed targets are over predicted in their relative ^{239}Pu concentrations.

The expected SCA coefficients can easily be calculated from the masses of ^{239}Pu and ^{235}U in the target. Figure 4.23 shows the measured SCA coefficients from the fitting algorithm for ^{239}Pu and ^{235}U along with their expected values. Figure 4.23.a shows that the ^{239}Pu coefficient remains relatively close to the predicted values, how-

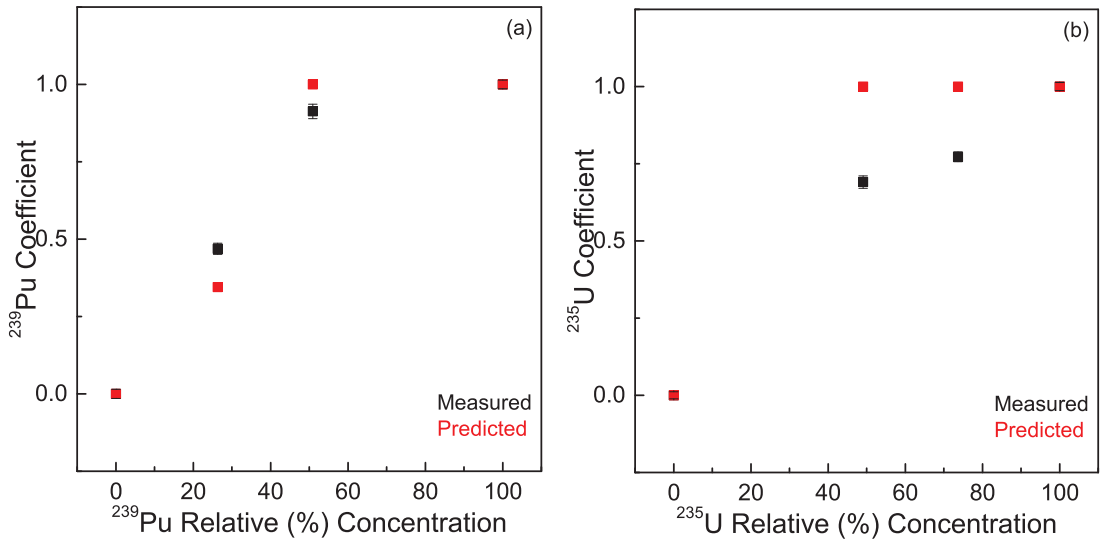

Figure 4.23: The ^{239}Pu coefficient (a) and ^{235}U coefficient (b) from spectral contribution analysis utilizing the energy region spanning 2650 keV to 3750 keV. Error bars are representative of 1σ standard deviation. The measured coefficients are shown in black with the predicted coefficients shown in red.

ever, Figure 4.23.b shows that the ^{235}U coefficient is significantly below the expected values for both composite targets. This is likely due to mass effects in the targets which cause attenuation of the γ-rays exiting the target and consumption of neutrons available for fission within the combined targets. These effects either reduce the total number of delayed γ-rays making it to the HPGe detector, in the case of attenuation, or reduce the total number of γ-rays emitted by the target material, in the case of neutron consumption. These effects reduce the capability of the SCA algorithm to accurately link the spectral contribution to the mass. In this instance the total measured spectra for these two targets are 7.5% and 19.8% smaller than expected for the 26.3% and 50.9% relative ^{239}Pu targets, respectively. While the contribution of the ^{239}Pu spectrum is over predicted in one target, the total still falls shy of the expected complete spectrum. SCA assumes that the total varies linearly with respect to mass. While this may be true for low-mass and homogeneous targets, SCA cannot accurately portray the target composition when γ-ray attenuation or complete neutron consumption play a role.

4.3.1 Peak Areas

The same contribution analysis can be applied to an array of peak areas. In much the same way two spectra merge to form a combined spectrum, so too would the individual peak areas. By combining multiple peak areas into a vector, the statistical error can be reduced over that of individual peaks. A vector of peak areas created by ^{239}Pu and ^{235}U can then be used to determine the relative concentration of a mixed sample in very much the same way as with spectral contribution analysis. By changing Equation 4.1 to vectors of peak areas instead of spectra, an array of photopeak areas of a combined target can be assumed to be a linear combination of its constituent arrays. Equation 4.1 thus becomes,

$$\boldsymbol{a_{comb.}} = \alpha_{239} \cdot \boldsymbol{a}_{239} + \alpha_{235} \cdot \boldsymbol{a}_{235}, \tag{4.4}$$

where the $\boldsymbol{a}$'s are now vectors of peak areas.

Figure 4.24 shows the results of SCA performed using a vector of peak areas. The peaks from Table 4.2 were used to form an array of peak areas and fed through the same least squares regression algorithm as was used for SCA on sections of whole spectra. The statistical error is increased over that of SCA utilizing spectra, from an average of ∼1.2% to ∼2% relative concentration. This increase in the statistical error is due to the reduction in counts used to form the basis and mixed vectors. Despite this increase in statistical error, the accuracy of using an array of peak areas is significantly increased over that of using a range of spectra. The point at 26.3% relative ^{239}Pu concentration is within error bars of the line of equality. While the data point at 50.9% relative concentration is not on this line, it is within 5%. Utilizing entire spectra for SCA resulted in differences from this line in excess of 10%. The increase in accuracy is most likely due to the reduced influence of the continuum. Figure 4.25 shows the resulting spectra reproduced from the fitting algorithm along with the original spectra. In the figure it can be seen that the peak areas appear to be accurately portrayed while the continuum is undercalculated. The continuum between photopeaks is in excess of the counts present in the individual photopeaks

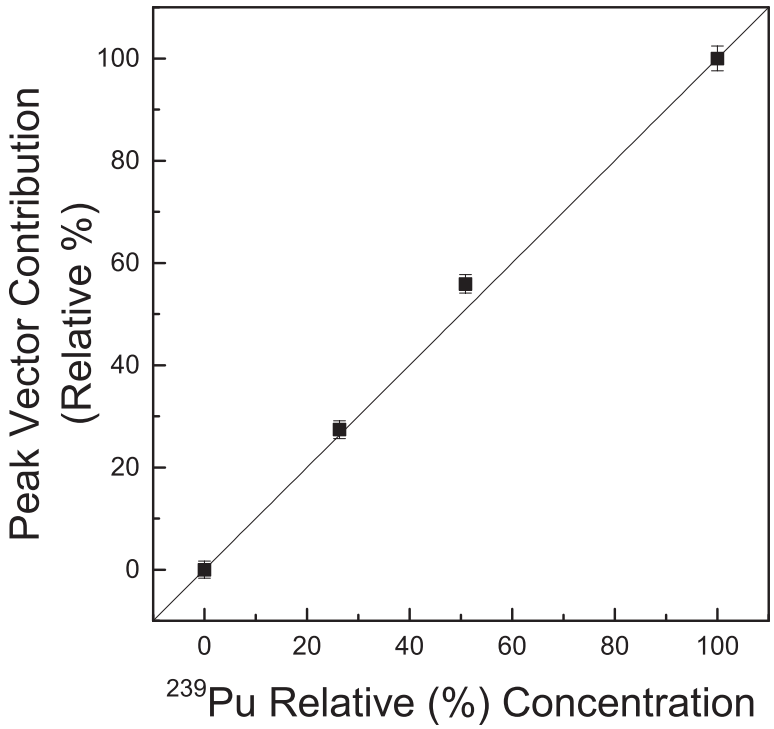

Figure 4.24: Spectral contribution analysis performed on an array of peak areas rather than a continuum of spectra. The peaks areas used in PRA (Table 4.2) were aligned into an array. The arrays of pure samples were then used as a basis set to fit the arrays of mixed samples using least squares regression. Error bars are representative of 1σ standard deviation.

themselves providing significant influence over the fitting algorithm. An array of peak areas is removed from this influence, thus increasing accuracy.

4.4 Mass Effects

The delayed γ-ray yield has been assumed to be linear with respect to mass. This assumption works for a variety of targets and experimental setups where the density of the target is low and the intensity of the interrogating source is significant as to penetrate the target easily. With this assumption as mass increases, so should the emissions from that mass. However, further analysis shows that this is not the case.

Figure 4.26 shows a diagram of neutrons entering a mixed target containing ^{239}Pu

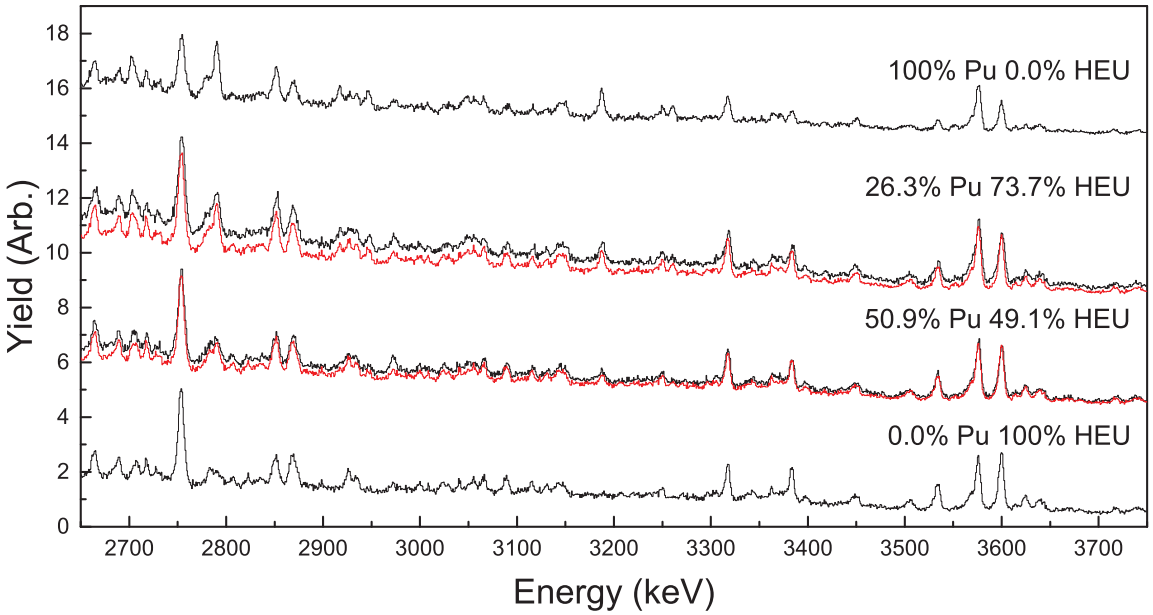

Figure 4.25: The portion of the energy spectra used for spectral contribution analysis. Peak areas derived from the 100% ^{239}Pu and 0% ^{239}Pu spectra were used to form a basis vector for recreation of vectors containing identical peak areas the two mixed targets. Original data is shown in black while a fit to bicomponent spectra are shown in red using the coefficients obtained from the algorithm. Artificial offsets have been introduced to allow differentiation of the spectra and their characteristics.

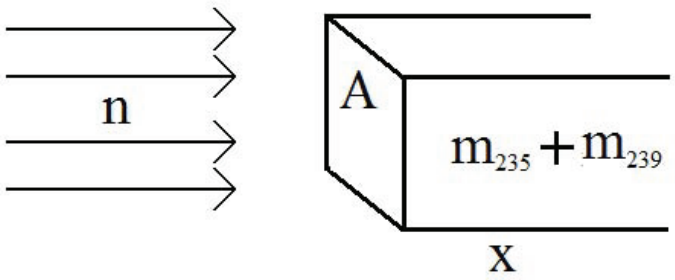

Figure 4.26: Simplified diagram of neutrons entering a target containing a mixture of ^{239}Pu and ^{235}U with a surface area of A and a thickness of x.

and ^{235}U. The equation,

$$\frac{dn}{dx} = -\beta_{235}n - \beta_{239}n - \beta_o n = \beta_{tot.}n, \tag{4.5}$$

governs the number of neutrons, n, as a function of depth into a target, where the β's are the absorption rate caused by fission and β_o is is the absorption from all other processes and those neutrons that escape the target. The solution to this equation is,

$$n = n_0 e^{-\beta_{tot.} x}, \tag{4.6}$$

where x is the depth into the target. The fission yield per unit depth for a target containing both ^{235}U and ^{239}Pu is thus,

$$\frac{dY_f}{dx} = \sigma_{235} N_{235} n_0 e^{-\beta_{tot.} x} + \sigma_{239} N_{239} n_0 e^{-\beta_{tot.} x}, \tag{4.7}$$

where σ_f is the fission cross section, N is the atomic density of the target and n_0 is the initial number of neutrons entering the surface of the target. By integrating Equation 4.7 from the surface of the target to its thickness, x_t, the yield from fission is,

$$Y_f = \frac{\sigma_{235} N_{235} n_0}{\beta_{tot.}}(1 - e^{-\beta_{tot.} x_t}) + \frac{\sigma_{239} N_{239} n_0}{\beta_{tot.}}(1 - e^{-\beta_{tot.} x_t}). \tag{4.8}$$

The total density ($\rho_{tot.}$) of the target can be represented by,

$$\rho_{tot.} = \rho_{235} + \rho_{239} = \frac{m_U}{x_t A} + \frac{m_{Pu}}{x_t A}. \tag{4.9}$$

Substituting for x_t provides the yield from fission as a function of mass and number of neutrons,

$$Y_f = \frac{\sigma_{235} N_{235} n_0}{\beta_{tot.}}(1 - e^{-\frac{\beta_t}{\rho_{tot.} A}(m_U + m_{Pu})}) + \frac{\sigma_{239} N_{239} n_0}{\beta_{tot.}}(1 - e^{-\frac{\beta_{tot.}}{\rho_{tot.} A}(m_U + m_{Pu})}). \tag{4.10}$$

The atomic density of ^{235}U can be represented by,

$$N_{235} = \frac{m_U N_A}{M_{235} A x_t} = \frac{m_U N_A \rho_{tot.}}{M_{235}(m_U + m_{Pu})}, \tag{4.11}$$

where M_{235} is the molar mass of ^{235}U. Substituting the atomic densities for ^{235}U and

^{239}Pu into Equation 4.10 yields the equation,

$$\begin{aligned} Y_f =& \frac{\sigma_{235} m_U n_0 N_A \rho_{tot.}}{M_{235} \beta_{tot.} (m_U + m_{Pu})} (1 - e^{-\frac{\beta_{tot.}}{\rho_{tot.} A}(m_U + m_{Pu})}) \\ &+ \frac{\sigma_{239} m_{Pu} n_0 N_A \rho_{tot.}}{M_{239} \beta_{tot.} (m_U + m_{Pu})} (1 - e^{-\frac{\beta_{tot.}}{\rho_{tot.} A}(m_U + m_{Pu})}). \end{aligned} \tag{4.12}$$

Expanding the exponentials in Equation 4.12 in the low mass limit yields,

$$\begin{aligned} Y_f =& \frac{\sigma_{235} m_U n_0 N_A \rho_{tot.}}{M_{235} \beta_{tot.} (m_U + m_{Pu})} (1 - 1 + \frac{\beta_{tot.}}{\rho_{tot.} A}(m_U + m_{Pu}) + \ldots) \\ &+ \frac{\sigma_{239} m_{Pu} n_0 N_A \rho_{tot.}}{M_{239} \beta_{tot.} (m_U + m_{Pu})} (1 - 1 + \frac{\beta_{tot.}}{\rho_{tot.} A}(m_U + m_{Pu}) + \ldots), \end{aligned} \tag{4.13}$$

and,

$$Y_f = \frac{\sigma_{235} n_0 N_A}{M_{235} A} \cdot m_U + \frac{\sigma_{239} n_0 N_A}{M_{239} A} \cdot m_{Pu} = \frac{dY}{dm_U} \cdot m_U + \frac{dY}{dm_{Pu}} \cdot m_{Pu}. \tag{4.14}$$

Thus, the delayed γ-ray yield has been assumed to be linear with respect to mass. For small mass targets the equation,

$$\frac{dY_{H.E.}}{dm_{tot.}} = \frac{\frac{dY_{H.E.}}{dm_{Pu}} \cdot m_{Pu} + \frac{dY_{H.E.}}{dm_U} \cdot m_U}{m_U + m_{Pu}}, \tag{4.15}$$

governs the total high-energy yield, $Y_{H.E.}$, as a function of the contributing masses; in this instance, the masses of ^{235}U (m_U) and ^{239}Pu (m_{Pu}). Substituting the relative ^{239}Pu concentration into Equation 4.15 yields,

$$\frac{dY_{H.E.}}{dm_{tot.}} = (\frac{dY_{H.E.}}{dm_{Pu}} - \frac{dY_{H.E.}}{dm_U}) \cdot R_{Pu} + \frac{dY_{H.E.}}{dm_U}. \tag{4.16}$$

Equation 4.16 shows that the high-energy yield should be linear with respect to relative concentration. At a relative concentration of zero, the yield is just that of ^{235}U. As the concentration of ^{239}Pu is increased to 100% the yield is simply that of ^{239}Pu. Figure 4.27 shows the yield of high-energy γ-rays from the four targets as a function of relative concentration. This yield has been shown in previous experiments conducted using bremsstrahlung photons as an interrogating source to be a direct

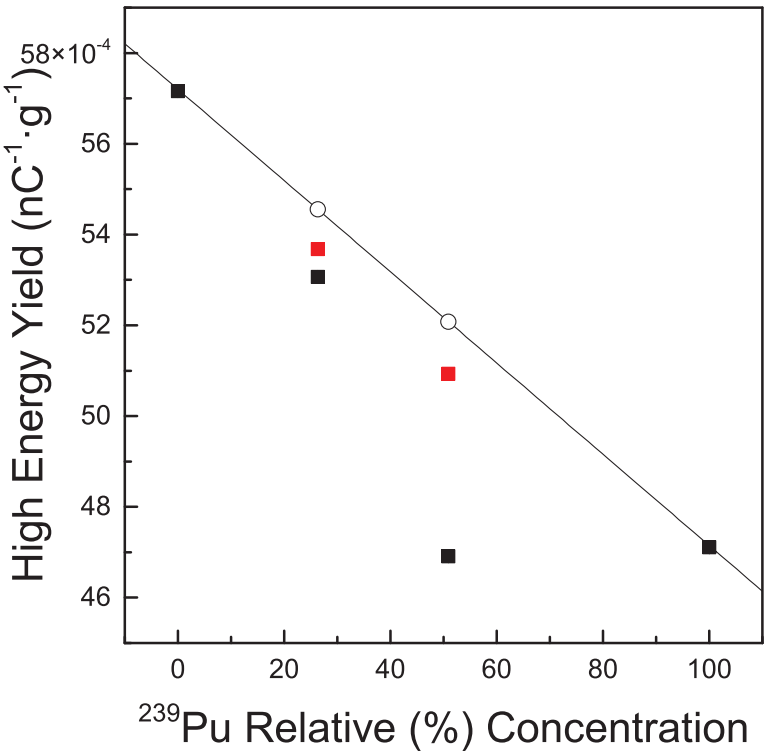

Figure 4.27: Delayed γ-ray yield above 3 MeV across the four targets as a function of relative concentration (■). The line indicates the expected linear relationship between relative concentration and the high energy yield from Equation 4.16 with the expected positions of the 26.3% and 50.9% relative ^{239}Pu targets (○). Also shown is the calculated delayed γ-ray yield utilizing attenuation of the ^{235}U γ-rays through the ^{239}Pu NADs (■).

indication of fissionable material in congruence with Equation 4.16 [10, 28]. Included in this graph is the expected yield line dictated by Equation 4.16 and the expected positions of the 26.3% and 50.9% relative concentration yields. Unfortunately, the measured high-energy delayed γ-ray yields for these two data points fall short of their expected low-mass values.

In an effort to determine the factors causing the decreased yields at 26.3% and 50.9% relative concentration, an estimation of the attenuation of high-energy γ-rays within the targets was calculated. The samples are formed by placing the ^{235}U pellets behind the ^{239}Pu disks as discussed in Section 3.2. A fraction of the ^{235}U is shadowed

from the HPGe detector. This causes some of the γ-rays exiting the ^{235}U pellets to pass through the ^{239}Pu NADs. Using the target geometry, it was calculated that approximately 20% and 40% of the ^{235}U in the 26.3% and 50.9% relative ^{239}Pu targets are shadowed by the ^{239}Pu, respectively. The measured values for $dY_{H.E.}/dm_{Pu}$ and $dY_{H.E.}/dm_{U}$ along with the fraction of attenuated γ-rays was used in Equation 4.16 to calculate the expected high-energy yield for the mixed targets. Attenuation was calculated with the assumption that all γ-rays that are attenuated or scattered do not make it to the detector. This assumption can only under predict the high-energy delayed γ-ray yield. The results of this calculation were then added to Figure 4.27.

Even over predicting the quantity of attenuation that is occurring, attenuation can only account for a fraction of the difference between the predicted and measured high-energy delayed γ-ray yields. The remainder of this difference must come from lack of neutron excess (total neutron consumption) or self-shielding of the neutrons. If the number of neutrons is limited, as mass is increased the amount of fission, and thus delayed γ-rays, decreases per gram of fissile material. This is due simply to all of the neutrons in the experimental setup being consumed, for fission or otherwise. While more material becomes available for fission, the neutrons remain limited, restricting the quantity of fission to that of the number of available neutrons for it. It is also possible that as the mass is increased in the target the amount of self-shielding is increased, reducing the amount of neutrons that are available for fission per gram of fissile material. While attenuation, self-shielding and total consumption of neutrons plays a significant role in discerning mass through spectral contribution analysis, it does not have a significant influence in the peak ratio analysis data.

Figure 4.28 shows the measured dY/dm of the 3186 keV line from ^{106}Tc from ^{239}Pu as a function of total fissile mass. This peak is only present in samples containing ^{239}Pu and is indicative of its fission. As shown in the figure, dY/dm is not a constant as expected and is influenced by the total fissile mass in the sample. While the dY/dm value at 2.9 and 3.8 g are within error bars, the point at 5.7 g is reduced to $\sim$70% of these values. It is evident that the increased mass decreases the number of neutrons available for fission per gram of fissile material thus reducing the apparent dY/dm and making the yield nonlinear with respect to mass.

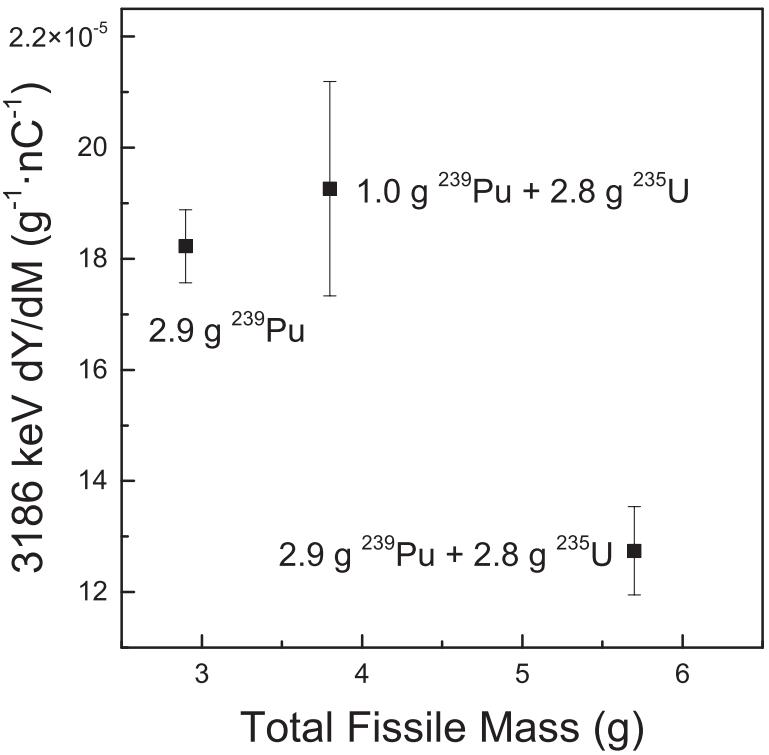

Figure 4.28: Measured dY/dm of the 3186 keV line from ^{106}Tc from ^{239}Pu as a function of total fissile mass. Error bars are indicative of 1σ standard deviation.

Equation 4.12 can be separated into its linear function and a nonlinear function by,

$$\begin{aligned} Y_f =& \frac{\sigma_{235} n_0 N_A}{M_U A} \times m_U \times \frac{\rho_{tot.} A}{\beta_{tot.}(m_U + m_{Pu})}(1 - e^{-\frac{\beta_{tot.}}{\rho_{tot.} A}(m_U + m_{Pu})}) \\ &+ \frac{\sigma_{239} n_0 N_A}{M_{Pu} A} \times m_{Pu} \times \frac{\rho_{tot.} A}{\beta_{tot.}(m_U + m_{Pu})}(1 - e^{-\frac{\beta_{tot.}}{\rho_{tot.} A}(m_U + m_{Pu})}) \\ &= \frac{dY_f}{dm_U} \cdot m_U \times f(m_{tot.}) + \frac{dY_f}{dm_{Pu}} \cdot m_{Pu} \times f(m_{tot.}). \end{aligned} \tag{4.17}$$

The function, f, is dependent upon the total fissile mass of the target and is equal to,

$$f(m_{tot.}) = f(m_U + m_{Pu}) = \frac{\rho_{tot.} A}{\beta_{tot.}(m_U + m_{Pu})}(1 - e^{-\frac{\beta_{tot.}}{\rho_{tot.} A}(m_U + m_{Pu})}). \tag{4.18}$$

In the low mass limit Equation 4.18 is equal to one. In the high mass limit the total fission yield becomes,

$$\begin{aligned} Y_f =& \frac{\sigma_{235} n_0 N_A}{M_U A} m_U \frac{\rho_{tot.} A}{\beta_{tot.}(m_U + m_{Pu})} + \frac{\sigma_{239} n_0 N_A}{M_{Pu} A} m_{Pu} \frac{\rho_{tot.} A}{\beta_{tot.}(m_U + m_{Pu})} \\ =& \frac{dY_f}{dm_U} \cdot \frac{m_U}{m_U + m_{Pu}} \cdot \frac{\rho_{tot.} A}{\beta_{tot.}} + \frac{dY_f}{dm_{Pu}} \cdot \frac{m_{Pu}}{m_U + m_{Pu}} \cdot \frac{\rho_{tot.} A}{\beta_{tot.}}, \end{aligned} \tag{4.19}$$

where the value $\rho_{tot.} A / \beta_{tot.}$ is the total fissile mass capable of interaction, m_i. Figure 4.29 shows the expected behavior of the yield as a function of an arbitrary mass. At low energies, the yield is linear with fissile mass. As the mass is increased, the yield reaches a maximum limit. This limit is determined by the neutrons made available for fission, target density and total fissile mass. These parameters dictate the depth to which the neutrons can penetrate the material and, subsequently, the total interacting fissile mass, m_i.

The maximum half-depth of neutron penetration for the targets can be calculated from the lowest interacting fissile material, in this instance ^{235}U. The cross section at peak neutron energy for ^{235}U is $\sim$78% that of ^{239}Pu. This, along with the reduced fissile density from the level of enrichment, makes ^{235}U the least interacting material in the targets. The half-depth is determined by,

$$d_{\frac{1}{2}} = \frac{ln(2)}{\sigma_{235} \cdot \eta_{235}}, \tag{4.20}$$

where η_{235} is the atomic density of the ^{235}U target and σ_{235} is assumed to be the fission cross section at peak neutron energy. Inserting the values for enriched ^{235}U target into Equation 4.20, the maximum half-depth for neutrons in the target is $\sim$1.45 mm. While the targets selected in this experiment are small, the smallest dimension of the ^{235}U cylinders is 4.88 mm in diameter, making the maximum interacting mass, m_i, significantly smaller than that of the targets.

For results relying on relative concentration like PRA and SCA the mass effects

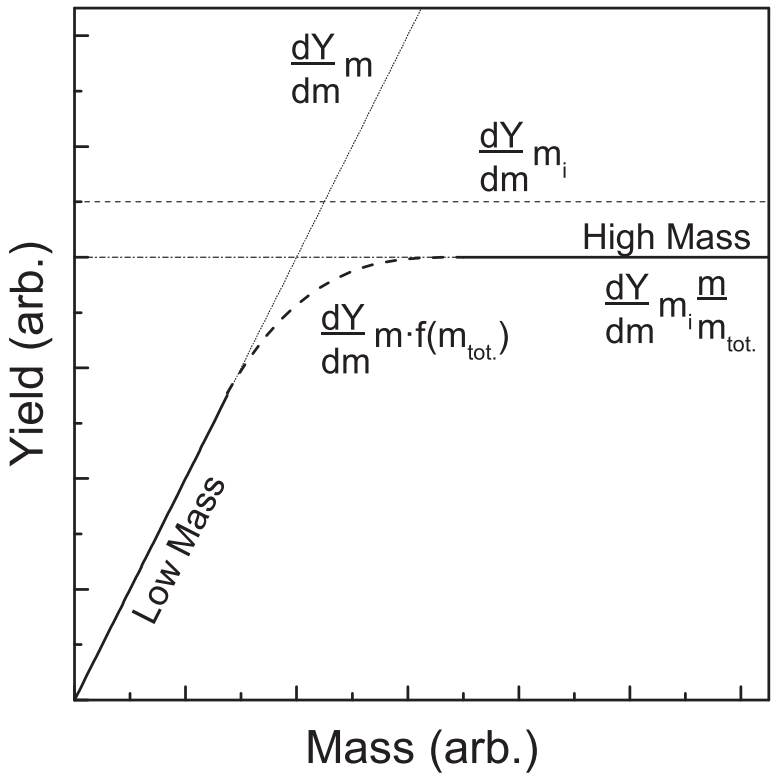

Figure 4.29: The expected shape of yield as a function of mass. At low-mass the yield is expected to be linear with dY/dm. At high-mass, additional mass will not increase the yield.

are negligible. For the peak ratio equation,

$$Y_1 : Y_2 = \frac{\frac{dY_1}{dm_{Pu}} \cdot m_{Pu} \cdot f(m_{tot.}) + \frac{dY_1}{dm_U} \cdot m_U \cdot f(m_{tot.})}{\frac{dY_2}{dm_{Pu}} \cdot m_{Pu} \cdot f(m_{tot.}) + \frac{dY_2}{dm_U} \cdot m_U \cdot f(m_{tot.})}, \tag{4.21}$$

it can clearly be seen that the function $f(m_{tot.})$ would cancel out. The same can also be seen in instances regarding relative concentrations. However, for instances relying on total yield, f does not cancel out. This limits the ability of SCA to determine exact mass as seen in Figure 4.23, however, it should not limit its ability to determine relative mass concentration from relative spectral contribution. Equation 2.10 dictates the spectral contribution. Substituting the experimental parameters for SCA

into the ^{239}Pu component of Equation 2.10 yields,

$$\alpha_{239} \cdot \phi_{239} = \frac{m_{Pu} \cdot f(m_{tot.})}{m^b_{Pu} \cdot f(m^b_{Pu})} \cdot \frac{dY_1}{dm_{Pu}} \cdot m^b_{Pu} \cdot f(m^b_{Pu}), \tag{4.22}$$

where m^b_{Pu} signifies the mass used to create the basis spectrum for ^{239}Pu. By taking the relative ^{239}Pu spectral contribution,

$$\frac{\alpha_{239}}{\alpha_{239} + \alpha_{235}} = \frac{\frac{m_{Pu} \cdot f(m_{tot.})}{m^b_{Pu} \cdot f(m^b_{Pu})}}{\frac{m_{Pu} \cdot f(m_{tot.})}{m^b_{Pu} \cdot f(m^b_{Pu})} + \frac{m_U \cdot f(m_{tot.})}{m^b_U \cdot f(m^b_U)}} = \frac{m_{Pu}}{m_{Pu} + \frac{m^b_{Pu} \cdot f(m^b_{Pu})}{m^b_U \cdot f(m^b_U)} \cdot m_U}, \tag{4.23}$$

the influence of the mass effects in relative spectral contribution can be seen. Because the spectra comprising the basis sets are formed using nearly identical masses, 2.8 g ^{238}U and 2.9 g ^{239}Pu, the factor,

$$\frac{m^b_{Pu} \cdot f(m^b_{Pu})}{m^b_U \cdot f(m^b_U)}, \tag{4.24}$$

is very close to one. This minimizes the influence of mass effects on spectral contribution analysis and results in a linear relationship between relative concentration and relative spectral contribution. In the instances that these mass effects take hold, these methods cannot be used to determine exact mass of a target. These methods can, however, be used to determine relative concentration.

4.5 Principal Component Analysis

Principal component analysis is designed to determine the direction of greatest variance in a data set [31,32]. In data such as this, that direction may correlate to the total mass of the target, the mass of an individual constituent, a relative concentration or some combination thereof. Methods like PCA are often tied to a least squares regression algorithm to relate the results of the analysis to a known observable [32]. In the case of spectroscopy on gasoline samples, the calculated principal component loadings would be correlated with an observable such as octane [41]. This method,

however, requires a substantially larger data set than the spectra of four targets. A large data set of known samples is used to "train" the multivariate analysis to the known observable. Once trained, the analysis can be applied to unknown samples and used to determine their composition, octane, tensile strength, etc., depending on the desired output.

Because of the limitations of the data set and the fact that there are multiple observables such as mass and relative concentration, it is beneficial to perform PCA without forcing a correlation to a known parameter. The correlations between the input spectra and the new transformed spectra, or loadings, of each component can be compared to known parameters in an attempt to find a correlation between that principal component and that parameter. These loadings are the degree of transformation from the old coordinate system to a new, minimally correlated, system. The resulting transformed spectra, or scores, tied to those loadings can then be utilized to pinpoint peaks that dominate that correlation. These scores are linear combinations of the existing spectra that inherit the maximum variance from the spectra. Large scores indicate that that portion of the spectra, often a peak, is largely described by that principal component. Unfortunately, a single component may not describe a large portion of the variance in a sample and often two or more are necessary to fully describe the data [32, 42]. Also, because principal component analysis makes no assumptions about the data, a correlation between a component and a single observable may not be possible [32].

4.5.1 PCA on Sections of Spectra

While it is common to utilize entire spectra, the portion of the energy spectrum from 2650 keV to 3750 keV from the 90 s/90 s irradiation scheme was selected as data input for PCA. This portion is identical to that used in Section 4.3 and was selected for its elevated energy, above that of natural decay, along with its high degree of structure. Because many of the observable fission fragments have photopeaks in this region, it is highly representative of the ^{239}Pu and ^{235}U delayed γ-ray spectrum. Figure 4.30.a shows a log plot of the variance described by each of the four principal components.

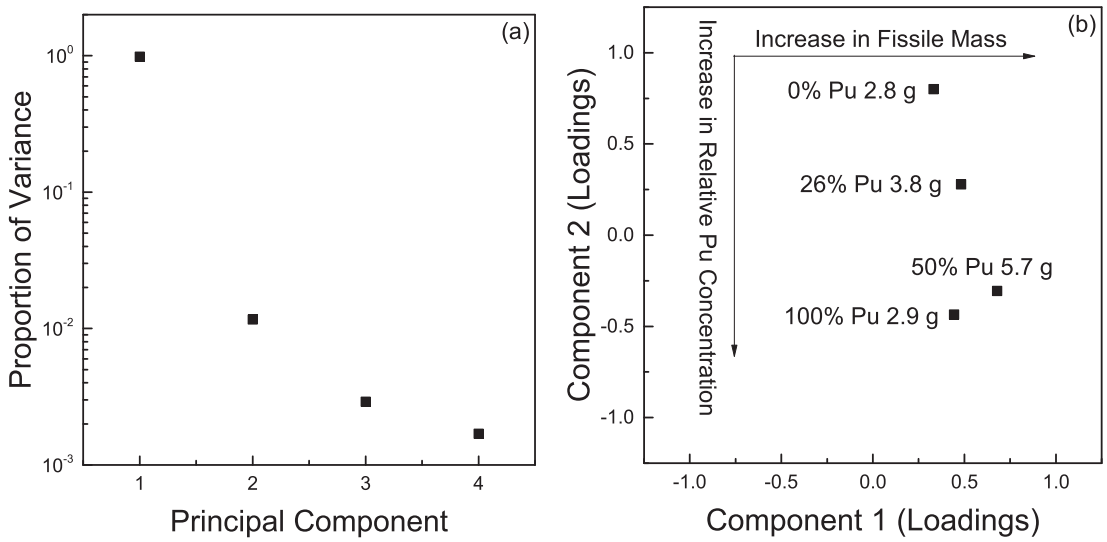

Figure 4.30: Some of the results of principal component analysis performed using a section of the energy spectrum from 2650 keV to 3750 keV from the 90 s/90 s data set. (a) Scree plot showing the proportion of variance each principal component describes and (b) a loadings plot between the first and second components. The loading plot also shows the relative ^{239}Pu concentration along with the total fissile mass in the sample along with possible directions of correlation between individual components and their likely observables.

This scree plot shows that the first component alone accounts for 98.4% of the variance in the spectra. This first component is two orders of magnitude larger than the next greatest contributor. A total of 99.5% of the data's variance is described by the first two components alone. With the remainder of the components accounting for only 0.5% of the variance in the data, it is likely that they are unnecessary and that the data can be described in full by the first two components alone. Despite this assumption, correlations between all possible observables and all principal components was sought.

Figure 4.30.b shows the loadings plot between the first two components. As indicated by the scree plot these components describe 99.5% of the variance in the spectra. In an ideal situation each component would correspond to an known observable. Correlations between the first two components and the individual masses of ^{239}Pu, ^{235}U, total fissile mass and relative concentration were sought. In Figure 4.30.b the loadings are labeled with their respective target's relative ^{239}Pu concentration along

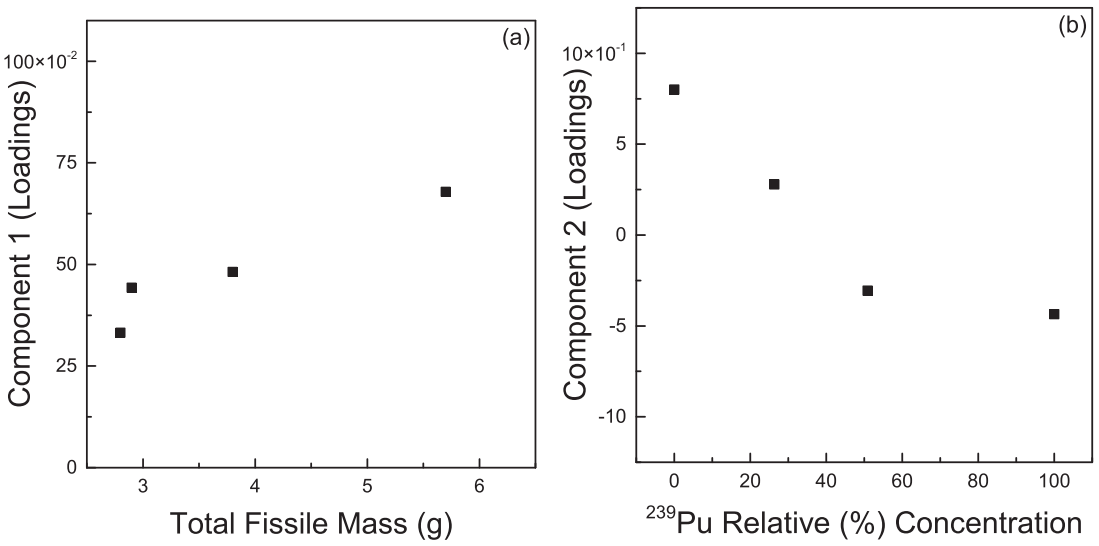

Figure 4.31: Principal component loadings as functions of likely primary correlation. (a) The first component as a function of total fissile mass in the target. (b) The second principal component as a function of relative concentration.

with their respective total fissile mass. The first component's loadings appear to vary primarily with total fissile mass while the second component varies primarily with relative concentration. A linear fit may be applied to each component separately to obtain both total fissile mass and relative concentration. It is desirable to constrain the fit order to linear to find an optimal relation between one or more components and an observable. The coefficient of determination, R^2 value, obtained with a linear fit describes a great deal of the correlation between the loadings and the observable and, with only four data points, increasing the order can cause false correlations.

Figure 4.31 shows the first two component loadings with respect to their apparent correlations. Figure 4.31.a shows that the first component does indeed vary monotonically with the total fissile mass in the sample. A strong linear relationship could be drawn between the first component loadings and total fissile mass. While there are deviations from linearity, this is possibly due to incomplete separation of the component and multiple observables or merely statistical variations in the data. Figure 4.31.b compares the second principal component loadings with relative concentration. There is also strong monotonic relationship between component 2 and relative concentra-

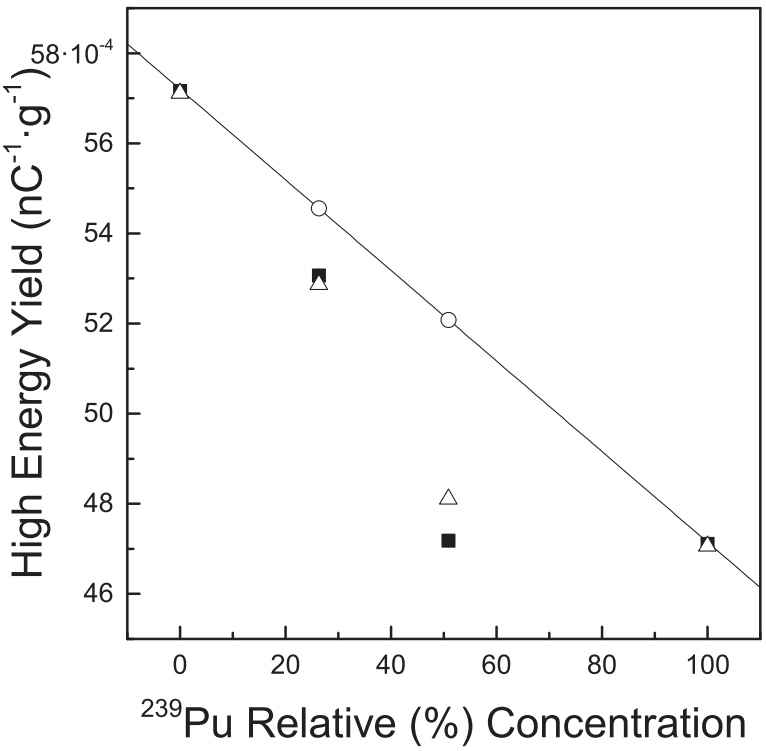

Figure 4.32: Delayed γ-ray yield above 3 MeV across the four targets as a function of relative concentration (■). The line indicates the expected linear relationship between relative concentration and the high energy yield from Equation 4.16 with the expected positions of the 26.3% and 50.9% relative ^{239}Pu targets (○). The second PCA component loadings (△) have been scaled with high energy delayed γ-ray yield to match at 0.0% and 100% relative ^{239}Pu concentration.

tion. A linear correlation can be drawn between this component and relative ^{239}Pu concentration. Because the mass of a sample cannot always be controlled, relative concentration is a significantly important observable, however, this component appears to deviate from linearity greater than that of the first. In examining Figure 4.31.b, there is a notable similarity between this figure and Figure 4.27, which describes the high energy yield as a function of relative concentration.

Figure 4.32 shows the result of a scaling performed on the second principal component loading with regards to the total high-energy yield, above 3 MeV. This scaling was performed to match the end points at 0.0% and 100% relative ^{239}Pu concentration. While the energy span used in the PCA algorithm is between 2650 keV to

3750 keV and not the total energy spectrum above 3 MeV, it is evident that the second component most likely corresponds to delayed γ-ray yield. Because the total high-energy yield, or any region's yield, correlates directly with relative concentration via Equation 4.16, the second principal component can be correlated to the relative ^{239}Pu concentration in the sample. Unfortunately, this correlation is subject to the same mass effects seen in spectral contribution analysis. These mass effects likely result in the observed deviations from linearity in the second principal component. Because of this, it is likely that more than one individual component is necessary to determine, with any significance, the relative concentration in a particular target.

4.5.2 PCA on a Vector of Peak Areas

In Section 4.5.1 a region spanning 1100 keV was selected for principal component analysis. While this shows great promise, such a large region is very inclusive to potentially hazardous contributions. These contributions can include random coincidence photopeaks, high continuum background and, potentially, photopeaks from activation in the sample container, detector, etc. If the issues are known, then mitigation can take the form of simply removing these sections from the spectra. Rather than remove sections of energy spectra, vectors can be formed of peak areas and fed into principal component analysis. This vector can be formed of significant photopeaks chosen to correlate to relative concentration, mass, etc. This vector would be inclusive of necessary information and exclusive of background and activation influences. Such a vector can be formed using the areas of photopeaks with any energy.

In an effort to properly discern the photopeaks necessary to determine relative concentration, the principal component scores were considered from the analysis of Section 4.5.1. PCA scores are the data mapped into the new basis set in such a way as to inherit the maximum possible variance in the data [32]. Because the second component was shown to vary primarily with relative concentration, it is the second component scores that were considered for analysis. Figure 4.33 shows the scores values of the second component as a function of energy. Positive scores indicate a positive correlation with the second component and likewise for negative scores.

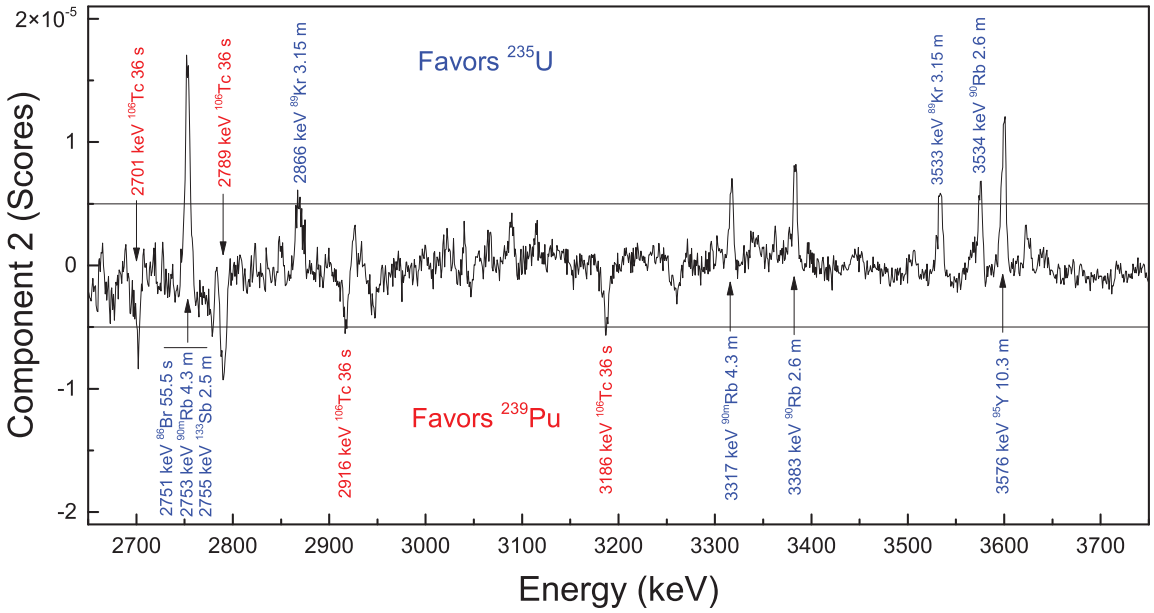

Figure 4.33: The second principal component scores as a function of energy performed using a section of the energy spectrum from 2650 keV to 3750 keV from the 90 s/90 s data set. Two lines have been drawn at $\pm 5 \cdot 10^{-6}$. Significant photopeaks are labeled in blue for those that increase as ^{235}U content increases and red for those that increase as ^{239}Pu content increases.

The magnitude of these scores indicate the strength of this correlation [32]. In the figure, two lines are drawn at $\pm 5 \cdot 10^{-6}$. This value was chosen to include sections of the spectrum, in this instance peaks, which correlate significantly with relative concentration while avoiding potential noise. It is interesting to note that this is inclusive of peaks already chosen visually for analysis in using PRA and SCA.

The vector of peak areas from Section 4.2 was used in this analysis. This vector includes all the photopeaks indicated by Figure 4.33 save for the photopeak near ~2700 keV. These vectors were normalized to total charge on the tungsten radiator. Principal component analysis was then applied to this vector in an effort to derive a more significant correlation between the component loadings and relative concentration.

Figure 4.34.a shows a scree plot of the variance described by the four principal components using vectors containing peak areas for the 90 s/90 s 132 Hz irradiation

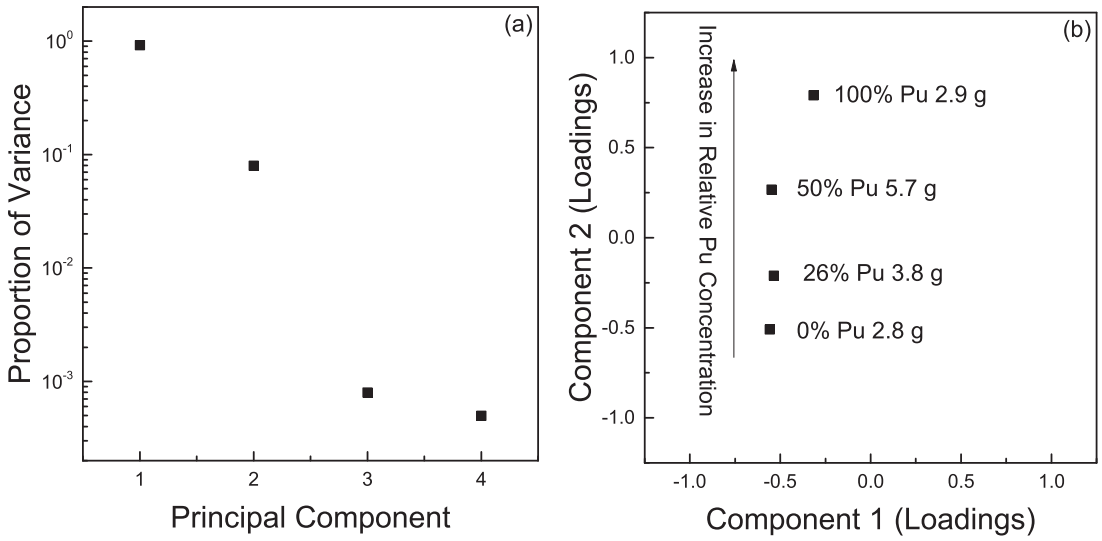

Figure 4.34: A portion of the results of principal component analysis applied to vectors containing peak areas for the 90 s/90 s 132 Hz irradiation scheme. (a) Scree plot showing the proportion of variance each principal component describes and (b) a loadings plot between the first and second components.

scheme. The proportion of variance of the first component is responsible for 91.9% of the total variance in the data. The next component is only one order of magnitude smaller than the first. In the previous section, it was this component that was most strongly associated with relative concentration. It is interesting to note that a significant portion, 99.9%, of the total variance is described by the first two components. The remaining two components are only responsible for a combined 0.1% of the total variance. It is highly probable that these two components are unimportant with regards to observables. Despite this, and because the PCA algorithm is unconstrained, correlations between all observables and components were attempted.

Figure 4.34.b shows the first two component loadings plotted against each other. Unlike in Section 4.5.1 where the first component appeared to vary relative to total fissile concentration, the first component loadings do not appear to scale with any known observable. Despite not being shown, it is likewise with the third and fourth components. This lack of correlation between these components and an observable, while unexpected, is not unheard of. PCA on its own does not presume correlations between the directions of greatest variance and any observable. The second compo-

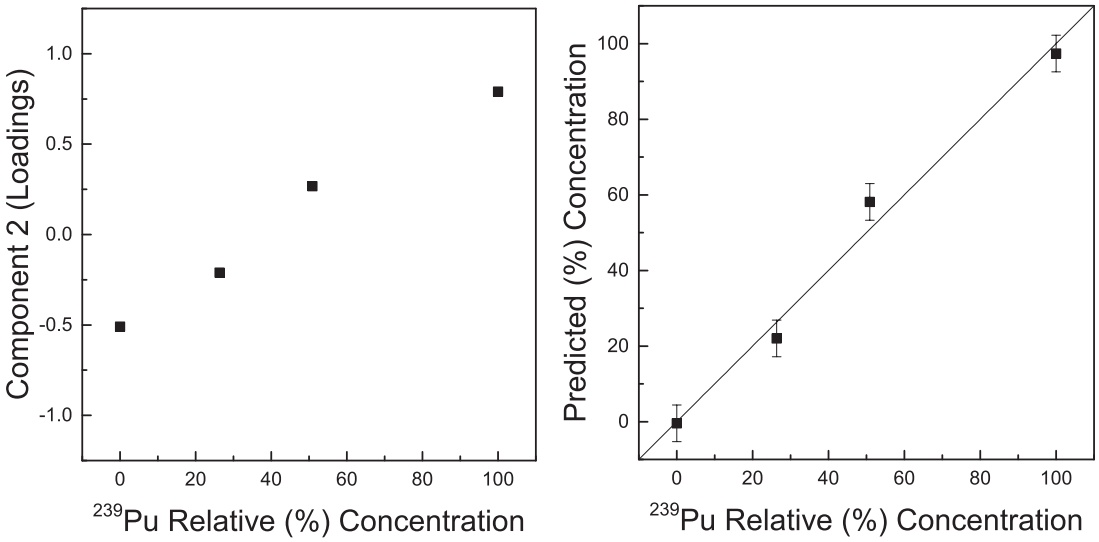

Figure 4.35: Principal component analysis on vectors containing peak areas for the 90 s/90 s 132 Hz irradiation scheme. (a) The second principal component loadings as a function of relative ^{239}Pu concentration. (b) A linear fit was applied to the second component's loadings and, subsequently, transformed into a predicted relative concentration. Error bars are representative of 1σ standard deviation and is derived from the fit parameters.

nent loadings, however, still appear to vary monotonically with relative concentration.

Figure 4.35.a shows the second principal component as a function of relative concentration. This component has a strong monotonic relationship with relative concentration. A linear fit was applied to the second component's loading and transformed into predicted relative concentration. This fit had an R^2 value of 0.979 showing a strong correlation between the second component and relative ^{239}Pu concentration. Figure 4.35.b shows the results of this transformation. The transformation results in $\sim$5% error across all four data points. This error comes from the results of the fitting algorithm and not a statistical error from the component loadings. All of the data points lie within 10% relative ^{239}Pu concentration of their expected value.

This analysis shows that in similar fashion to Section 4.3.1, the utilization of peak areas appears to reduce the influence of mass effects on the analysis. While total fissile mass cannot be determined from the first component loadings, the relationship between the second component and relative concentration is preserved. The analysis

performed in Section 4.5.1 is necessary, however, to determine the relationship between the components and observables as well as determining the photopeaks that best describe relative concentration. This method of analysis can pinpoint photopeaks desireable for PRA; however, because the data set is small, the correlation between the second component and relative concentration can not be proven with great confidence.

4.5.3 PCA Interpretation

In an effort to interpret the true correlations between the first two components, relative concentration and mass, multiple energy spectra were formed from the pure ^{239}Pu and ^{235}U delayed γ-ray spectra collected from the 90 s/90 s 132 Hz irradiation scheme. The two spectra from pure ^{239}Pu and ^{235}U were normalized to mass and total charge on target. Each spectrum was then multiplied by a theoretical mass and the two spectra were linearly combined to form a combined target with a specifically selected mass and relative concentration. Each channel of this new spectrum was then convolved with a random Gaussian distribution about the counts in that channel, with the square root of the channels counts providing the width of the Gaussian. This process was used to form a theoretical set of delayed γ-ray spectra from 30 targets. Table 4.3 shows the selected masses for each of the simulated delayed γ-ray energy spectra. This process, unfortunately, ignores the mass effects described in Section 4.4. While it would be desirable to use simulated energy spectra, time constraints prohibited this.

The 30 theoretical energy spectra were then fed though the identical PCA process used in both Sections 4.5.1 and 4.5.2. Because often only the first few components are necessary to describe the data set, only ten of the possible thirty principal components were considered in the algorithm. Figure 4.36 shows a scree plot of these ten principal components proportions of variance. Indeed, Figure 4.36 shows that only the first two should be necessary in describing a large portion of the variance in the data set. A total of 99.5% of the variance is described by these two components alone while the remaining eight components are each on the order of 10^{-4} and are probably not of

Table 4.3: ^{239}Pu and ^{235}U masses and relative ^{239}Pu concentrations of the 30 theoretical energy spectra used for interpreting the results of PCA on delayed γ-ray energy spectra.

	Constant ^{239}Pu Mass Spectra									
	1	2	3	4	5	6	7	8	9	10
^{235}U (g)	3	2.7	2.4	2.1	1.8	1.5	1.2	0.9	0.6	0.3
^{239}Pu (g)	3	3	3	3	3	3	3	3	3	3
Rel. ^{239}Pu (%)	50.0	52.6	55.6	58.8	62.5	66.7	71.4	76.9	83.3	90.9
	Constant Fissile Mass Spectra									
	11	12	13	14	15	16	17	18	19	20
^{235}U (g)	0	0.3	0.6	0.9	1.2	1.5	1.8	2.1	2.4	2.7
^{239}Pu (g)	3	2.7	2.4	2.1	1.8	1.5	1.2	0.9	0.6	0.3
Rel. ^{239}Pu (%)	100.0	90.0	80.0	70.0	60.0	50.0	40.0	30.0	20.0	10.0
	Constant ^{235}U Mass Spectra									
	21	22	23	24	25	26	27	28	29	30
^{235}U (g)	3	3	3	3	3	3	3	3	3	3
^{239}Pu (g)	0	0.3	0.6	0.9	1.2	1.5	1.8	2.1	2.4	2.7
Rel. ^{239}Pu (%)	0.0	9.1	16.7	23.1	28.6	33.3	37.5	41.2	44.4	47.4

significant interest.

Figure 4.37 shows the first two principal component loadings as a function of total fissile mass and relative concentration. Other correlations between observables such as ^{239}Pu or ^{235}U mass and other principal components were also attempted with less productive results. Figure 4.37 agrees with analysis in Sections 4.5.1 and 4.5.2 in that the first principal component shows a strong correlation with total fissile mass while the second correlates to relative concentration. However, it is clear from Figure 4.37 that these components are not completely separated. An ideal situation would result in a strong correlation between a given component and relative concentration, because the total fissile mass of a sample cannot always be controlled. Taking this into consideration, the 30 theoretical spectra were fed through a partial least squares regression algorithm to determine the minimum number of components that would be necessary to predict relative concentration with the given set of spectra.

It is clear from Figure 4.37.a that an attempt to train a least squares regression

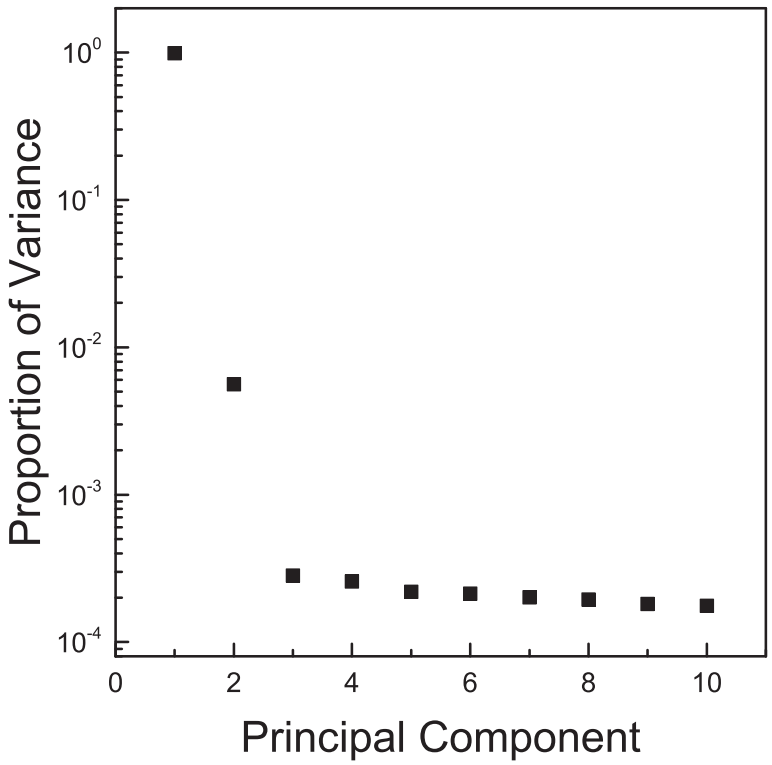

Figure 4.36: A scree plot showing the proportion of variance described by each of the first ten principal components for the data set of 30 theoretical spectra.

algorithm to relative concentration on the first principal component alone will be met with minimal success. While the scree plot in Figure 4.36 shows the relative importance of the first component it does not tie it to a specific observable. PCA simply finds a set of orthogonal axis that maximizes variance in the data. PCA does not assume any correlation about the data to any observable. In instances with multiple observables like delayed γ-ray spectra, it is necessary to comb through the results of PCA to reveal the underlying connections. In this instance, the results of PCA provide interpretable and meaningful results where the first principal component loadings can be strongly tied to total fissile mass while the second can be tied to relative concentration. It is evident from Figure 4.37.b and Figure 4.37.c that while these components do correlate greatly with fissile mass and relative concentration, there is some potential cross talk between components and observables. That is to

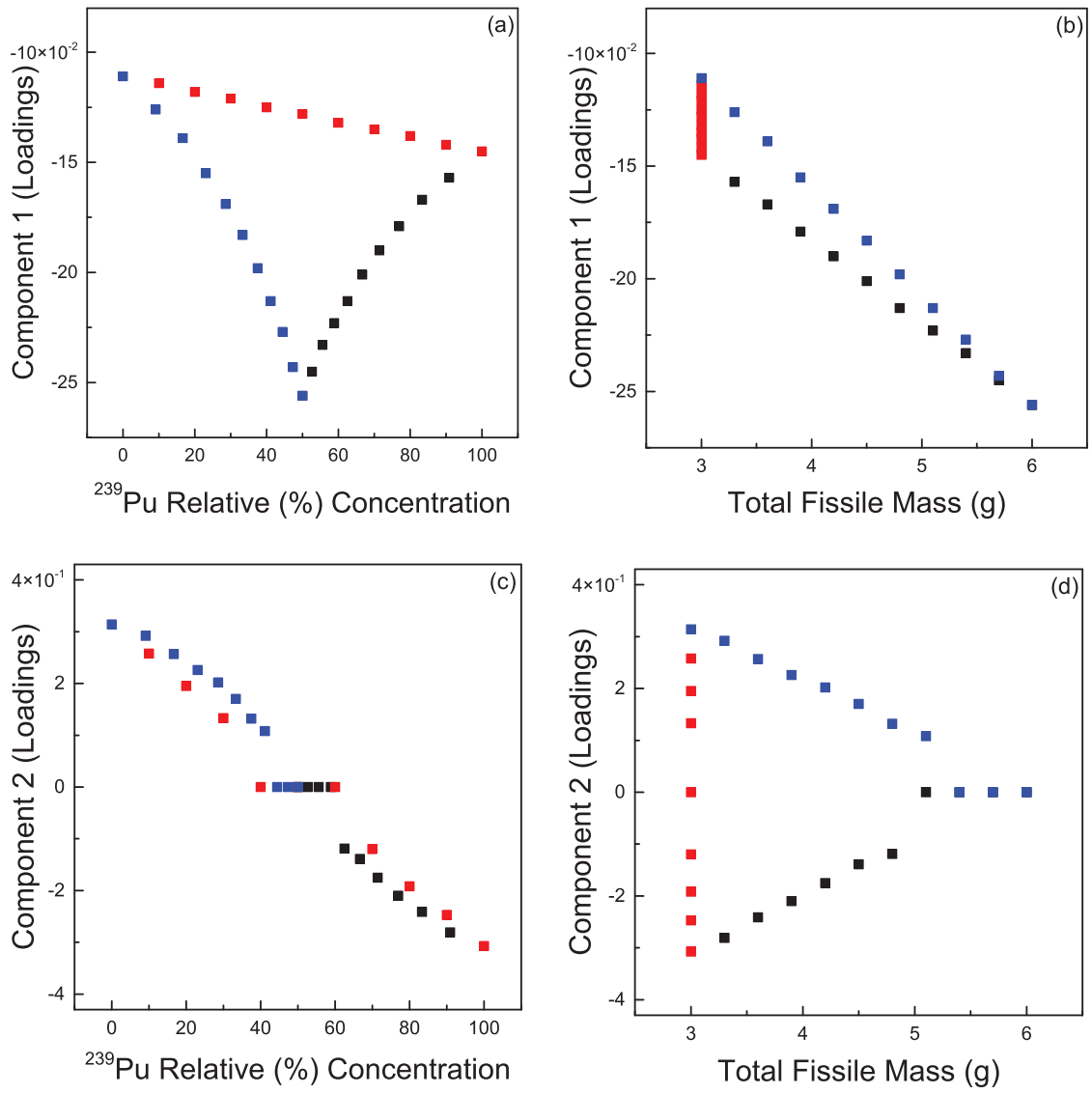

Figure 4.37: The first principal component's loadings as a function of (a) relative ^{239}Pu concentration and (b) total fissile mass along with the second principal component as a function of (c) relative ^{239}Pu concentration and (d) total fissile mass. Other possible correlations such as ^{239}Pu or ^{235}U mass and other components were also considered but with less successful results. All four plots represent data from Table 4.3 with unique identifying colors. Data representative of constant 3.0 g of ^{239}Pu is shown in black, that of a constant 3.0 g of total fissile mass is shown in red and spectra created with a constant 3.0 g of ^{235}U is shown in blue.

say that while the first component varies nearly linearly with total fissile mass there are likely influences from relative concentration and vice versa.

Further examination of the first component loadings reveal a correlation with spectral intensity. Because the intensity of a spectrum is determined essentially by $m \cdot \sigma$, and the cross section differs between ^{239}Pu and ^{235}U, this component was plotted against the product of mass and the cross section at the peak energy of the neutron spectrum. Figure 4.38 shows the result of this analysis. This correlation to intensity, and thus $m \cdot \sigma$, is due to the predilection of PCA to select the first component based on amplitude. Unfortunately, further analysis has not yielded the origin of the nonlinear relationship of the second component and relative concentration. Due to nonlinear component crosstalk as well as significant mass effects it is therefore a necessity to incorporate multiple components to formulate a more complete analysis of a given spectra.

Figure 4.39 shows the results of an attempt to train a PCA least squares regression algorithm using the data set of 30 theoretical delayed γ-ray spectra. The resulting loadings from the PCA algorithm are linearly correlated with relative concentration. Figure 4.39.a shows that to incorporate only the first component is met with failure. The R^2 value of the fit is a mere 0.48, suggesting little correlation between the first component alone and relative concentration. This is primarily because, in this case, the first component is more strongly associated with total fissile mass and not relative concentration. Figure 4.39.b shows the algorithm fit when the first two components are incorporated into the analysis. This increases the R^2 value to 0.97, showing a very strong correlation with relative concentration and a combination of the first two principal component loadings. While the first two components account for 99.6% of the total variance in the training spectra, there is still a great deal of discrepancy between the actual relative concentration and the predicted. To account for the final discrepancies between actual and predicted concentration, the third component was added to the algorithm. Figure 4.39.c shows the results of utilizing the first three components in the least squares training on the 30 theoretical spectra. While the inclusion of the third component only accounts for an additional 0.03% of the variance in the data, the result shows little deviation from the actual relative concentration.

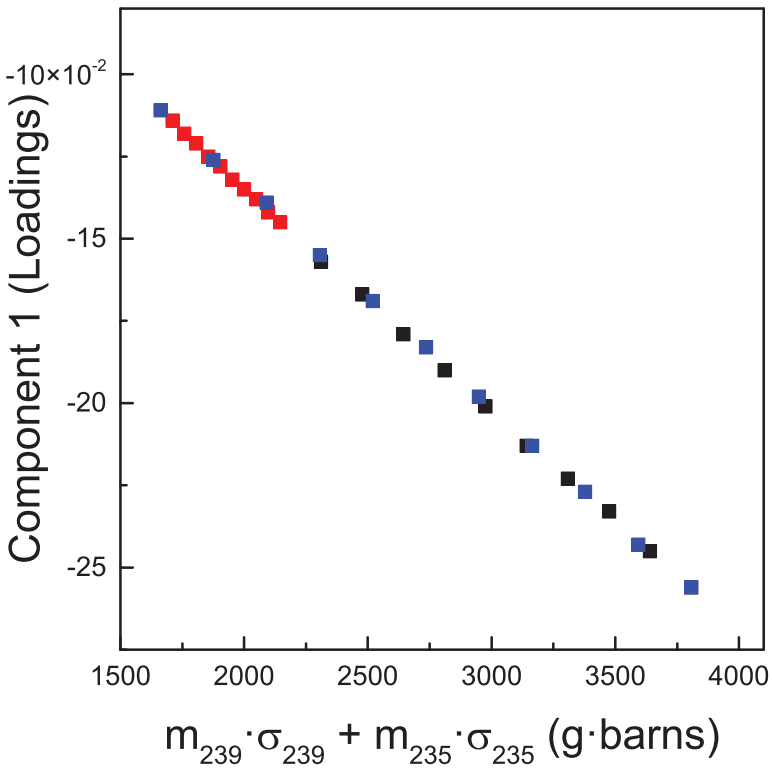

Figure 4.38: The first component loadings as a function of $m \cdot \sigma$. All four plots represent data from Table 4.3 with unique identifying colors. Data representative of constant 3.0 g of ^{239}Pu is shown in black, that of a constant 3.0 g of total fissile mass is shown in red and spectra created with a constant 3.0 g of ^{235}U is shown in blue.

This fit has a strong correlation with relative concentration with an R^2 value of 0.99. Beyond the inclusion of three components the returns are significantly diminished.

In Figure 4.39.d the trained algorithm was turned on the actual data set of four delayed γ-ray energy spectra collected from the 90 s/90 s 132 Hz irradiation scheme. While the data set used to train the algorithm is comprised of altered versions of two of the actual spectra, it is incapable of accurately predicting the concentration of these samples. The result is high in precision with an average error of $\sim$0.5% relative ^{239}Pu concentration, but is scattered an average of $\sim$10% relative concentration from actual. This is, however, not intended as a method to actually predict relative ^{239}Pu concentration in a sample and a data set of several delayed γ-ray spectra from actual known samples would be necessary to accomplish this task.

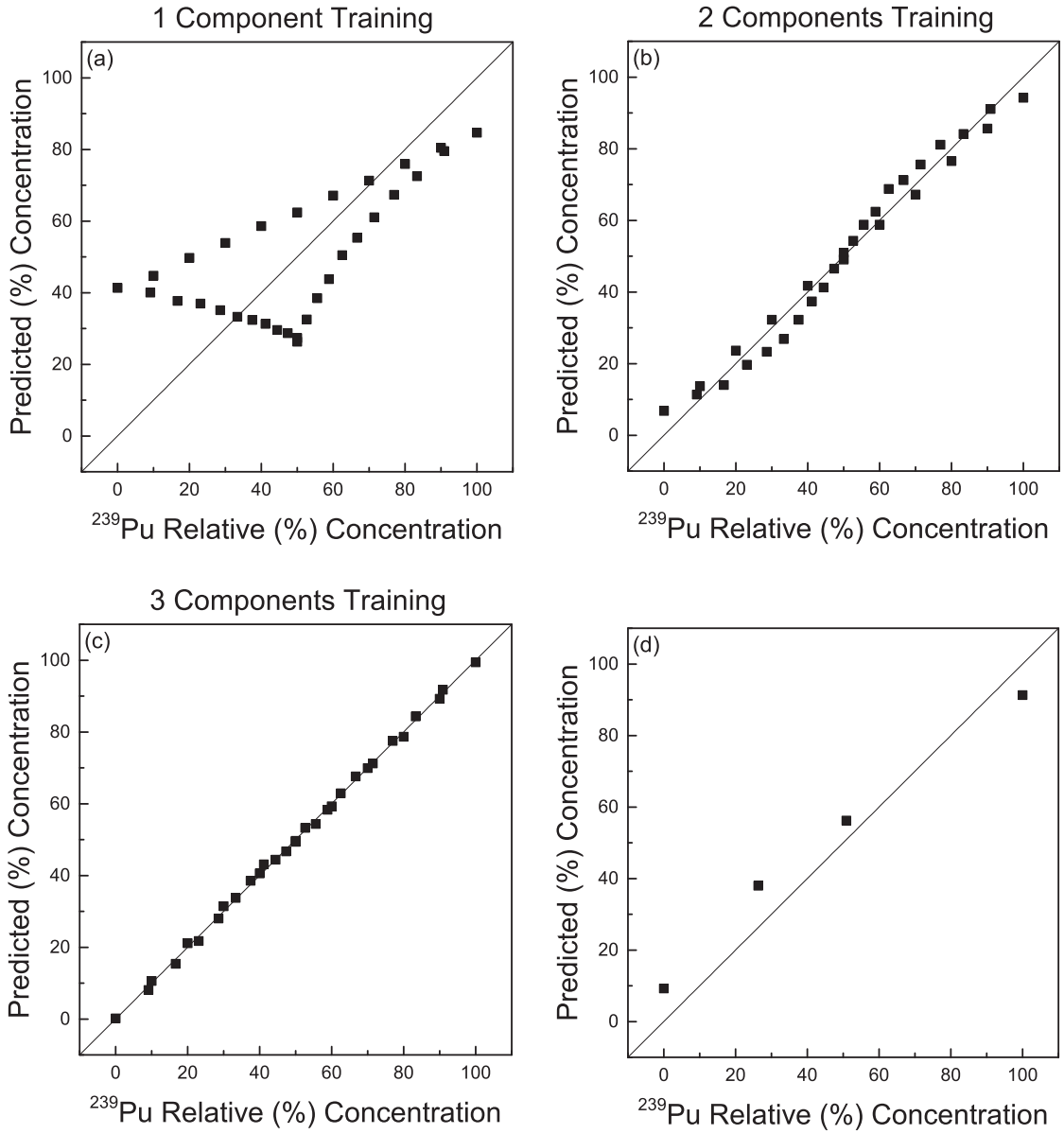

Figure 4.39: A least squares regression training applied to the principal component loadings when including only the first component (a), the first two components (b) and the first three components (c) for the theoretical data set from Table 4.3. (d) The trained principal component algorithm applied to the real delayed γ-ray spectra collected from the 90 s/90 s 132 Hz irradiation scheme. On (d) a line of equality was added and error bars are representative of 1σ standard deviation and are propagated from the fitting coefficients and not from data statistics.

Chapter 5

Conclusions

5.1 Signatures of individual isotopes

Isotopic analysis techniques that focus on the derivation of relative concentration are highly beneficial to the nuclear forensics and safeguards community. The relative concentrations of materials present in a sample of fissile material is a direct indication of its method of manufacture and enrichment. Thus, these techniques have the ability to attribute a fissile material to its origin. Multiple methods have been presented in this dissertation that serve this purpose: peak ratio analysis (PRA), spectral contribution analysis (SCA) and principal component analysis (PCA). In cases of fuel reprocessing it may also be necessary to accurately determine the mass of fissile material within a sample along with relative concentration. While not all of these methods are capable of this, both PCA and SCA can accomplish this. While it has been demonstrated that SCA can only achieve this under certain circumstances, it is a necessity to examine the capabilities of PCA further.

5.1.1 Peak Ratio Analysis

Peak ratio analysis has proven a valuable tool for the determination of relative concentration in a mixed sample of ^{239}Pu and ^{235}U. Figure 4.18 shows the results of transforming the ratio of the 3186 keV line from ^{106}Tc and the 3383 keV line from

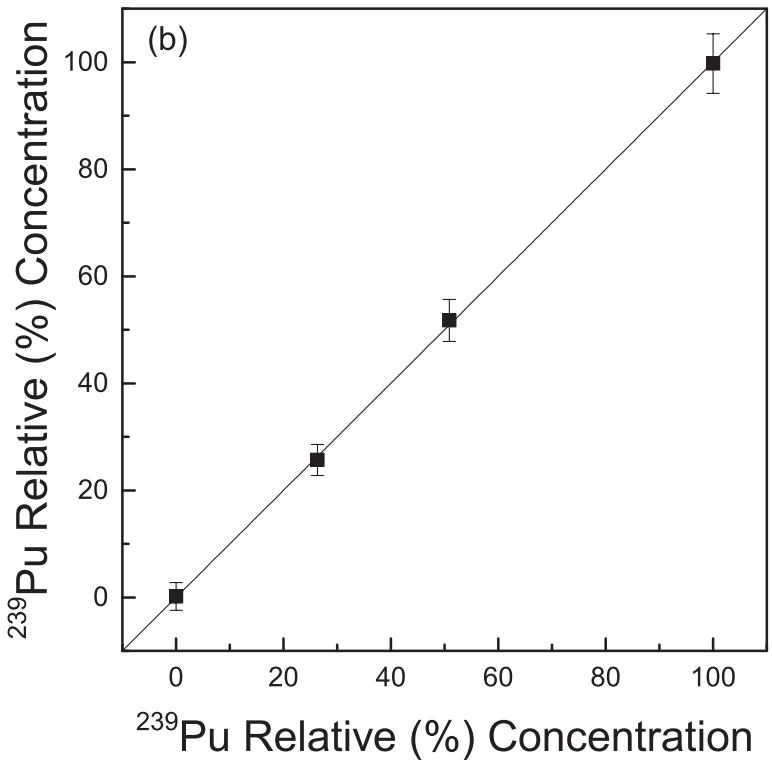

Figure 5.1: The results of transforming the ratio of the 3186 keV line from ^{106}Tc and the 3383 keV line from ^{90}Rb into relative concentration. Error bars are indicative of 1σ standard deviation.

^{90}Rb into relative concentration. This transformation results in a relatively small error, $\sim$5%, across all four targets. This resolution is achieved with a single peak ratio. With a large array of high-energy photopeaks to select from, the error can be reduced significantly by including multiple peak pairs in the analysis. The use of multiple photopeaks would also decrease the influences of other fissile materials in samples containing more than ^{239}Pu and ^{235}U.

Increases in sensitivity to a specific material can be achieved by selecting photopeaks that are exclusive to ^{239}Pu or ^{235}U. More investigation is necessary, however, if fissile materials other than ^{239}Pu and ^{235}U are present in the target. Materials such as ^{233}U, ^{241}Pu, etc., may be present in a target and influence the delayed γ-ray yield. The presence of either of these fissile materials would produce discrete γ-rays that will overlap those examined in Section 4.2 and influence the determination of the

concentration of ^{239}Pu and ^{235}U [14, 15]. The isotope ^{241}Pu is of particular interest as it is a common contaminant in plutonium samples because it cannot be separated chemically.

5.1.2 Multi-Gaussian Fitting

Multi-Gaussian fitting enables the deconvolution of multiple overlapping photopeaks. This method of fitting is further enhanced when the characteristics of the detector are known along with the energies of the photopeaks. By fixing parameters such as resolution and energy, the number of free parameters necessary to accurately deconvolve overlapping peaks is reduced. The number of parameters is further reduced if multiple photopeaks can be linked in intensity. This requires knowledge of the branching ratios as well as the detector efficiency. Figure 5.2 shows the results of a linked multi-Gaussian fitting routine overlaid on four energy spectra taken with the 90 s/90 s irradiation scheme. The results follow the energy spectra quite well. Because the 2777 keV and 2789 keV photopeaks come from the same isotope, ^{106}Tc, their intensities can be linked. This enabled the resolution of a previously undetectable photopeak from ^{91}Rb between the two at 2783 keV.

In the case shown in Figure 5.2, the peaks are close enough that detector efficiency need not be included as a factor. On a larger scale, the intensities of several photopeaks over a much wider energy range would be linked together allowing for the deconvolution of overlapping photopeaks from multiple isotopes. This method can even resolve photopeaks with identical energies as in the case with ^{90}Rb and ^{90m}Rb which share the 4366 keV photopeak along with many others [15].

5.1.3 Spectral Contribution Analysis

Spectral contribution analysis is capable of accurately determining the relative concentration within a sample of fissile material [28]. This is achieved by determining the relative spectral contribution each component provides to a spectrum of mixed material. Figure 5.3 shows the results of SCA performed using both sections of spectra and vectors of peak areas. The utilization of a vector of peak areas is quite

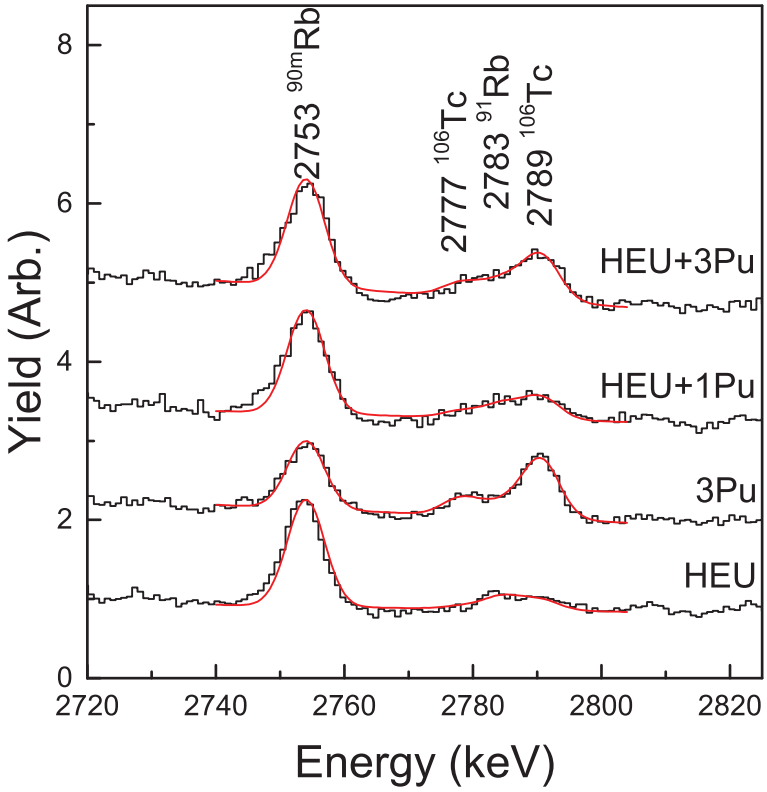

Figure 5.2: Portion of the energy spectra for the four targets listed in Table 3.3 taken utilizing the 90 s/90 s irradiation scheme. Four photopeaks are labeled with their respective energies. Three of these peaks, two from ^{106}Tc and one from ^{91}Rb overlap significantly as to be difficult to resolve. The multi-Gaussian fits are overlaid on their respective energy spectra in red. Artificial offsets have been added to enable differentiation between spectra and their structures.

accurate as compared to using sections of spectra. This is most likely due to removal of the influence of the continuum below the photopeaks which has significantly more counts than the photopeaks themselves. This background appears to have a significant impact on the results of SCA.

While previous experiments in the use of SCA have proven successful, unfortunately, because of inhomogeneity of the samples and lack of a neutron excess, the algorithm is incapable of accurate mass determination. The determination of fissile mass is desirable in instances of nuclear safeguards where such determination is necessary prior to reprocessing to determine if any material has been diverted. While

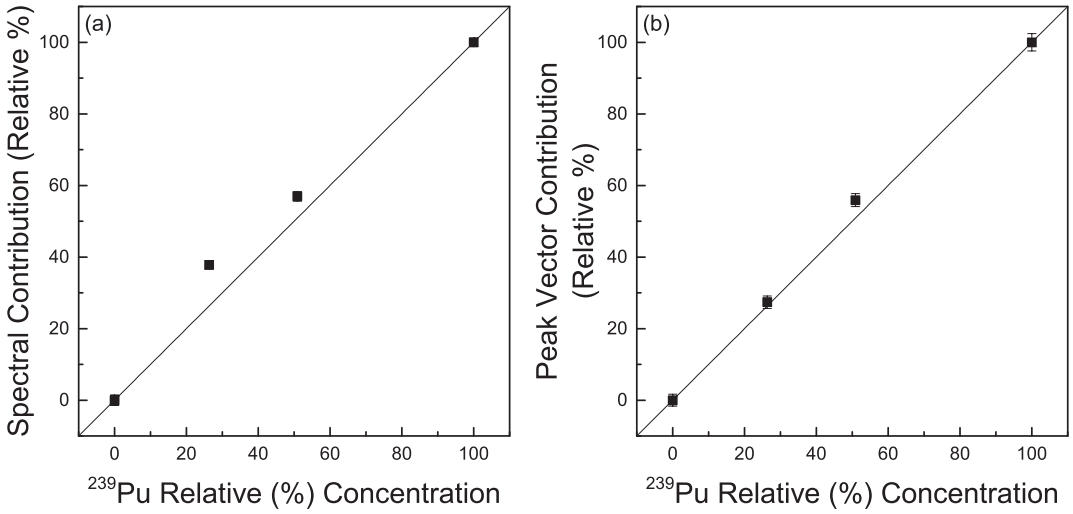

Figure 5.3: Spectral contribution analysis performed with a region of energy from 2650 keV to 3750 keV (a) and a vector of peak areas (b) from the 90 s/90 s data set. Error bars in both graphs are representative of 1σ standard deviation. The lines represent equality between relative ^{239}Pu concentration and relative ^{239}Pu spectral or peak vector contribution. For (b), the peaks areas used in PRA (Table 4.2) were aligned into a vector. The spectra and vectors of pure samples were then used as a basis set to fit those of mixed samples using least squares regression.

this aspect is lost without a plethora of neutrons for fission, SCA can still be used to determine the relative concentration.

5.1.4 Principal Component Analysis

The results of PCA are promising as a technique for determining both mass and relative concentration. Figure 5.4 shows the scores plots of the first two components from principal component analysis performed using both sections of energy spectra and a vector of photopeak areas from the 90 s/90 s data set. While using energy ranges appears to preserve both mass and relative concentration information, only the relative concentration can be determined using a vector of peak areas. Both quantities are desirable for use in applications. Because utilization of sections of spectra preserves the ability to determine information about the total fissile mass along with relative concentration without the need to fit photopeaks and deconvolve those that overlap, it is a highly desirable method.

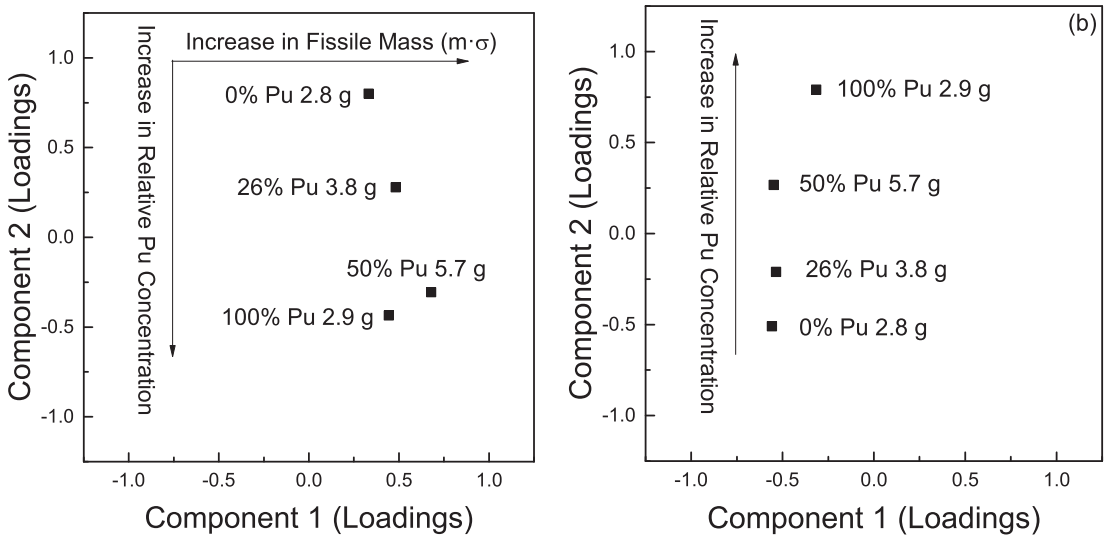

Figure 5.4: Loadings plots of the first and second principal components for principal component analysis performed using an energy from 2650 keV to 3750 keV (a) and a vector containing peak areas (b) from the 90 s/90 s data set.

Figure 5.5 shows the first component loadings as a function of the product $m \cdot \sigma$ for principal component analysis performed using an energy from 2650 keV to 3750 keV from the 90 s/90 s data set. The value σ is taken from the (n,f) cross section at the peak energy of the neutron spectrum. While the relationship between the first component and $m \cdot \sigma$ is much more linear as predicted by Section 4.5.3, the results do show some deviation. This deviation is likely due to mass effects that were not accounted for in the interpretation of principal component analysis. Regardless, the linearity of the first component is significant with respect to $m \cdot \sigma$ as compared to just mass.

One significant aspect of PCA is the ability to detect peaks significant to relative concentration. Figure 5.6 shows the scores of the second principal component when using sections of energy spectra from the 90 s/90 s data set. This component correlates strongly with relative concentration. Those scores that are significant in intensity are indicative of high degrees of variance that correlate with the second component. Because this component relates to relative concentration, these high scores identify photopeaks that correlate with relative concentration which can then be uti-

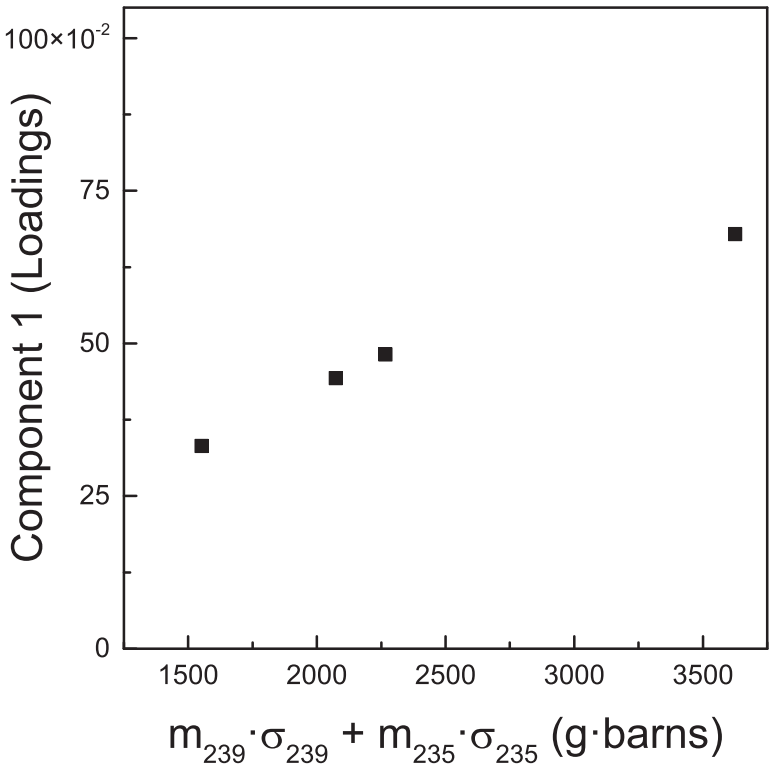

Figure 5.5: The first principal component as function of $m \cdot \sigma_{peak}$ for principal component analysis performed using an energy from 2650 keV to 3750 keV from the 90 s/90 s data set.

lized for peak ratio analysis. While the components only appear to correlate to $m \cdot \sigma$ and relative concentration, other quantities exist such as: individual isotopic mass, rate of fission, neutron multiplicity, attenuation, etc. Further analysis into the component scores may also reveal discrete photopeaks that correlate with other desirable quantities.

Unfortunately, while PCA is very promising in determining fissile mass, or at least $m \cdot \sigma$, in conjunction with relative concentration, it lacks essential data. Because only four targets were examined, it was necessary to utilize a set of theoretical spectra. While this analysis is promising, the theoretical spectra do not incorporate mass effects making it is necessary to repeat this process with a multitude of spectra acquired from a physical experiment.

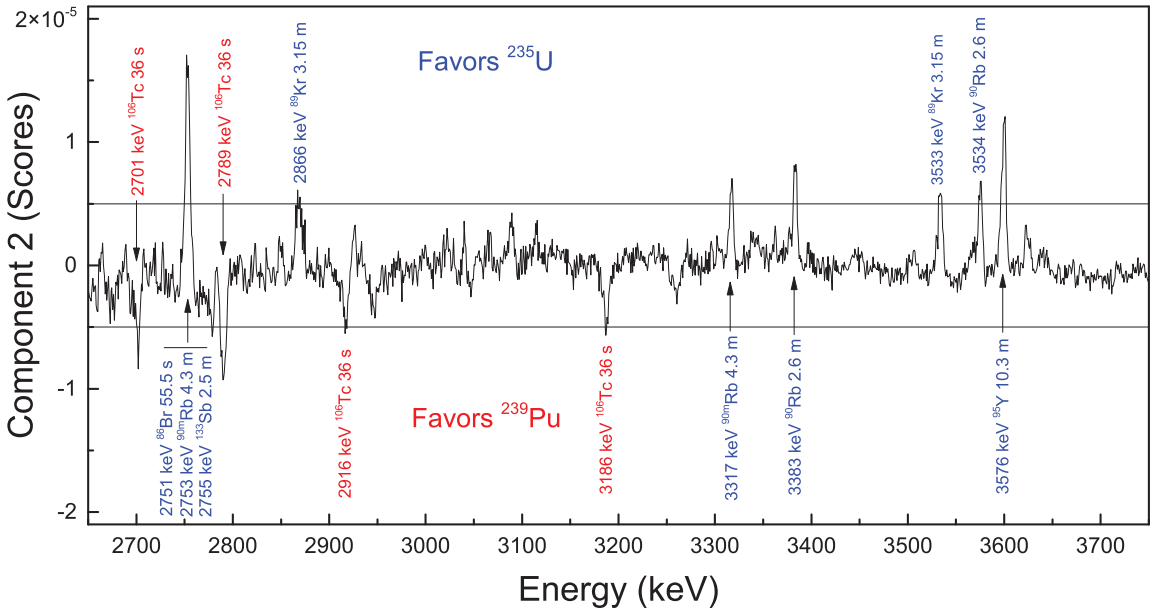

Figure 5.6: The second principal component scores as a function of energy performed using a section of the energy spectrum from 2650 keV to 3750 keV from the 90 s/90 s data set. Two lines have been drawn at $\pm 5 \cdot 10^{-6}$.

5.2 Future Work

To improve upon the techniques in this dissertation, it would be desirable to model dozens if not hundreds of irradiation, shuttle and count time structures. This would eliminate the need to utilize costly accelerator time for optimization. This modeling could also serve to identify issues faced by analysis techniques such as SCA by determining the neutron consumption within the setup and resolve possible ways to produce a neutron excess. This excess would minimize mass effects in the targets enabling SCA to accurately determine the mass within a given target. By shifting the time and costs away from the experimental to modeling, more experiment time would be available to utilize for either increasing statistics within measurements or examination of a larger sample population. The increased sample population would benefit all aspects of analysis where the population is just too small to make accurate determinations.

Appendix A

^{241}Pu Determination

The two isotopes, ^{239}Pu and ^{241}Pu, have the same chemical attributes and thus cannot be chemically separated. This makes ^{241}Pu a potential contaminant resulting from the manufacture of ^{239}Pu based nuclear weapons. The ability to determine the quantity of ^{241}Pu is, thus, highly desirable. The two isotopes differ by only 2 Da in mass which makes much of their fission fragment distributions overlap in yield. While their cumulative mass yields are similar in shape the yields of individual isotopes within both the high-mass and low-mass distributions differs greatly. Figure A.1 shows the difference in cumulative high-energy γ-ray yield between ^{239}Pu and ^{241}Pu. Many fission fragments in the high-mass distribution favor that of ^{241}Pu while those in the low-mass distribution favor ^{239}Pu. This analysis points to the possibility of many photopeaks in the high-energy region (above 3 MeV) that would be unique to ^{241}Pu or ^{239}Pu enabling the detection and differentiation of the two.

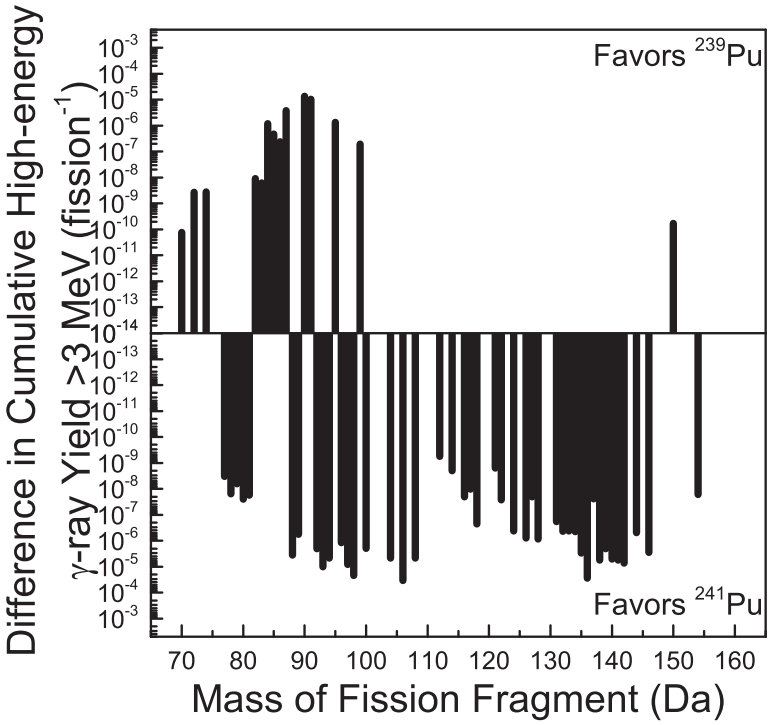

Figure A.1: The difference in yield of high-energy γ-rays between ^{239}Pu and ^{241}Pu for fast-pool neutron induced fission. The larger yield differences favor ^{241}Pu while some γ-rays favor ^{239}Pu [14, 15].

Bibliography

[1] W. Bertozzi, S. E. Korbly, R. J. Ledoux, and W. Park. Nuclear resonance fluorescence and effective Z determination applied to detection and imaging of special nuclear material, explosives, toxic substances and contraband. *Nucl. Instrum. Methods Phys. Res. B*, 261:331, 2007.

[2] W. Bertozzi, J. A. Caggiano, W. K. Hensley, M. S. Johnson, S. E. Korbly, R. J. Ledoux, D. P. McNabb, and E. B. Norman. Nuclear resonance fluorescence excitation near 2 Mev in ^{238}U and ^{239}Pu. *Phys. Rev. C*, 78:041601, 2008.

[3] D. R. Slaughter, M. R. Accatino, A. Bernstein, P. Biltoft, J. A. Church, M. A. Descalle, J. M. Hall, D. R. Manatt, G. J. Mauger, T. L. Moore, E. B. Norman, D. C. Peterson, J. A. Pruet, and S. G. Prussin. The nuclear car wash: A system to detect nuclear weapons in commercial cargo shipments. *Nucl. Instrum. Methods Phys. Res. A*, 579:349, 2007.

[4] F. Carrel, M. Agelou, M. Gmar, Lainé, J. Loridon, J. Ma, C. Passard, and B. Poumaréde. Identification and differentiation of actinides inside nuclear waste packages by measurement of delayed gammas. *IEEE Trans. Nucl. Sci.*, 57:2862, 2010.

[5] B. J. Micklich and D. L. Smith. Nuclear materials detection using high-energy γ-rays. *Nucl. Instrum. Methods Phys. Res. B*, 241:782, 2005.

[6] L.W. Campbell, L.E. Smith, and A.C. Misner. High-energy delayed gamma spectroscopy for spent nuclear fuel assay. *Nuclear Science, IEEE Transactions on*, 58(1):231–240, 2011.

[7] E. B. Norman, S. G. Prussin, R. M. Larimer, H. Shugart, E. Browne, A. R. Smith, R. J. McDonald, H. Nitsche, P. Gupta, M. I. Frank, and T. B. Gosnell. Signatures of fissile materials: high-energy γ rays following fission. *Nucl. Instrum. Methods Phys. Res. A*, 521:608, 2004.

[8] V. Mozin, S.J. Tobin, L.W. Cambell, J.R. Cheatham, C.R. Freeman, C.J. Gesh, A. Hunt, B.A. Ludewigt, E.T.E. Reedy, H.A. Selpel, et al. Determining plutonium mass in spent fuel with non-destructive assay techniques-NGSI research overview and update on NDA techniques, part II. In *Proceedings Symposium on International Safeguards: Preparing for Future Verification Challenges*, 2010.

[9] A. Iyengar, E.B. Norman, C. Howard, C. Angell, A. Kaplan, J.J. Ressler, P. Chodash, E. Swanberg, A. Czeszumska, B. Wang, R. Yee, and H.A. Shugart. Distinguishing fissions of ^{232}Th, ^{237}Np and ^{238}U with beta-delayed gamma-rays. *Nucl. Instrum. Methods Phys. Res. B: Beam Interactions with Materials and Atoms*, 304(0):11 – 15, 2013.

[10] E. T. E. Reedy, S. J. Thompson, and A. W. Hunt. The detection of delayed γ-rays between intense bremsstrahlung pulses for discriminating fissionable from non-fissionable materials. *Nucl. Instrum. Methods Phys. Res. A*, 606:811, 2009.

[11] Niels Bohr and John Archibald Wheeler. The mechanism of nuclear fission. *Phys. Rev.*, 56(5):426, 1939.

[12] Tsahi Gozani. Active nondestructive assay of nuclear materials. Technical Report NUREG/CR-0602, United States Regulatory Commission, 1981.

[13] T. R. England and B. F. Rider. ENDF-349 evaluation and compilation of fission product yields 1993. Technical Report LA-UR-94-3106, Los Alamos Nationatial Laboratory, Los Alamos New Mexico, USA, 1994.

[14] M.B. Chadwick, P. Obložinský, M. Herman, et al. ENDF/B-VII.0: Next generation evaluated nuclear data library for nuclear science and technology. *Nuclear Data Sheets*, 107(12):2931, 2006.

[15] M. R. Bhat. Evaluated nuclear structure data file (ENSDF). *Nucl. Data for Sci. and Tech.*, page 817, 1992. Data extracted using the NNDC On-Line Data Service from the ENSDF database, file revised as of 7/22/2009.

[16] J. R. Phillips. Passive nondestructive assay of nuclear materials. In D. Reilly, editor, *Irradiated Fuel Measurements*. 1991. NUREG/CR-5550.

[17] J. L. Jones, B. W. Blackburn, D. R. Norman, S. M. Watson, K. J. Haskell, J. T. Johnson, A. W. Hunt, F. Harmon, and C. Moss. State of the prototype pulsed photonuclear assessment (PPA) inspection system. *Nucl. Instrum. Methods Phys. Res. A*, 579:353, 2007.

[18] J. Hu, S.J. Tobin, H.O. Menlove, and S. Croft. Determining plutonium mass in spent fuel using ^{252}Cf interrogation with prompt neutron detection. 2010.

[19] M. C. Brady and T. R. England. Delayed neutron data and group parameters for 43 fissioning systems. *Nucl. Sci. Eng.*, 103:129, 1989.

[20] O. Hahn and F. Strassmann. *Naturwissenschaften*, 27:11, 1939.

[21] L. Meitner and O. R. Frisch. *Nature*, 143:239, 1939.

[22] S. S. M. Wong. *Introductory Nuclear Physics*. John Wiley and Sons, Inc., New York, second edition, 1998.

[23] K.S. Krane. *Introductory Nuclear Physics*. Wiley, 1987.

[24] Glenn F. Knoll. *Radiation Detection and Measurement*. John Wiley and Sons, Inc., New York, third edition, 2000.

[25] R. E. Mars, E. B. Norman, J. T. Burke, R. A. Macri, H. A. Shugart, E. Browne, and A. R. Smith. Fission-product gamma-ray line pairs sensitive to fissile material and neutron energy. *Nucl. Instrum. Methods Phys. Res. A*, 592:463, 2008.

[26] D. H. Beddingfield and F. E. Cecil. Identification of fissile materials from fission product gamma-ray spectra. *Nucl. Instrum. Methods Phys. Res. A*, 417:405, 1998.

[27] C. L. Hollas, D. A. Close, and C. E. Moss. Analysis of fissionable material using delayed gamma rays from photofission. *Nucl. Instrum. Methods Phys. Res. B*, 24-25:503, 1987.

[28] E.T.E. Reedy. Discrete Gamma-Rays from Photofission for Nuclear Forensics Applictions. Master's thesis, Idaho State University, 921 S 8th Ave, Pocatello, ID 83201, 2011.

[29] M.B. Leboeuf. *Optimizing Neutron Activation Analysis*. May 1965.

[30] K. Pearson. Liii. on lines and planes of closest fit to systems of points in space. *Philosophical Magazine Series 6*, 2(11):559–572, 1901.

[31] H. Hotelling. Analysis of a complex of statistical variables into principal components. *Journal of Educational Psychology*, 24:417–441, 1933.

[32] I.T. Jolliffe. *Principal Component Analysis*. Springer, New York, second edition, 2002.

[33] V. Mozin. *Delayed Gamma-Ray Assay for Nuclear Safeguards*. PhD thesis, University of California, Berkeley, 2011.

[34] U. S. Department of Energy. Uncertainty analysis of the SWEPP plutonium sources (NADS and ZPPRS). Technical Report EDF-3153, Idaho National Engineering and Environmental Laboratory, Idaho Falls, Idaho, 2002.

[35] Advanced Measurement Technology, Inc. *Model 672 Spectroscopy Amplifier Operating and Service Manual*, manual revision h edition.

[36] Canberra, 800 Research Parkway, Meriden, CT 06450 USA. *Model 8701 ADC Users Manual*, 1999.

[37] D. H. Wilkinson. A stable ninety-nine channel pulse amplitude analyser for slow counting. *Mathematical Proceedings of the Cambridge Philosophical Society*, 46:508–518, 7 1950.

[38] Advanced Measurement Technology, Inc. *Model 973U Ultra-High-Rate Spectroscopy Amplifier Operating and Service Manual*, manual revision e edition.

[39] Canberra, 800 Research Parkway, Meriden, CT 06450 USA. *Model 8715 ADC Users Manual*, 1999.

[40] M. Geenty. personal communication, March 2015. Case# 4809 - 8715 ADC Analog Conversion Inquiry.

[41] J.H. Kalivas. Two data sets of near infrared spectra. *Chemometrics and Intelligent Laboratory Systems*, 37(2):255 – 259, 1997.

[42] Y.H. Choi, H.K. Kim, A. Hazekamp, C. Erkelens, A.W.M. Lefeber, and R. Verpoorte. Metabolomic differentiation of cannabis sativa cultivars using 1h NMR spectroscopy and principal component analysis. *Journal of Natural Products*, 67(6):953–957, 2004. PMID: 15217272.